The use of UV Resonance Raman Spectroscopy in the analysis of ionizing radiation-induced damage in DNA

by

Conor Shaw

BSc, University of Victoria, 2005

A Dissertation Submitted in Partial Fulfillment of the
Requirements for the Degree of

Masters of Science

in the Department of Physics and Astronomy

University of Victoria

The use of UV Resonance Raman Spectroscopy in the analysis of ionizing radiation-induced damage in DNA

by

Conor Shaw
BSc, University of Victoria, 2005

Supervisory Committee

Dr. A. Jirasek, Supervisor (Department of Physics and Astronomy)

Dr. G. Steeves, Member (Department of Physics and Astronomy)

Dr. W. Ansbacher, Member (British Columbia Cancer Agency - Vancouver Island Centre)

Dr. A. Brolo, Outside Member (Department of Chemistry)

Supervisory Committee

Dr. A. Jirasek, Supervisor (Department of Physics and Astronomy)

Dr. G. Steeves, Member (Department of Physics and Astronomy)

Dr. W. Ansbacher, Member (British Columbia Cancer Agency - Vancouver Island Centre)

Dr. A. Brolo, Outside Member (Department of Chemistry)

Abstract

Raman spectroscopy is a form of vibrational spectroscopy that is capable of probing biological samples at a molecular level. In this work it was used in the analysis of ionizing radiation-induced damage in DNA. Spectra of both simple, short-stranded DNA oligomers (SS-DNA) and the more complicated calf-thymus DNA (CT-DNA) were acquired before and after irradiation to a variety of doses from 0 to $\sim$ 2000 Gy. In a technique known as ultraviolet resonance Raman spectroscopy (UVRRS), three UV wavelengths of 248, 257 and 264 nm were utilized in order to selectively enhance contributions from different molecular groups within the samples. Assignment of the spectral peaks was aided by the literature, as well as through analysis of UVRR spectra of short strands of the individual DNA bases obtained at each of the three incident UV wavelengths. Difference spectra between the irradiated and unirradiated samples were calculated and the samples exposed to $\sim$ 2000 Gy showed significant radiation-induced features. Intensity increases of spectral peaks, observed

primarily in the CT-DNA, indicated unstacking of the DNA bases and disruption of Watson-Crick hydrogen bonds, while intensity decreases of spectral peaks, observed only in the SS-DNA, indicated both base damage and the loss of structural integrity of the DNA molecule. The high molecular specificity of UVRRS allowed for precise identification of the specific bonds affected by the radiation, and the use of the varying incident wavelengths allowed for the observation of damage to moieties that would otherwise have been excluded. The use of UVRRS shows promise in the study of radiation-induced damage to DNA and would be well suited for extension to the study of more complicated biological systems.

Table of Contents

List of Tables

List of Figures

Acknowledgements

I can't believe I'm finally writing the acknowledgments! I finally made it! I would have never gotten to this point if not for the advice and guidance of my supervisor Andrew Jirasek. Thank you for your patience! I also want to thank Wayne Beckham and everyone at the Cancer Centre and everybody in the Medical Physics program for all of their support. Special thanks to Holly Johnston for making classes more interesting, Quinn Matthews for his two-point MEM code, Dave Rudko for coming to my defense and of course Karl Bush for leading the way through graduate school and for proving that the impossible is possible by getting an iPhone before everyone else in Canada.

Despite Karl's great example, there were many times when I thought that I was going to screw everything up and I am in debt to my mum, step-dad, dad and Kathy for always reminding me that I could get through this! Also, thanks to my brother for his "Chapter writing Reward System," the rules of which I still don't understand. Thank you also to Nichole Nutz from IDT DNA for all of her friendly advice about how to deal with DNA oligomers (you can get anything online these days!). Also, thanks to Alex Brolo for letting me use his Raman equipment and all of the Brolonians for their help!

Finally, I want to thank everyone in the Physics & Astronomy Department for all of their support, particularly Joy for always knowing what to do, and Michel Lefebvre for showing up to my defense! Also, one more thank you to Andrew Jirasek. I look forward to working with you in the future!

Chapter 1

Introduction

1.1 Radiation Therapy

The medical applications of radiation have been developing steadily since the late 1800's. In 1895, after Wilhelm Conrad Roentgen discovered the electromagnetic radiation now known as x-rays, he quickly noticed the ability of this unique radiation to image the internal structure of the human body after observing the shadow of his wife's bones on a film exposed by x-rays that had passed through her hand [1]. Shortly after, Pierre and Marie Curie's discovery and subsequent experiments with the radioactive sources polonium and radium further strengthened the idea that radiation could be useful in the destruction of cancerous tumours [2]. The fields of medical imaging and radiation therapy have come a long way since then, and have proven invaluable in the diagnosis and treatment of cancer.

While early radiation therapy often resulted in high radiation doses to healthy tissue, the goal of modern conformal radiation therapy is to maximize radiation dose to tumourous tissue while minimizing dose to healthy tissue. With the improvements in medical imaging instruments, such as computed-tomography (CT) and magnetic resonance imaging (MRI) units, the ability to locate a tumour and surrounding organs at risk is greatly enhanced. Based on these images, a treatment plan can be produced that provides a high dose to the tumour, but spares surrounding organs and healthy

tissue.

Although cancer is the leading cause of premature death in Canada [3], the mortality rates of most types of cancer have decreased since 1994 [3], thanks in large part to improvements in cancer treatment, including radiotherapy. Many forms of cancer are treated by, or in conjunction with radiation therapy, and in many cases, the treatment is curative, resulting in the eradication of the tumour. In other cases, the treatment can significantly increase the years of survival for the patient, or it can be used in a palliative sense to alleviate painful symptoms of the cancer. In all of these cases, radiation therapy can be very effective, and some of the typical types of treatment are described in standard texts [4, 5]. Through advancements in modern radiotherapy and other forms of cancer treatment such as chemotherapy and surgery, the mortality rate of cancer will continue to decrease.

Unfortunately, alongside the benefits, the inevitable exposure of healthy tissue to radiation during treatment continues to be of concern in radiation therapy. As a result, it is important to understand the nature of the effects of radiation on human tissue, and the damage that can be caused to its constituent cells. It is known that damage to the deoxyribonucleic acid (DNA) contained in the cell nucleus has a significant effect on the lifetime of a cell, and, as such, the effects of radiation on DNA are of particular interest. While there are repair mechanisms for DNA damage, they are not always successful, and this can lead to the inability of a cell to replicate, and ultimately, its death.

1.2 DNA

Deoxyribonucleic acid (DNA) is often thought of as the essential building block of life. It is contained within the cells of every living organism and is passed on during cell reproduction. The DNA molecule contains the genetic blueprints that control the chemical reactions in the cells of an organism, such as protein production [6]. These

chemical reactions in turn define the characteristics of an organism, and thus DNA is what makes a living creature unique. In order to be able to better understand DNA, and how it works, it is first necessary to understand its composition, and how it is structured, as discussed in the following section.

1.2.1 Structure of DNA

DNA is essentially a long molecular chain containing hydrogen, carbon, nitrogen and phosphorous atoms. The atoms are organized into structures referred to as nucleotides, which consist of a deoxyribose sugar bonded to both a phosphate group and a nitrogen base, as in figure 1.1. There are four different nitrogen bases that make up DNA, and they can be classified into two different groups. Each nitrogen base is essentially a complex ring structure containing carbon and nitrogen atoms. The *pyrimidine* bases each consist of a single aromatic ring of six atoms, known as thymine and cytosine (figure 1.1). Adenine and guanine are the other two DNA bases, consisting of a fused double ring made up of nine atoms. These are known as the *purine* bases (figure 1.1).

The DNA molecule is composed of two chains of nucleotides that join together to form the familiar double helix structure shown in figure 1.2. The two nucleotide chains are held together through hydrogen bonds between the bases of the nucleotides on each side of the helix (see figure 1.1). These are called Watson-Crick hydrogen bonds, after the discoverers of the double helix structure of DNA [7]. When the bases connect through these hydrogen bonds to form a base pair, a purine base must always pair with a pyrimidine base. In fact, each base only pairs with one of the other three. Adenine only pairs with thymine, and guanine only pairs with cytosine. To complete the double helix structure, the bonds between the sugar and phosphate groups of consecutive nucleotides on each nucleotide chain form the backbone of the DNA molecule (see figure 1.1). The double helix can be thought of as a twisted ladder, with the sugar-phosphate backbone making the sides of the ladder, and the

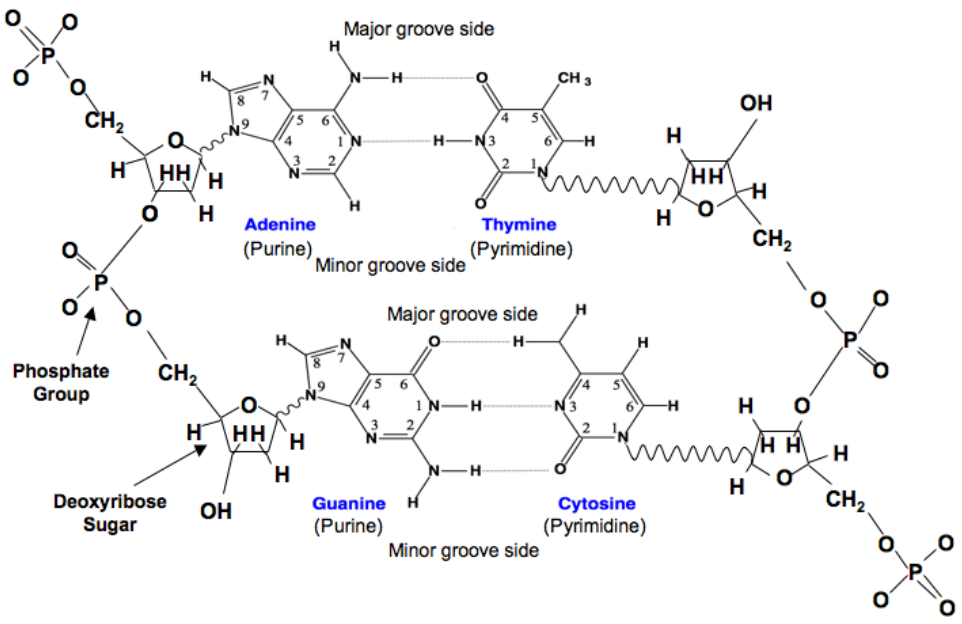

Figure 1.1: Schematic diagram of the purine and pyrimidine bases, and the sugar/phosphate backbone. The dotted lines indicate hydrogen bonds. The major and minor groove sides of the base pairs are also identified.

connecting base pairs acting as its rungs.

While the hydrogen bonds between the bases hold the sides of the helix together, the molecule is allowed further stability through a process known as *base stacking* [8, 9]. This stability comes from the energetically favourable situation of the planes of the connecting base pairs being arranged parallel to each other, one on top of the other, like a stack of coins. In this orientation, the electron clouds of the double bonds (also known as pi-bonds) in a given base ring overlap with those of the corresponding bonds in the adjacent bases stacked above and below. The overlapping electron clouds join in a non-covalent bond, stabilizing the DNA molecule in this stacked structure. A more detailed discussion of all of the forces that play a part in the formation and stability of the double-helix structure of DNA is given in a variety of studies on the molecular stability of DNA [10–14].

Although DNA is always found in the double helix structure, the *conformation* of the helix can vary depending on the environment in which the DNA is found.

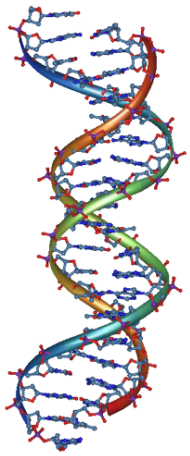

Figure 1.2: Diagram showing the double helix structure of a sample DNA sequence. Created using iMol Molecular Visualizer (P. Rotkiewicz, 2007).

.

Changes in conformation result in changes in how tightly wound the helix is, and in the spacing and orientation of the base pairs. In nature, the three conformations that are observable are described as *A, B,* and *Z-DNA*. In aqueous solutions, and in cells, B-DNA is most commonly observed [15–17]. A-DNA and Z-DNA can also be found in cells under special circumstances [18, 19], but in non-physiological situations, A-DNA is prominent in dehydrated DNA samples, and Z-DNA is present in solutions with high concentrations of salts like $MgCl_2$ and NaCl [15, 20].

The main differences between the three conformations can be classified in terms of the way that the bases are stacked, the tilt of the base pairs, and the position of the helical axis. Each conformation is also characterized by the width and depth of it's major and minor grooves, which correspond to the spacing between the two phosphate backbone strands measured on opposite sides of the base pairs, as shown in figure 1.1. A detailed description of the differences between the A, B and Z conformations is given in a review article elsewhere [15], but, briefly, as seen in figure 1.3, A-DNA forms a wide and stubby double helix, B-DNA is more extended and symmetric about the helical axis, while Z-DNA is even further extended about the axis, and, instead of a smoothly coiling backbone, the backbone of Z-DNA adopts a zig-zag pattern, hence

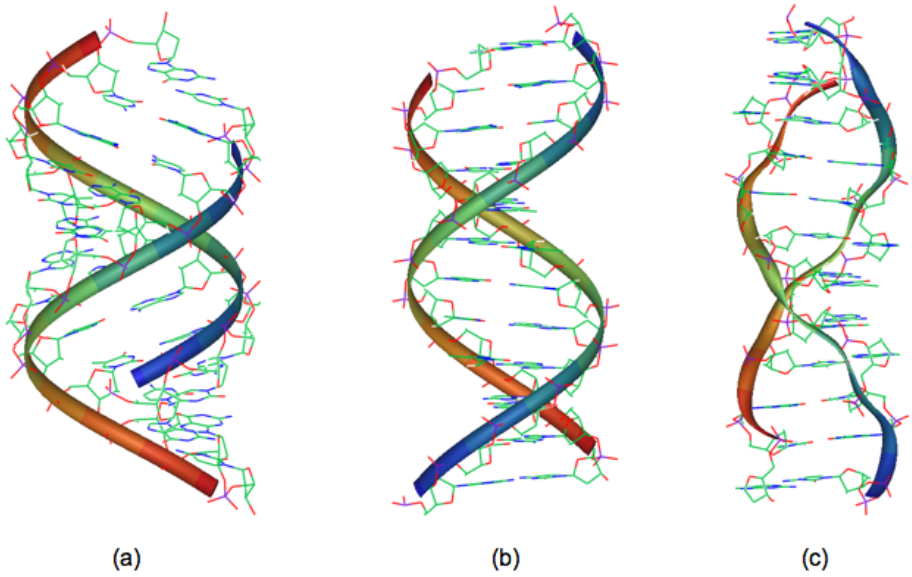

Figure 1.3: The three conformations of DNA found in nature. (a) A-DNA (b) B-DNA (c) Z-DNA. Created using iMol Molecular Visualizer (P. Rotkiewicz, 2007).

.

it's Z designation. Also, unlike the right-handed helices of A and B-DNA, Z-DNA is a left-handed helix, meaning that it winds in a counter-clockwise sense around the helical axis.

In general, base sequence, the degree of base stacking, and the helical conformation all help to define the structure of DNA. An understanding of the DNA structure of a sample under study is critical, as when faced with any kind of stress, such as ionizing radiation-induced damage, all of the structural properties of DNA will be affected and potentially modified.

1.2.2 Ionizing Radiation-Induced DNA Damage

Cell damage due to ionizing radiation results in some type of biologic effect, such as cell death, mutation, or carcinogenesis, and there is strong evidence to suggest that damage to DNA is the catalyst for this change [21]. Radiation damage to DNA can be induced through either the *direct* or *indirect* action of radiation. Direct effects occur either when the incident radiation excites or ionizes the atoms of the medium

containing the DNA, liberating electrons that then go on to disrupt the molecular bonds, or when the radiation itself causes ionization in the DNA. This chain of events is most often initiated by directly ionizing radiation such as neutrons or alpha particles [21], while the indirect action of radiation is the primary mechanism by which indirectly ionizing radiation causes damage. In this case, the incident radiation interacts with atoms or molecules within the medium containing the DNA, creating *free radicals* that can disrupt and damage DNA. Whether dealing with cellular DNA, or free DNA in a solution, the DNA is typically surrounded by water molecules, which react readily with radiation to form free radicals. This process can occur through a variety of different reactions, such as the series given below:

$$H_2O \rightarrow H_2O^+ \cdot + e^- \tag{1.1}$$

$$H_2O^+ \cdot + H_2O \rightarrow H_3O^+ + OH\cdot \tag{1.2}$$

where e^- is a free electron, $H_2O^+\cdot$ is an ion radical, and $OH\cdot$ is the hydroxyl radical. The ion and hydroxyl radicals are both free radicals, but the ion radical has a short lifetime and rapidly decays into the hydroxyl radical [21].

Whether through the direct or indirect action of radiation, the ionizing radiation-induced damage to DNA is often classified as either a *single-strand break* (SSB), or a *double-strand break* (DSB). Single-strand breaks occur frequently, even at low radiation doses, and involve a break on one side of the helix which affects the sugar-phosphate backbone and perhaps a nearby base (figure 1.4(a)). As this damage is localized to one side of the double helix, it is easily repaired by the inherent repair mechanism of cellular DNA, with the undamaged side used as a template [21]. Even multiple SSBs on one DNA molecule can be repaired without incident, but if two breaks on opposite sides of the helix are within a few base pairs of each other,

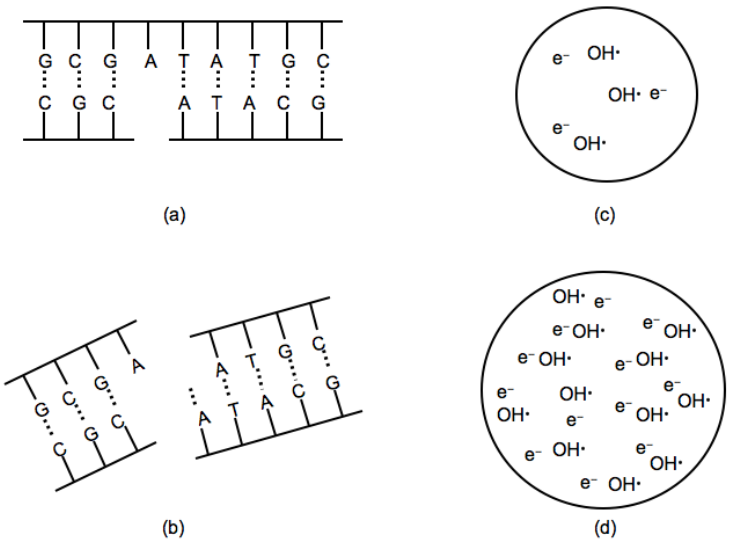

Figure 1.4: (a) Schematic of a single strand break (SSB) (b) Schematic of a double strand break (DSB) (c) Spurs contain 3 electrons (e^-) and 3 hydroxyl radicals (OH·) and have a total energy of up to 100 eV (d) Blobs contain 12 electrons and 12 hydroxyl radicals, with a total energy ranging from 100-500 eV.

.

the DNA molecule may snap in half, resulting in a double-strand break (see figure 1.4(b)). This type of damage is more rare than SSBs, but much more serious as it is not as easily repaired, and can lead to mutations, carcinogenesis and even cell death. Because the DNA of a given cell is replicated and passed on to the daughter cell during replication, DNA damage and misrepair is inherited also, meaning that carcinogenesis and mutations may manifest themselves in later generations. Cell death, on the other hand, will occur either in the damaged cell, or in its daughter, due to the damaged DNA [21].

When SSBs or DSBs are induced in a DNA molecule, they will likely be due to a combination of both free radicals and directly ionizing particles, such as electrons. Collections of radicals and electrons can cause significant damage to DNA, and it is common for radiation chemists to classify these groups of particles as *spurs*, *blobs*, and *short tracks*. These classifications correspond to increasingly larger and more energetic groups of free radicals and electrons, with spurs being the smallest and

least energetic. Spurs are responsible for approximately 95% of the energy deposition events caused by x-rays, and are defined as containing up to 100 eV of energy [21]. On average, each spur contains three free radicals and three electrons (see figure 1.4(c)) and is about 4 nm in diameter, which is approximately twice the diameter of the double helix of DNA [21]. Due to the size of a spur, radical attack and ionization can occur at multiple sites throughout the DNA double helix. This can result in SSBs and DSBs, as well as damage to the individual bases, which can produce modified base products [22–25].

Ultimately, ionizing radiation has a significant effect on the structure of DNA. Alongside the SSBs and DSBs, the radiation damage will result in the destruction of the hydrogen bonds connecting the base pairs, resulting in the separation, or the *denaturation* of the DNA strands. Bonds involved in base stacking will also be damaged, and the conformation of the DNA will be affected. In fact, it has been suggested that the initial conformation of the DNA can act to shield the bases interior to the double helix from damage, and as the DNA is unravelled, base damage increases [26]. The understanding of ionizing radiation-induced damage to DNA improves as methods of observing and quantifying this damage continue to develop. A brief overview of some of these methods is contained in section 1.2.4.

1.2.3 Tissue Response to Ionizing Radiation

As was mentioned in the previous section, radiation-induced effects to DNA play a significant role in whether or not a cell continues to proliferate, mutates, or dies due to radiation exposure. In radiation therapy, the death of tumour cells is the goal, but the effect of radiation on healthy tissue is a significant concern. Despite great achievements in the ability of modern radiotherapy to target cancerous tissue, it is important to understand how the healthy tissue is affected, as it is not yet possible to completely shield it from the radiation. Biological effects to tissues due to radiation are highly variable, and before they can be fully understood, it is necessary

to know how energy is transferred from the radiation to the exposed tissue. A detailed description of this process is given in standard texts [4, 5], but, ultimately the quantity used to describe the amount of energy deposited by ionizing radiation in a given amount of tissue, or any material, is known as *dose*. This quantity is defined by the following ratio:

$$D = \frac{dE_{ab}}{dm} \tag{1.3}$$

where dE_{ab} is the amount of energy absorbed in the mass, dm, and dose is given in units of Gray.

Both tumours and healthy tissue are known to respond differently to radiation dose, and figure 1.5(a) shows theoretical dose-response curves for both cancerous and healthy tissue, displaying the percentage of tissue damage as a function of dose. As can be seen, both curves have a sigmoid (S) shape, with a threshold dose below which no damage occurs. Above this threshold dose, there is a sharp increase in tissue damage, until it begins to level off around 100%. In the case of figure 1.5(a), a favourable situation is shown, in which damage to the tumour occurs at a lower dose than that of the healthy tissue.

Unfortunately, dose-response curves are not easily determined experimentally, and the response curve of the tissue of a given individual is rarely known. Also, unlike the situation in figure 1.5(a), not all tumours are as ideally suited for radiation therapy. Depending on the type of tumour, it's location in the body, and the physiology of the patient, the dose-response curves of both the tumour and the surrounding healthy tissue can vary significantly. In some cases, due to the responses of the tumour and healthy tissue, it is not possible to damage the tumour without significant damage to the normal tissue. This may mean that radiation therapy is not suitable for treatment, but, it may still be possible in the right conditions. For example, large tumours are typically poorly supplied with oxygen, and it has been observed that in

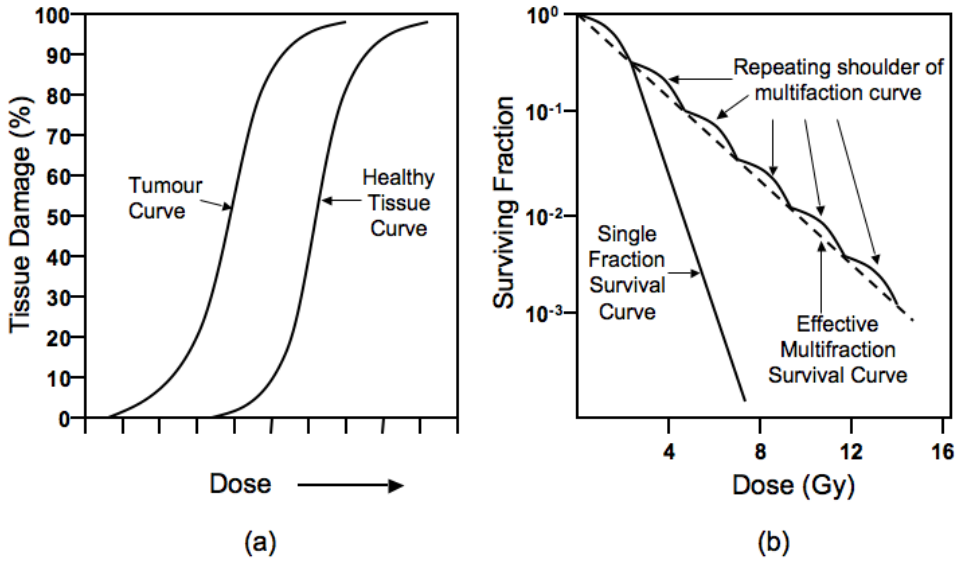

Figure 1.5: (a) Sample dose response curves of normal and cancerous tissue (b) Sample cell survival curve before and after fractionation.

the prescence of oxygen, the radiation-induced damage to the tumour is increased [4]. An increase in oxygen would not affect normal tissue, as it is all ready well supplied with oxygen, and, as a result, radiotherapy may now be an appropriate treatment. The use of a drug, such as a radiosensitizer, or chemotherapy agent can have a similar therapeutic benefit [21], so long as the drug increases tumour control sufficiently more than damage to normal tissue.

Another radiotherapy technique known to increase tumour damage while decreasing healthy tissue damage is known as *fractionation*. This involves dividing the total dose to be delivered to a tumour into a series of fractions which are delivered over an extended period of time, often weeks. Fractionation is based on the idea that healthy and cancerous tissue have different recovery rates from radiation-induced damage, and, in general, normal cells recover faster than tumour cells [4]. Over the course of the treatment, the cumulative effect of the low dose fractions will result in severe damage to the tumour cells, while the healthy tissue will be able to recover.

Figure 1.5(b) shows an example of a tumour cell survival curve for both a single dose treatment, and a multifraction treatment. The survival curves are plotted as

survival fraction as a function of dose on a semi-logartithmic scale. The single dose survival curve has the standard form observed in mammalian cells [21] for sparsely ionizing radiation such as x-rays. It consists of an initially linear decrease at low doses, followed by a curved shoulder that extends over a small dose range, followed by another linear decrease at high doses. The effect of fractionating treatment means that the shoulder portion of the curve is repeated in each fraction, resulting in an effectively linear decrease over the course of the treatment. The effective survival curve is defined by a line extending from the origin through the point on the single dose survival curve corresponding to the dose fraction [21]. While this means that multifraction treatment requires a higher dose to kill the cancerous cells than a single dose treatment, the fractionated method greatly benefits the survival of the healthy tissue exposed to radiation throughout the treatment.

1.2.4 Observation of Radiation-Induced DNA Damage

The analysis of radiation-induced damage in DNA has long been a topic of interest in radiation biology, and advances in analytical techniques have allowed researchers to ascertain the importance of DNA damage on the biological effects of radiation exposure, such as tissue damage. Studies have been done both on cellular DNA (*in vivo*), and isolated DNA prepared in a lab, usually in solution (*in vitro*). Typically, samples observed *in vitro* are easier to deal with and control, and thus much work has been done on "free" DNA. Early work in identifying the base damage products of irradiated DNA involved using acidic or enzymatic hydrolysis to release the products from the DNA molecule, and then some form of chromatography to separate them from the rest of the solution. Hydrolysis is essentially the breaking down of a chemical by its reaction with water, while chromatography is a technique typically used for the separation of a mixture into it's components by exploiting how these components move at different rates as they are passed through a medium. Several forms of chromatography have been used to differentiate between base damage products in-

cluding *thin-layer chromatography* [22, 23], *high performance liquid chromatography* [22, 23], and *gas chromatography*, which was used in conjunction with *mass spectrometry* [24, 25]. These techniques have been used in the study of radiation-induced damage to DNA both *in vitro* and *in vivo*, and reviews of some of the earlier studies are found elsewhere [22, 23].

The determination of the number of DSBs in irradiated DNA has also been studied extensively using techniques such as gel electrophoresis, which is still commonly used today. In this technique, either DNA isolated from irradiated cells, or "free" DNA is passed through a gel under the influence of an electric field [21]. The smaller pieces of DNA move more quickly and further into the gel than larger pieces, and thus damaged DNA can be easily separated and identified. As an example, *pulsed-field gel electrophoresis* (PFGE) has been used to study radiation-induced DSBs in the DNA of Chinese hamster ovary (CHO) cells [27]. Similarly, PFGE has been used in conjunction with standard agarose gel electrophoresis (SAGE) and thermal transition spectrophotometry to study the effects of radical scavengers on radiation-induced DSBs in calf-thymus DNA [28].

More recently, spectroscopic techniques have proven useful in the study of ionizing radiation-induced damage to DNA. Raman spectroscopy, in particular, has shown promise, and is described in more detail in the following chapter. This type of spectroscopy allows for the detailed molecular analysis of DNA samples, and can easily detect structural changes, without the need to alter the sample through time-consuming techniques such as hydrolysis. While not yet used extensively in the analysis of ionizing radiation-induced damage to DNA, existing studies involving both isolated DNA and tissue samples show promising results. For example, Fourier transform (FT) Raman spectroscopy has been successfully used in the identification of radiation-induced damage to calf-thymus DNA [29], while standard Raman spectroscopy has been used to study radiation-induced damage to both the normal and tumourous tissue of mice

and humans [30, 31]. These results, alongside it's relative ease of implementation, imply that Raman spectroscopy will be a useful tool in the analysis of radiation-induced damage in DNA, and an attractive complement to the currently used methods.

1.3 Thesis Scope

In keeping with the goal of radiation therapy to kill tumour cells while having a minimal effect on the healthy tissue of a patient, it is critical to understand the effects of radiation on our internal biology, particularly as radiotherapy becomes more widely used in the treatment of cancer and treatments become more complex. As it is known that the biological effects of radiation are highly dependent on the radiation damage to DNA [21], it seems that understanding the effects of ionizing radiation on DNA is a logical place to start. While there have been many studies on the effects of ionizing radiation on DNA, as mentioned in section 1.2.4, they were primarily concerned with quantifying DNA damage. This work looks to add to the current base of information with a detailed study of the effects of radiation on DNA at the molecular level, assigning radiation-induced damage to particular molecules, or sub-groups of larger molecules (referred to as *moieties*). This is achieved through the study of irradiated and unirradiated DNA with ultraviolet resonance Raman spectroscopy (UVRRS), which has not previously been attempted.

UVRRS is an easily implemented molecular level probe that requires no modification of an aqueous DNA sample before analysis. It has already been successfully used in the study of both genomic DNA [32, 33] and short DNA oligomers [34–36], but has not yet been used in the study of ionizing radiation-induced damage to DNA. However, the nucleotides of DNA are near resonance in the ultraviolet spectrum of light [37], and thus UVRRS provides detailed information about the molecular changes in the bases of DNA due to radiation. The use of FT-Raman spectroscopy to identify the radiation-induced damage of calf-thymus DNA [29] has already provided encouraging

results, allowing for the identification of base unstacking, structural modifications of the bases and backbone, conformational changes and strand breaks. The analysis of radiation-induced DNA damage with UVRRS presented here looks to expand upon this work, with the added benefit of a more intense signal and high sensitivity to the nucleotides.

As there is currently little information on the use of UVRRS in the study of ionizing radiation-induced damage to DNA, this investigation assesses the feasibility of the idea, and attempts to understand the information that can be obtained in this way. A reproducible technique of spectral acquisition and analysis is described, which took inspiration from other Raman studies of DNA, including work involving the use of UVRRS to determine UV radiation-induced damage to DNA [38–40]. In an attempt to understand whether DNA sequence length has a significant effect on the type and extent of radiation-induced damage, spectra of irradiated and unirradiated calf-thymus DNA (CT-DNA) and a simple short-stranded oligonucleotide (SS-DNA) are analyzed. Knowing that the UVRR cross sections of the DNA bases are highly dependent on incident UV wavelength [33, 37], spectra of the DNA samples acquired at multiple incident wavelengths are considered, with the resultant molecular specificity allowing for a more detailed understanding of the moieties being affected by the radiation. The ionizing radiation-induced spectral differences that were observed in spectra of both the SS and CT-DNA are described in detail, and an emphasis is placed on sequence dependent differences. Information that could only be determined when using a particular incident UV wavelength is highlighted, and the utility of UVRRS with multiple incident wavelengths in the study of radiation-induced damage to DNA is discussed.

Chapter 2

Raman Spectroscopy

This chapter provides an introduction to the idea of Raman spectroscopy, beginning with a brief history (section 2.1), followed by a summarized theory (section 2.2) of normal and ultraviolet resonance Raman scattering. The information provided by a Raman spectrum is discussed (section 2.3), and a brief overview of the instrumentation necessary to acquire a spectrum is given (section 2.4). Issues such as spectral resolution (section 2.5), and the strengths and weaknesses of Raman spectroscopy (section 2.6) are considered, and the chapter concludes with a discussion of some of the applications of this type of spectroscopy (section 2.7).

2.1 History

The inelastic scattering of light, now known as Raman scattering, was first hypothesized by Smekal in 1923 [41], but was not observed experimentally until 1928, when it was discovered by Sir Chandrasekhra Venkata Raman and K.S. Krishnan [42]. In his initial experiment, Raman used a telescope to focus sunlight onto a sample of either a purified liquid or its dust-free vapour. Using a series of complementary optical filters, Raman and Krishnan were able to observe scattered light of a differing frequency from the incident light. It was described as an optical analogue to the Compton scattering of x-rays. The effect was named after Raman, and he received the Nobel Prize in physics for its discovery in 1930.

After the discovery of the Raman effect, initial studies focused on improvement of the excitation source. Initially, lamps of elements such as helium, bismuth, lead, zinc and mercury were developed [43–45], but most of these proved insufficient due to low light intensities. Various types of instrumentation for the detection of Raman scattering were also investigated, beginning with photographic plates. The time required to develop these plates made the process inefficient, and it wasn't long before photoelectric detectors were designed after the beginning of World War II [46]. In the early 1950s, photomultipiers were implemented into the detection instrumentation [47].

The use of lasers in Raman spectroscopy, first reported in 1962 [48], greatly improved upon the technique, as lasers provided a high power, monochromatic and easily focused excitation source. The introduction of continuous wave ion lasers and pulsed lasers provided sources with wavelengths ranging from the ultraviolet (UV) to the infrared (IR) regions of the spectrum. Experimental advances continued as the use of monochromators improved the efficiency of light collection. With improvements in diffraction gratings, double and triple monochromators were introduced, and eventually holographic gratings appeared in 1968 [49].

Today, these developments have culminated to produce the current state of the art Raman instrumentation. There are several types of Raman spectroscopy performed today, such as Fourier transform (FT) Raman, ultraviolet resonance Raman (UVRR) and surface enhanced Raman spectroscopy (SERS). Each method has its own advantages and disadvantages, and together they are an invaluable tool in both academic and industrial research.

2.2 Theory

2.2.1 Raman Scattering

When a molecule with vibrational energy levels v = $0, 1, 2, 3, \ldots$ (see figure 2.1) is irradiated by a light source of frequency ν_0, and energy $h\nu_0$ (where h is Planck's constant), the incident photons are scattered both elastically and inelastically. The elastically, or Rayleigh scattered radiation has the same frequency as the incident light, while the inelastically, or Raman scatter light is of a different frequency, ν' and energy, $h\nu'$. Most of the light will be Rayleigh scattered, while only 1 in $\sim 10^6$ to 10^8 photons will undergo Raman scattering [50]. Of the Raman scattered light, some will have a frequency of $\nu' = \nu_0 - \nu_n$ (termed Stokes scattering), and the rest will have a frequency of $\nu' = \nu_0 + \nu_n$ (termed anti-Stokes scattering). The frequency ν_n corresponds to the energy difference $h\nu_n$ between two consecutive vibrational energy levels of the irradiated molecule. Figure 2.1 shows a schematic of this effect where ν_n corresponds to the frequency difference between the ground state and first excited vibrational state.

The energy of the incident light is normally chosen such that it will not excite the molecule into its first excited electronic state (ψ_1), and instead the molecule is excited from its ground state ψ_0 to a virtual energy state, before relaxing back to ψ_0 (see figure 2.1). In resonance Raman spectroscopy, the excitation source is tuned to the energy difference between ψ_0 and ψ_1, as will be discussed in section 2.2.2.

The presence of Raman scattered light can be explained using classical theory. To begin, the excitation source (typically a laser), is described in terms of its electric field strength, $\mathbf{E}$. If the laser has frequency ν_0, then its electric field strength will fluctuate with time as follows:

$$\mathbf{E} = \mathbf{E_0} \cos 2\pi\nu_0 t \tag{2.1}$$

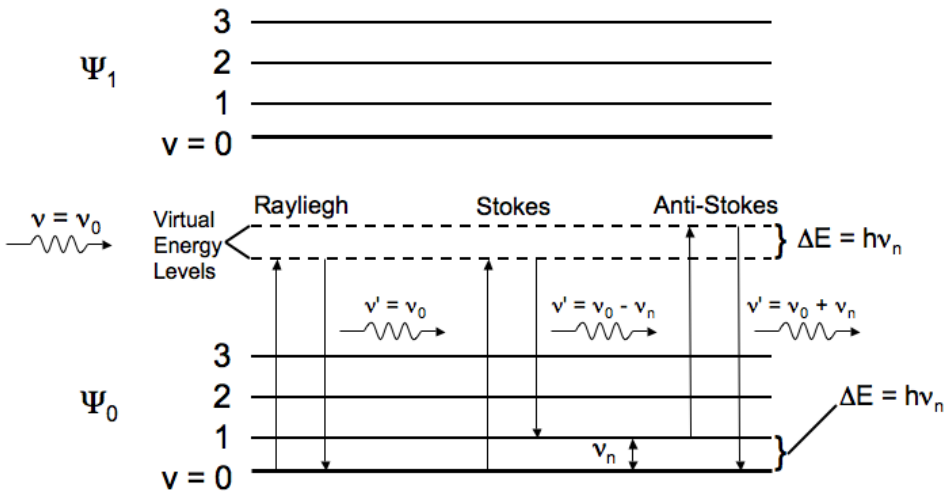

Figure 2.1: Schematic of Rayleigh scattering and Stokes and anti-Stokes Raman scattering

where $\mathbf{E_0} = (E_{0x}, E_{0y}, E_{0z})$ is the maximum amplitude of the electric field, ν_0 is the frequency, and t is the time. When a molecule is exposed to this field, a separation of charge is produced, and a dipole moment, $\mathbf{P}$, is induced, as described by:

$$\mathbf{P} = \alpha \mathbf{E} \tag{2.2}$$

where α is a proportionality constant called the polarizability. Because both $\mathbf{P}$ and $\mathbf{E}$ are vectors, equation 2.2 can be written in matrix form (in cartesian coordinates) as follows:

$$\begin{bmatrix} P_x \\ P_y \\ P_z \end{bmatrix} = \begin{bmatrix} \alpha_{xx} & \alpha_{xy} & \alpha_{xz} \\ \alpha_{yx} & \alpha_{yy} & \alpha_{yz} \\ \alpha_{zx} & \alpha_{zy} & \alpha_{zz} \end{bmatrix} \begin{bmatrix} E_x \\ E_y \\ E_z \end{bmatrix} \tag{2.3}$$

The matrix containing the polarizability components is called the polarizability tensor, and it is symmetric in normal Raman scattering.

If the irradiated molecule is vibrating with a frequency ν_n, then the nuclear displacements, q_i, can be written as:

$$q_i = q_{i0} \cos 2\pi\nu_n t \tag{2.4}$$

where q_{i0} is the maximum vibrational amplitude for the i^{th} coordinate, q_i. The polarizability is related to these nuclear displacements, and for small q_{i0}, α can be written as a linear function of q_i:

$$\alpha = \alpha_0 + \left(\frac{\partial\alpha}{\partial q_i}\right)_0 q_i + \ldots \tag{2.5}$$

where α_0 is the polarizability at the equilibrium position of the molecule, and $(\partial\alpha/\partial q_i)_0$ is the rate of change of α with respect to q_i, evaluated at the equilibrium position. If equations (2.5) and (2.1) are substituted into equation (2.2), the polarizability can be written as:

$$\begin{aligned} \mathbf{P} &= \alpha \mathbf{E_0} \cos 2\pi\nu_0 t \\ &= \alpha_0 \mathbf{E_0} \cos 2\pi\nu_0 t + \left(\frac{\partial\alpha}{\partial q_i}\right)_0 q_i \mathbf{E_0} \cos 2\pi\nu_0 t \end{aligned} \tag{2.6}$$

Inserting equation (2.4) for q_i in the above equation gives:

$$\mathbf{P} = \alpha_0 \mathbf{E_0} \cos 2\pi\nu_0 t + \left(\frac{\partial\alpha}{\partial q_i}\right)_0 q_{i0} \mathbf{E_0} \cos\left(2\pi\nu_n t\right) \cos\left(2\pi\nu_0 t\right) \tag{2.7}$$

Finally, using the trigonometric identity $2\cos A \cos B = \cos\left(A+B\right) + \cos\left(A-B\right)$ gives:

$$\mathbf{P} = \alpha_0 \mathbf{E_0} \cos 2\pi\nu_0 t + \frac{1}{2}\left(\frac{\partial\alpha}{\partial q_i}\right)_0 q_{i0} \mathbf{E_0} \{\cos\left[2\pi(\nu_0 - \nu_n)t\right] + \cos\left[2\pi(\nu_0 + \nu_n)t\right]\} \tag{2.8}$$

From equation (2.8) it is possible to see terms that represent both Rayleigh and

Raman scattering. The first term represents an oscillating dipole that scatters light at the same frequency (ν_0) as the incident light, and corresponds to Rayleigh scattering. The second term corresponds to Raman Stokes scattering, in which the scattered frequency ($\nu_0 - \nu_n$) is less than the incident frequency of the light, and the third term relates to Raman anti-Stokes scattering, in which the scattered frequency ($\nu_0 + \nu_n$) is greater than that of the incident light. Equation (2.8) also shows that if the partial derivative $(\partial\alpha/\partial q_i)_0$ is equal to zero, no Raman scattering will be observed. Thus, if a molecular vibration is to be Raman-active, the derivative of at least one of the components of the polarizability tensor (equation (2.3)) must be nonzero.

Classical theory predicts the intensity of Stokes and anti-Stokes scattering to be equal. However, experimentally, this is found to not be the case. Stokes scattering is much more intense than anti-Stokes, and the explanation for this comes from the initial populations of the vibrational states [20]. As can be seen in figure 2.1, Stokes scattering originates with electrons excited from a low energy vibrational state, while anti-Stokes scattering originates in those excited from higher energy vibrational states. The Maxwell-Boltzmann distribution law states that at room temperature, the lower energy vibrational states are much more populated than higher vibrational energy levels. As a result, Stokes scattering is more intense than anti-Stokes scattering at room temperature. Both types of Raman scattering experience the same magnitude of frequency shift, ν_n (see figure 2.1), and thus contain the same information about the molecule. Because of it's higher intensity, Stokes scattering is typically measured in Raman spectroscopy.

The intensity of the Stokes scattered radiation arising from a vibrational transition from state m to state n (see figure 2.2) is given by the following equation:

$$I_{mn} = k * I_0 * (\nu_0 - \nu_{mn})^4 \sum_{p\sigma} |(\alpha_{p\sigma})_{mn}|^2 \tag{2.9}$$

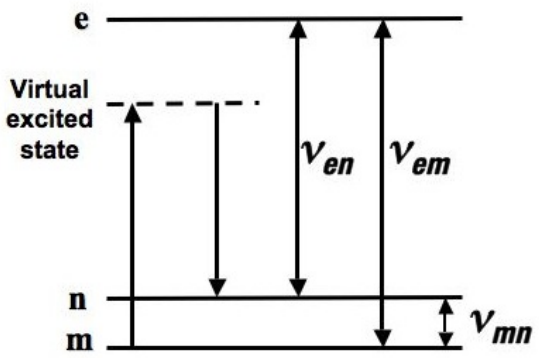

Figure 2.2: Energy Level Diagram: States m and n are vibrational states of the ground electronic state, and state e is an electronic excited state.

where k is a constant, I_0 and ν_0 are the intensity and frequency of the incident light, respectively, and ν_{mn} is the frequency difference between the initial and final vibrational states (see figure 2.2), equivalent to ν_n in figure 2.1. The term $(\alpha_{p\sigma})_{mn}$ represents the change in the polarizability caused by the transition from an initial state m through to a virtual excited state and back to a final state n (see figure 2.2). In this term, p and σ correspond to the incident and scattered polarization directions, respectively. Equation (2.9), shows that the intensity, I_{mn}, is proportional to the fourth power of the frequency of the scattered light, $\nu_0 - \nu_{mn}$.

In order to better understand equation (2.9), it is necessary to consider the term $(\alpha_{p\sigma})_{mn}$, described by the Kramer Heisenberg Dirac (KHD) expression, which is defined as:

$$(\alpha_{p\sigma})_{mn} = \frac{1}{h}\sum_{e}\left(\frac{M_{me}M_{en}}{\nu_{em} - \nu_0 + i\Gamma_e} + \frac{M_{me}M_{en}}{\nu_{en} + \nu_0 + i\Gamma_e}\right) \tag{2.10}$$

Here, ν_{em} represents the frequency corresponding to the energy difference between the initial state, m, of the molecule and a given electronic excited state e, while ν_{en} describes the energy difference between state e and the final state, n (see figure 2.2). The term $i\Gamma_e$ is a small factor relating to the lifetime of the virtual excited

state that was induced by the excitation source. Because the virtual state is not an actual electronic state of the molecule, it is described by a sum over all the electronic states of the molecule, e. Each excited state is involved in the terms M_{me} and M_{en} in equation (2.10) and these terms are called electric transition moments [20]. In a sense, these terms mix their subscripted states to describe the distorted electron cloud of the virtual excited state of the molecule. The electric transition moments are integrals over all time, τ, and, as an example, M_{me} is defined as:

$$M_{me} = \int \Psi_m^* \mu_\sigma \Psi_e d\tau \tag{2.11}$$

where Ψ_m and Ψ_e are wavefunctions of the subscripted states, and μ_σ is the σ component of the electric dipole moment. A more thorough discussion of the KHD expression is beyond the scope of this thesis, but can be found elsewhere [20, 50–54]

2.2.2 Resonance Raman Scattering

As can be seen in equation (2.9), the intensity of the Raman scattered light, I_{mn}, depends on both the intensity and frequency of the light incident on the molecule. In the case of *resonance Raman scattering*, ν_0 is chosen specifically so that it corresponds to an electronic transition of the molecule to be excited. In this case, the intensity of the scattered Raman light can be enhanced by a factor of 10^3 to 10^5 over that of normal Raman scattering [20]. This is evidenced by the denominator of the first term in equation (2.10). As ν_0 gets close to the frequency ν_{em} corresponding to the electronic transition between states m and e, the denominator becomes small, and is dominated by the term $i\Gamma_e$, which is a small energy term. The fraction then becomes very large, and as a result, so does I_{mn}. In this case, although $(\alpha_{p\sigma})_{mn}$ is summed over all possible states, e, the state corresponding to the transition to which ν_0 has been tuned, dominates the sum, and the resultant scattering depends very much on the properties of this state.

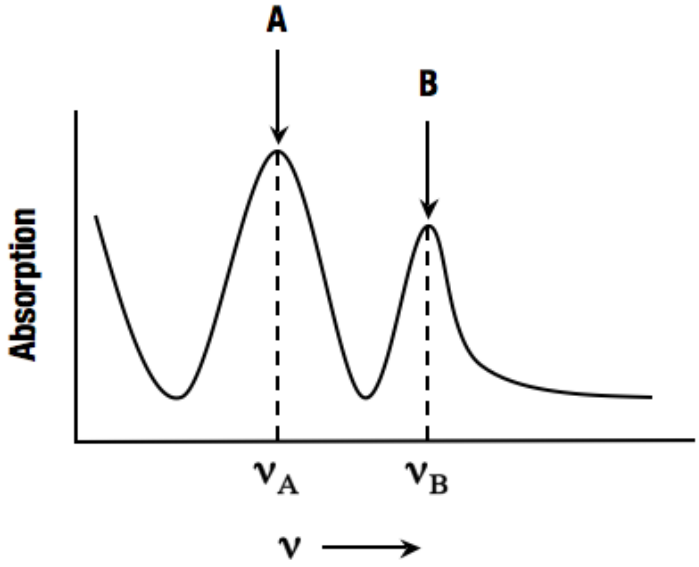

Figure 2.3: Absorption spectrum of a substance with resonant frequencies at ν_A and ν_B.

Aside from the large intensity increase, another benefit of resonance Raman scattering is it's molecular selectivity. For example, consider two moieties of a given molecule, A and B, that experience electronic transitions after absorbing energy corresponding to frequencies of ν_A and ν_B, as illustrated in the sample absorption spectrum of figure 2.3. If ν_0 is chosen close to ν_A, then moiety A will be resonantly enhanced, while if ν_0 is chosen close to ν_B, the same will be true for moiety B. This is a very useful property of resonance Raman scattering that is exploited in UVRR spectroscopy and will be used in this study, as described in Chapter 3, section 3.4.

To further understand the nature of resonance Raman scattering, the wavefunctions of the molecule are often considered as a product of separate electronic and vibrational wavefunctions, allowing the term $(\alpha_{p\sigma})_{mn}$ to be expressed as a sum of two terms. These terms are referred to as the A and B terms and relate to different types of resonance Raman scattering. The mathematics of this analysis are beyond the scope of this thesis, but a more thorough discussion of the topic can be obtained in references [20] and [50].

2.2.3 Molecular Vibrations and Normal Modes

In order to understand the Raman spectrum of a molecule, it is first important to understand the vibrations of the molecule, as Raman spectroscopy is a vibrational spectroscopy. While the vibration of a diatomic molecule is easily understood, since it occurs along the axis of the bond joining the two nuclei, the vibrations of polyatomic molecules are more complex. Each of the nuclei in a polyatomic molecule perform individual harmonic oscillations. However, the complicated vibrations of a polyatomic molecule can be expressed as the superposition of a series of completely independent "normal" vibrations. The number of normal modes of the molecule are related to it's *degrees of freedom*. Each atom in the molecule is free to move in the x, y, or z direction, and as such, it has 3 degrees of freedom. Therefore, the molecule will have $3N$ degrees of freedom, where N is the number of atoms in the molecule. Not all of these degrees of freedom are vibrational, however, as three correspond to translational movements of the molecule in the x, y and z directions, and three correspond to rotations of the molecule about the principal axes of rotation, which pass through the centre of gravity of the molecule. In the case of a linear molecule, however, there are only 2 rotational degrees of freedom, as the molecule can only rotate around it's principal axis of rotation, or about it. Taking the translational and rotational degrees of freedom of the molecule into account, an arbitrary polyatomic molecule has $3N-6$ degrees of freedom, while a linear polyatomic molecule has $3N-5$ degrees of freedom.

As an example of the normal modes of vibration, consider the molecule CO_2. It is a tri-atomic, linear molecule, and thus will have $3(3) - 5 = 4$ degrees of freedom. The four normal vibrations of the molecule are shown in figure 2.4. The first (figure 2.4(a)) is a symmetric stretch, the second and third are bending, or deformation modes (figure 2.4(b)), and the fourth is an asymmetric stretch (figure 2.4(c)). The bending modes are degenerate, in that they are essentially the same vibration, with

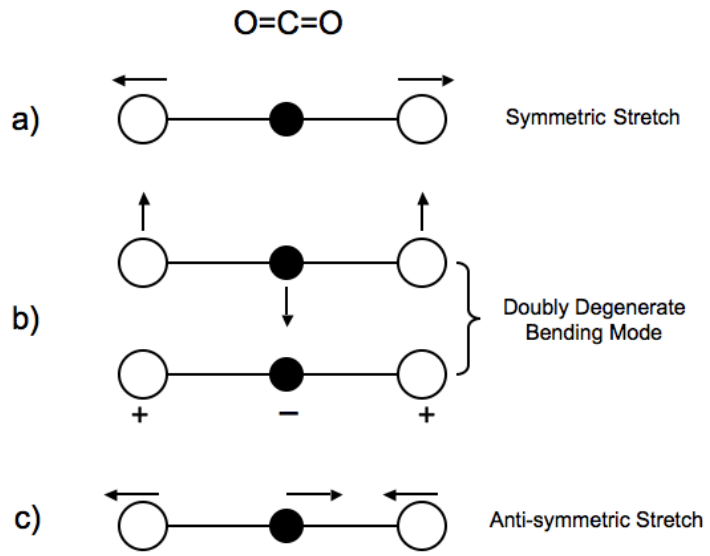

Figure 2.4: Normal modes of CO_2. In (b), the + indicates motion into the page and the − indicates motion out of the page in a direction perpendicular to the plane of the page.

the same frequency, but they occur in mutually exclusive planes separated by 90^o. Through the analysis of the change in polarizability throughout each vibration, it is possible to determine which vibrations are Raman active. In simple cases like this, Raman activity can be determined by plotting $1/\sqrt{\alpha_i}$ (where $i = x, y, z$) from the centre of mass in all directions. This gives a three-dimensional surface called a "polarizability ellipsoid." If, throughout the vibration, the size, shape or orientation of the ellipsoid changes, then it is said to be Raman active. Figure 2.5 shows the change in the polarizability ellipsoid for the vibrations of CO_2, and it is determined that only the symmetric stretch (figure 2.5(a)) is Raman active. While the size of the ellipsoid does change throughout the other two vibrations, they are the same at the two extremes of the vibration, and are thus not considered Raman active for small displacements. This is further illustrated by the fact that, for the bending mode and anti-symmetric stretch, the slope of the polarizability as a function of the atomic displacement, q, is zero at the equilibrium position (ie. $(\delta\alpha/\delta q)_0 = 0$), and thus the polarizability does not change for small displacements, as indicated in equation (2.8).

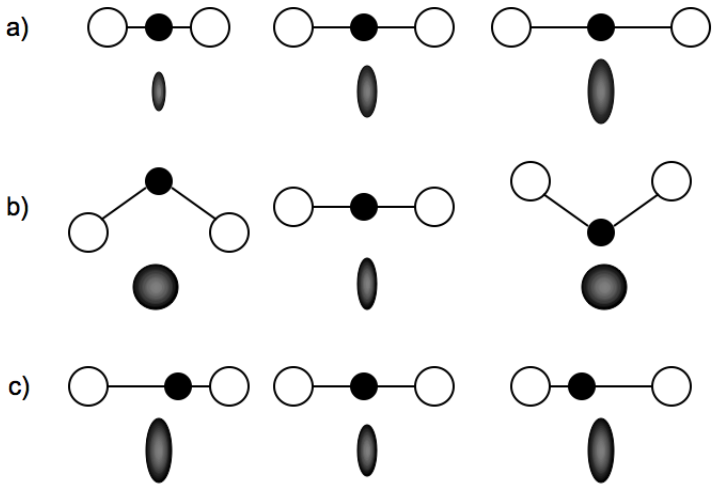

Figure 2.5: Polarizability ellipsoid ($1/\sqrt{\alpha_i}$, where $i = x, y, z$) for the normal vibrations of CO_2. In each case, the central configuration is the equilibrium position. (a) Symmetric stretch (b) Bending or deformation mode (c) Anti-symmetric stretch

While an analysis of the polarizability is straightforward for a small molecule like CO_2, for larger molecules, it is much more complicated, and it is necessary to use group theory and quantum mechanics to determine the Raman activity of a vibration. When these methods are applied, it can be shown [20, 55], that the selection rules are determined by the following set of integrals:

$$[\alpha_{ij}]_{v,v'} = \int \Psi_v^*(q_a)\alpha_{ij}\Psi_v'(q_a)dq_a \tag{2.12}$$

where $i = x, y, z$, $j = x, y, z$, α_{ij} are the components of the polarizability tensor as in equation (2.3), Ψ_v and Ψ_v' are the wavefunctions of the ground vibrational state v and the excited vibrational state v' respectively, and q_a is the normal coordinate for vibration a. A vibration is only considered Raman active if at least one of the nine integrals described in equation (2.12) is nonzero. This depends primarily on the symmetry of the vibration in question. A more detailed discussion on the selection rules, and symmetry analysis can be found in rerference [55], but is beyond the scope of this thesis.

2.3 Raman Spectrum

In Raman spectroscopy, the light scattered from the Raman active vibrations in a molecule is collected and its intensity is plotted as a function of the frequency shift of the scattered light as compared to the frequency of the incident light (ν_0). Typically, the frequency is in the units of *wavenumber*, $\bar{\nu}$, which is defined as the inverse of the wavelength of the light, $\bar{\nu} = 1/\lambda$, and is expressed in the units cm^{-1}. Therefore, the abscissa of a Raman spectrum is also plotted in units of cm^{-1}, however, it is important to remember that this corresponds to a frequency shift, and thus the abscissa is often labeled as the "Raman shift". Because wavenumber is proportional to the energy of the light ($E = h\nu = hc\bar{\nu}$, where h is Planck's constant), the cm^{-1} units of the abscissa correspond to the energy of the vibrations from which the Raman light was scattered. While the energy ranges of many standard vibrations are known [50], the assignment of a peak in a Raman spectrum to a specific vibration is not typically possible. In many cases, several molecules participate in a group vibration, and it is the vibration of the group that is observed in the spectrum, not the vibration of the specific molecular bonds that participate in the group vibration.

A more detailed discussion of how to approach the assignment of Raman spectral peaks is given elsewhere [50], but in general, in the assignment of peaks in a Raman spectrum it is often necessary to cross reference experimental spectra with spectra of standard substances, or to use theoretical considerations to determine the energy, and thus peak position, of particular vibrations. It is also useful to consult published works on the topic of Raman spectroscopy, because, since it's inception, Raman spectroscopy has been used to study many different substances and in most cases, specific assignments to spectral peaks have been made. In this work, references to previously published works on the Raman spectroscopy of DNA have been used to aid in the molecular assignment of the peaks in the various spectra acquired.

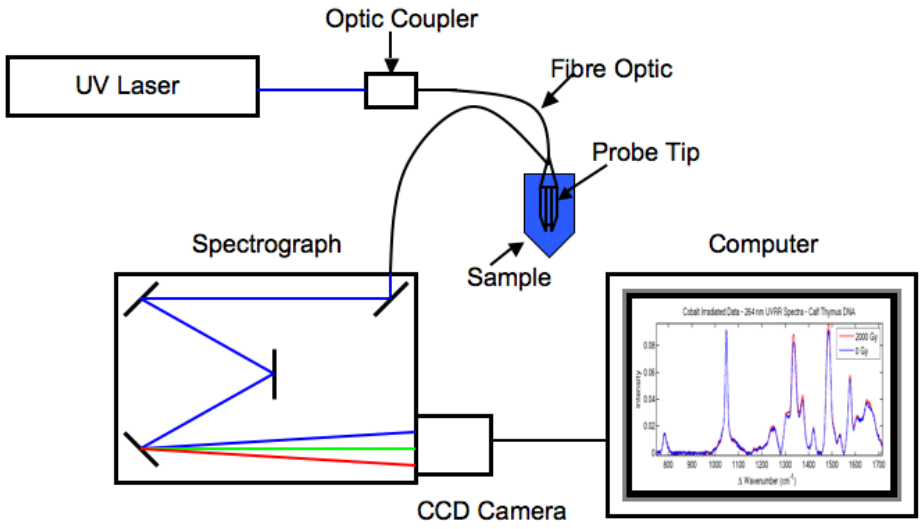

Figure 2.6: Schematic diagram of a fibre optic based UVRR Spectrometer

2.4 Raman Instrumentation

This section contains a brief overview of the main components necessary to construct a fibre optic based ultraviolet resonance Raman spectrometer. A schematic of the components is shown in figure 2.6. Essentially, it consists of a UV ion laser used as an excitation source, which is focused onto a fibre optic and passed into the sample. Scattered light from the sample is collected by a series of optic fibres and is passed into the spectrograph, where the light is separated into its component wavelengths. Light is then incident on a CCD (charge-coupled device) camera, where the light is converted to a digital signal and stored in a personal computer.

2.4.1 Ultraviolet Ion Laser

As an excitation source, lasers are now the standard for Raman spectroscopy. Using a laser allows the benefits of having a highly monochromatic source with minimal beam divergence allowing small sample volumes to be irradiated easily. Laser wavelengths from the hard UV (<200 nm) to the near-infrared (≈1064 nm) are employed in Raman

spectroscopy, depending on the application. Often, continuous wave (CW) lasers are used, as opposed to pulsed lasers, which can produce dangerously high instantaneous powers. CW lasers provide a high power output (but low instantaneous power), good frequency stability, and a long operational lifetime [56].

In an CW ion laser, a gas such as argon or krypton is contained in a sealed tube, as in figure 2.7(a). An electric discharge is initiated in this tube, which ionizes the gas and produces electrons. The electrons from the discharge collide with other gas atoms, causing further ionization and exciting the electrons of the ions to a higher energy level. Some of the excited electrons will spontaneously relax to a lower energy state and release characteristic photons which will either cause further excitation, or will interact with other excited ions and cause them to relax and emit a photon of the same energy in a process called "stimulated emission." The emitted photons are reflected back and forth in the cavity of the laser between the high reflector and the output mirror, and pass through a wavelength selector prism that only allows the wavelength chosen by the operator to pass (see figure 2.7(a)). When there is a sufficient balance between excitation and emission in the laser cavity, a usuable laser beam will be produced and passed through the partially reflecting output mirror.

The characteristic wavelengths that are achieved in the CW ion lasers are typically in the visible range, and in order to obtain wavelengths suitable for UVRR spectroscopy, a technique called frequency doubling must be employed. This involves passing the fundamental wavelength beam (characteristic ion laser beam) through a frequency doubling material, which is typically a crystal, such as the beta-barium borate (BBO) crystal, as shown in figure 2.7(b) [57]. The crystal is a highly non-linear medium, and as the fundamental laser beam passes through the crystal, the frequency of the light is doubled in a process called "second harmonic generation", or SHG. After the light passes through the crystal, it must pass through the SHG output mirror (see figure 2.7(b)), which is highly reflective to any fundamental light

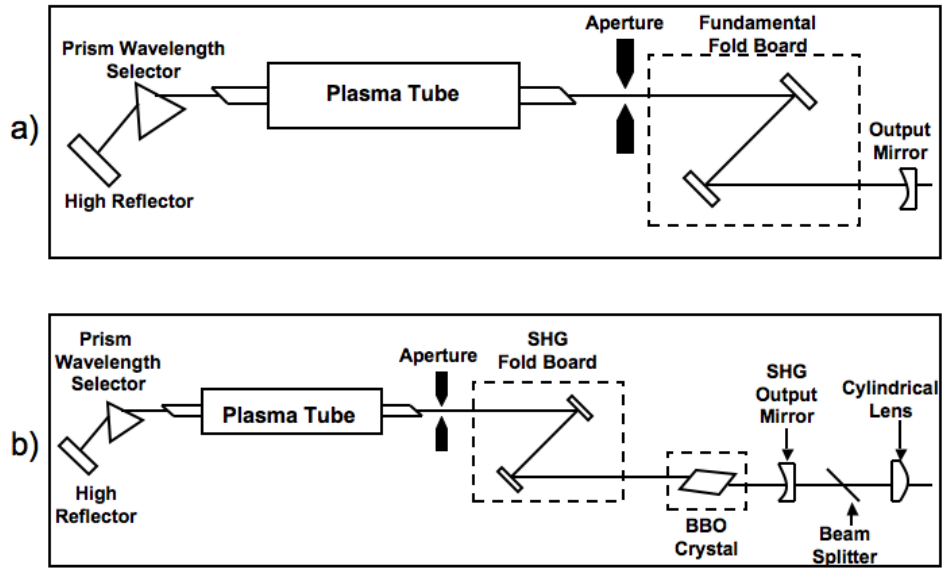

Figure 2.7: Continuous Wave ion laser schematics (a) Single-Line Operation (b) Second Harmonic Generation mode

that has passed through the crystal, and highly transmissive to the SHG light. The SHG light then passes through a cylindrical lens (see figure 2.7(b)) which recollimates the beam onto the vertical plane, where it can now be used as an excitation source for UVRR spectroscopy.

2.4.2 Sample Delivery and Collection

There are many possible methods of delivery of light from the excitation source to the sample, and of the collection of Raman scattered light. The methods chosen have a strong impact on the signal and the signal to noise ratio (SNR). Originally, the light was focused onto the sample and collected using a series of lenses in either a 90^o or 180^o geometry as shown in figure 2.8. The 90^o geometry (figure 2.8(a)) was quite common in early Raman spectroscopy, and it allowed the separate control of the laser and collection axes. However, it can be difficult to align the setup such that the scattered light is incident on the slit of the monochromator, and the 180^o geometry (figure 2.8(b)) has since become more common. In this case, the axis of the laser and the collection axis are the same. This provides convenience and gives

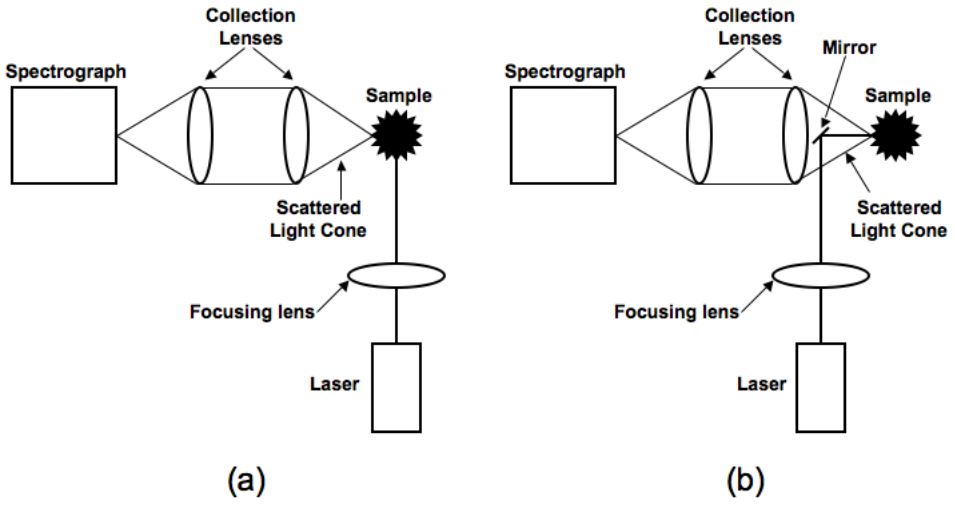

Figure 2.8: Common Raman light collection orientations. (a) 90^o orientation. (b) 180^o orientation.

reproducible results [56], while allowing for non-invasive sampling, in that the laser and thus the entire spectroscopic setup can be located at quite a large distance from the sample. The 180^o orientation also lends itself well to fibre optic Raman probes, which have greatly increased the versatility of Raman spectroscopy.

In a fibre optic Raman spectrometer (as shown in figure 2.6), incident laser light is focused through a lens onto an optical fibre that extends to the sample, where the tip may or may not be immersed. Because optical fibres transmit light very efficiently, the cables can be metres long, allowing large distances between excitation source and sample. The tip of the fibre optic probe that is immersed into the sample typically consists of a central excitation fibre, and a series of surrounding collection fibres [56] which transport the scattered light to the spectrograph. Figure 2.9(a) shows a common configuration consisting of 6 collection fibres surrounding a central excitation fibre. Laser light exits the central fibre in a cone, and backscattered light

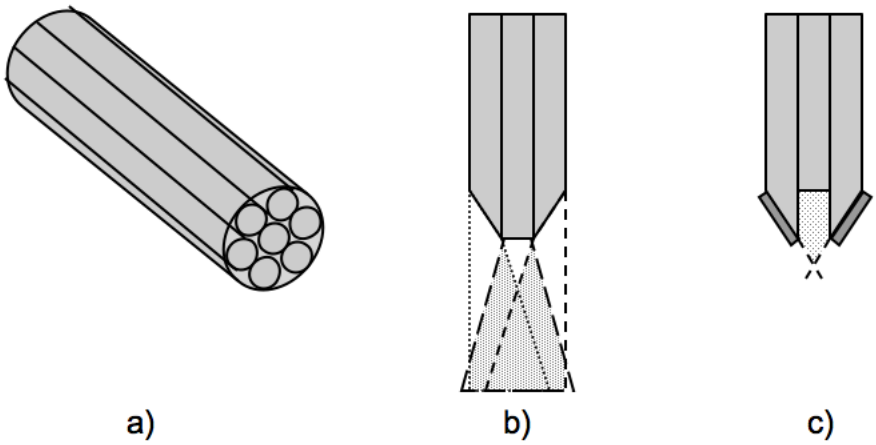

Figure 2.9: Fibre optic probes. (a) 6 collection fibres around 1 excitation fibre. (b) Bevelled probe tip - Dashed lines represent collection cones, and dotted region represents cone overlap. (c) Alternate 6 around 1 fibre bundle.

is collected by the surrounding fibres so long as it is scattered within the "collection cones" of the collection fibres. The collection cones are the same dimensions as the cones produced by light exiting the fibre. If the edges of the collection fibres are bevelled [56], as in figure 2.9(b), the collection cones are modified so as to increase overlap with the cone of the incident laser light. A useful modification of this bevelled probe involves slightly recessing the central excitation fibre and coating the bevelled edges of the collection fibres with aluminum, as in figure 2.9(c) [58, 59]. This is useful in situations in which the probe tip is immersed in a liquid sample, as it allows the effective collection of scattered light from the small volume enclosed by the collection fibres at an angle of 90^o to the axis of the excitation fibre. This probe is useful primarily for strongly absorbing samples, as it is designed to collect light that has been scattered within the enclosed volume where the excitation beam intensity is high, while light scattered beyond this volume is less likely to be collected.

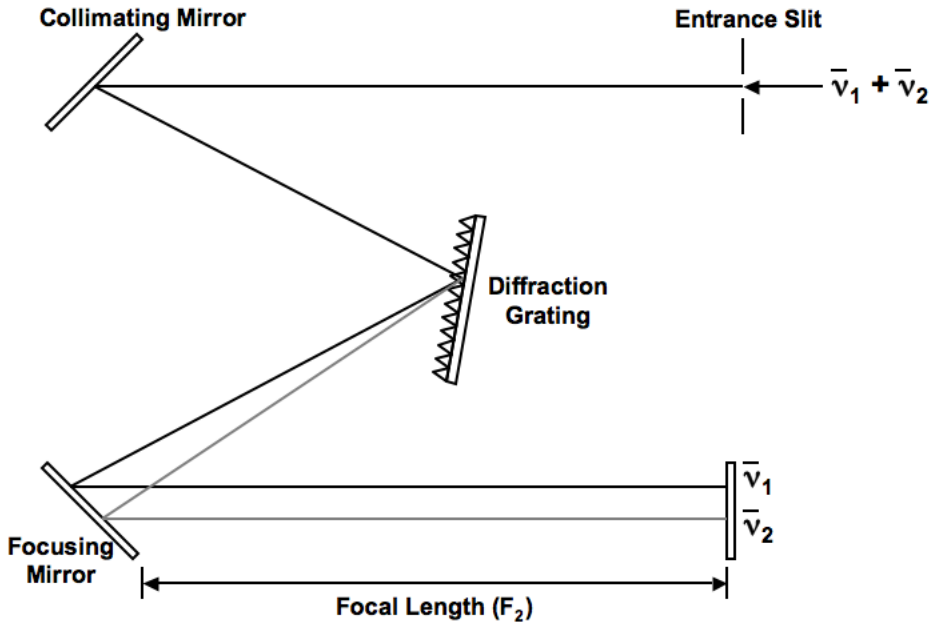

Figure 2.10: Schematic of a single grating Czerny-Turner spectrograph. Light composed of wavenumbers $\bar{\nu_1}$ and $\bar{\nu_2}$ is incident on the entrance slit, and split into it's component wavenumbers on the focal plane.

2.4.3 Spectrograph

After collecting the scattered signal, the different scattered wavelengths need to be separated in order to create a spectrum. Traditionally, this is done using either a dispersive or non-dispersive spectrometer. Non-dispersive spectrometers are typically used alongside long wavelength, NIR excitation sources, such as those used in FT-Raman spectroscopy . For excitation wavelengths in the visible and UV, dispersive spectrometers are typically used [56]. There are many different types of dispersive spectrometers, and initially, monochromators (single, double and triple) were used, but these forced the user to scan the dispersed signal one wavelength, or one channel, at a time. Today, multi-channel systems involving a spectrograph and a charge-coupled device (CCD) are common, and allow the detection of all of the dispersed signal at once.

Figure 2.10 shows a schematic diagram of a basic Czerny-Turner spectrograph [56]. In Raman spectroscopy, the collected Raman signal passes through the entrance slit of the spectrograph, and is reflected off of the collimating mirror onto the diffraction grating. When incident on the grating, the light is reflected at different angles depending on it's wavelength. The diffracted light is then reflected off of the focusing mirror onto the focal plane. The light on the focal plane is spatially separated depending on it's wavelength, according to the following equation:

$$\frac{d\lambda}{dl} = \frac{d \cdot \cos\theta}{mF_2} \tag{2.13}$$

where d is the separation between the grooves on the grating, m is the order of the diffraction, F_2 is the focal length of the focusing mirror, and θ is the angle at which the diffracted light leaves the grating. The term $d\lambda/dl$, typically in units of nm/mm, is referred to as the reciprocal linear dispersion, and describes the range of wavelengths covered in one length unit of the focal plane. To write equation (2.13) in terms of wavenumber $\bar{\nu}$, recall that:

$$\frac{d\lambda}{dl} = \frac{d(1/\bar{\nu})}{dl} = \frac{-1}{\bar{\nu}^2}\frac{d\bar{\nu}}{dl} \tag{2.14}$$

and then equation (2.13) can be written as follows:

$$\begin{aligned}
\frac{d\bar{\nu}}{dl} &= -\bar{\nu}^2\frac{d\lambda}{dl} \\
\frac{d\bar{\nu}}{dl} &= -\frac{d * \cos\theta * \bar{\nu}^2}{mF_2} \\
\frac{d\bar{\nu}}{dl} &= -\frac{d * \cos\theta(\bar{\nu_0} - \bar{\nu_n})^2}{mF_2}
\end{aligned} \tag{2.15}$$

where $\bar{\nu_0}$ is the wavenumber of the excitation source, and $\bar{\nu_n}$ corresponds to the Stoke's Raman shift. From equation (2.15) it can be seen that the reciprocal linear

dispersion varies with the square of the wavenumber of the scattered light, and thus, at the focal plane, the spectrum is non-linear. The angle of the diffraction grating can be adjusted in order to ensure that the desired wavenumber range is incident on the focal plane, and thus the CCD detector.

2.4.4 Light Collection

A CCD is a common type of multi-channel detector used in conjunction with a spectrograph in Raman spectroscopy. It utilizes the properties of a photosensitive semiconductor, usually silicon, to detect light in a two-dimensional optical array, and convert it to a digital signal. A circuit pattern of metal pads is deposited on the surface of the semiconductor, which define the spatial grid of the detector. When light is incident on the semiconductor chip, photoelectrons are produced which are attracted to the nearest metal pad of the circuit array, which is held at a positive potential. The number of photoelectrons produced is related to the intensity of the incident light and the time of exposure to the light, or "acquisition time". Spatial information is maintained as the electrons are attracted to the metal pad, or "pixel" of the array closest to their production.

When light incident on the CCD has first passed through a spectrograph, images of the entrance slit of the spectrograph separated by wavenumber are focused on the detector array, as shown in figure 2.11. The image of a certain wavenumber may be wider than one vertical row of pixels, depending on the width of the entrance slit, and thus the resolution of the acquired spectrum is limited by either the pixel width or the spectrograph entrance slit width, depending on which is larger. Regardless, pixels in a given column detect light of the same wavenumber, and their signal is often summed when a spectrum is acquired. The acquisition process is referred to as *readout*, and involves the variation of the potentials of the metal pads on the circuit array such that the signal from each pad is sequentially directed to the edge of the array one row at a time, where the signal of each column can be summed. The collected signal

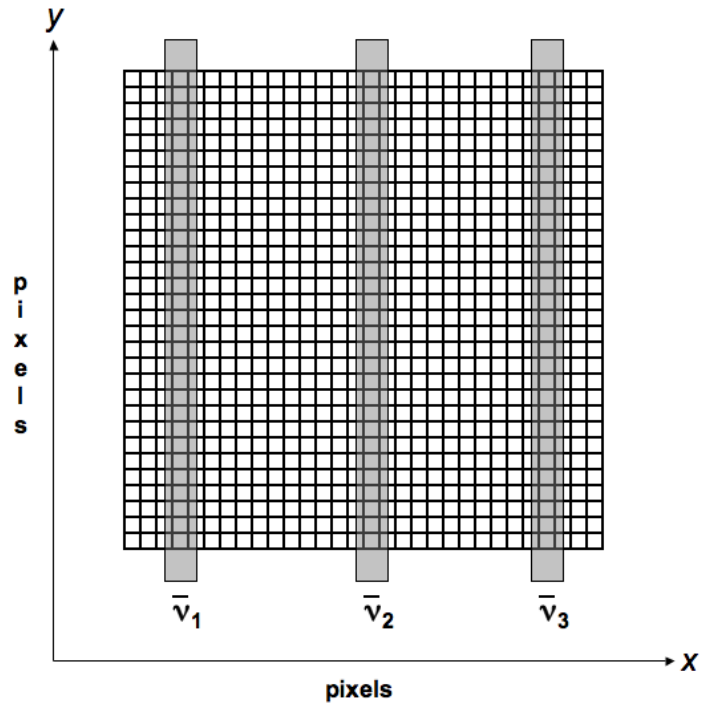

Figure 2.11: Schematic of a CCD Detector Array. Images of the spectrograph slit are spatially separated according to wavenumber ($\bar{\nu_1}, \bar{\nu_2}, \bar{\nu_3}$).

is then passed through an amplifier and is digitized by an analog-to-digital converter (ADC). Intensity can then be plotted on the computer as a function of individual pixel position to form a two-dimensional image, or as a function of pixel column (if the vertical columns have been summed) to form a one-dimensional spectrum.

While a CCD is very useful as a multichannel detector, it does have some sources of noise that must be taken into account. The most significant of these are *dark current, readout noise*, and *bias*. *Dark current* refers to signal collected by the detector array from spontaneously generated electrons produced at temperatures over 0^oC, and electrons resulting from defects in the semiconductor material. To minimize the effects of dark current, CCDs are typically cooled to well below zero before a spectrum is acquired. *Readout noise* occurs during the shifting of the electric signal of the metal pads, and the digitization of the signal. It is usually independent of the number of electrons being readout, and typically accounts for only a small number

of counts out of the total intensity signal [56]. In most acquired spectra, the signal is high enough that readout noise is negligible. Finally, *bias* is an offset signal usually added by the amplifiers in order to artificially rise the spectrum above the noise level. While typically constant for a given pixel, it may vary throughout the detector array [56]. However, it is easily removed by subtraction following spectral acquisition.

2.5 Spectral Resolution

As mentioned above, in section 2.4.4, the resolution of the spectrograph/CCD system is limited by either the entrance slit width of the spectrograph, or the pixel width of the CCD. The resolution of the system is given by:

$$d\bar{\nu} = \left(\frac{d\bar{\nu}}{dl}\right) W \tag{2.16}$$

where $d\bar{\nu}$ is the wavenumber incremental observed with a pixel, or entrance slit (whichever is the limiting factor) width, W. As the slit width can be arbitrarily small, so long as sufficient light intensity is permitted to pass, the pixel width is often the limiting factor, giving a resolution in units of cm^{-1}/pixel. Recall that the reciprocal dispersion, $d\bar{\nu}/dl$, varies with wavenumber, and thus depends on the region of the focal plane under investigation.

It is clear from equation (2.16) that when $d\bar{\nu}/dl$ is small (corresponding to a high dispersion), the spectral resolution is high, while when $d\bar{\nu}/dl$ is large (corresponding to a lower dispersion), the resolution is low. From equation (2.15) it can be seen that the dispersion may be adjusted by using a diffraction grating with a different spacing, d, or by changing the focal length, F_2, of the focusing mirror in the spectrograph. The focal length of a spectrograph is typically fixed, but the installation of varying diffraction gratings can easily be performed.

2.6 Strengths and Weaknesses of Raman Spectroscopy

Raman spectroscopy has proven to be useful in a variety of applications, a brief overview of which is included in the next section. This type of spectroscopy is attractive because it provides specific molecular information about a substance. The scattering is directly related to fundamental vibrational modes of molecules, and acquired spectra provide a unique fingerprint of a sample, with a high spectral resolution. Raman spectroscopy is also very versatile, and may be used to study a variety of samples in a non-destructive way, as the samples require no major modifications or preparation. Also, it is possible to study samples in a solid, liquid or gaseous form. The weak Raman scattering of water means that it will not interfere in the spectra of aqueous samples, and the same is true for glass, meaning that samples can be studied while in glass containers.

Although Raman scattering is a weak process, modern collection optics efficiently gather the scattered light, and through the use of processes such as resonance Raman scattering, the intensity of spectra can be greatly enhanced. Resonance Raman spectroscopy also provides a high degree of molecular selectivity, as the resonant vibrational mode is enhanced above others in the spectrum, allowing the identification of specific molecular bonds in large molecules.

The main limiting factors of Raman spectroscopy are related to fluorescence and sample degradation, caused by absorption of light from the excitation source. Raman scattering occurs too quickly for there to be significant energy absorption in a molecule [50], but, when operating close to resonance for a particular state of a molecule, energy absorption can occur. When this happens, the molecule relaxes to a lower energy state and releases energy through fluorescence, which results in the emission of photons of a broad range of frequencies, and is often stronger than the Raman signal. Fluorescence does not contain the vibrational information of Raman

scatter and thus its interference can limit the compounds investigated by Raman spectroscopy. It is also possible that energy absorbed in the sample from the excitation source is dissipated as heat, which can result in photodegradation of the sample. This is of particular significance in resonance Raman spectroscopy, but photodegradation can be reduced by minimizing exposure time to a particular region of the sample. In a liquid sample, this is achieved by rotating the sample container, causing a flow of the solution through the beam of the excitation source.

2.7 Applications of Raman Spectroscopy

Raman spectroscopy has found utility in a large variety of applications in both research and industry. It was initially used in the analysis of inorganic materials [50] but has since expanded to uses as diverse as the determination of the age of paintings using FT Raman spectroscopy [60], and the identification of components of plastic explosives in a fingerprint using SERS [61, 62]. It has also become very widely used in the analysis of polymers, and some of the more recent studies of polymers using Raman have been collected in the book by Painter *et al* [63]. Raman spectroscopy has also been used industrially as an on-plant monitor in many applications, including quality control for the production of protective diamond-like films for computer hard disks [64, 65], and reaction monitoring during the production of PCl_3 [66]. It has even been used to identify silicone deposited in human breast tissue from breast implants [67].

Due to the ability of Raman spectroscopy to study both solid and aqueous samples *in situ*, and it's ability to act as a molecular-level probe, Raman spectroscopy has also proven useful in a variety of biological applications [68]. Some of these applications include the study of bacterial spores [69], the characterization of microorganisms [70], and the analysis of benign and malignant human thyroid [71] and breast tissue [72, 73]. It has also been used to study ultraviolet radiation damage to herring

sperm DNA [38], and both UV [39] and ionizing-radiation [29] induced damage to calf-thymus DNA.

The high intensity and molecular specificity of resonance Raman spectroscopy have made it particularly useful in biological applications. It has been widely used to study heme-containing proteins [74, 75], such as hemoglobin and cytochromes, but has also shown great utility in the study of DNA [32–36]. Resonance Raman spectroscopy is also sensitive to substances such as non-heme oxygen carrying proteins such as hemerythrin [76, 77] and hemocyanins [78, 79], as well as carotenoids, which are present in carrots [80], human blood plasma [81] and other plants and animals.

As the applications of Raman spectroscopy are vast, it is not possible to describe all of its uses here, however, good general reviews can be found in books by Ferraro and Nakamoto [20] and Smith and Dent [50].

Chapter 3

Materials and Methods

The experimental procedure and data analysis process are described in detail throughout this chapter. Section 3.1 details the sample preparation process for the oligonucleotides and calf-thymus DNA used in this research, while the preparation of the DNA buffer is described in section 3.2. The various setups used for sample irradiation are discussed in section 3.3, and details of the irradiations performed using both a linear accelerator (section 3.3.1) and Co-60 radiotherapy unit (section 3.3.2) are given. Spectroscopic studies are then described, and, as with the irradiation process, several apparatus were used, including a UVRR spectroscopic setup (section 3.4.1), a Raman apparatus using a 785 nm laser (section 3.4.2), and a Raman microscope with a 632 nm excitation source (section 3.4.2). Finally, the data analysis process is discussed in section 3.5.

3.1 DNA Sample Preparation

3.1.1 SS-DNA

30-mer Oligonucleotides

Short stranded 30-mer oligonucleotides (oligos) were obtained from Integrated DNA Technologies (IDT, Coralville, IA). Complementary adenine and thymine strands were ordered, with guanine and cytosine attached to the ends of each strand (see

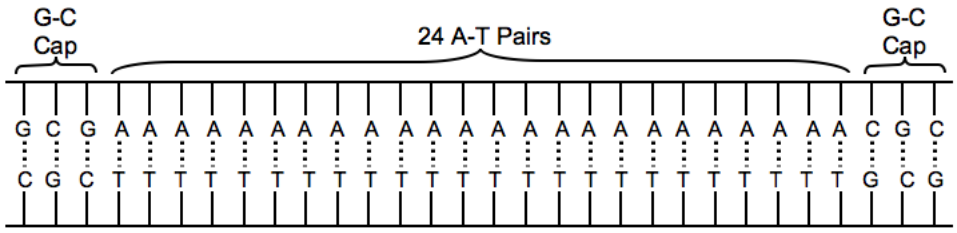

Figure 3.1: Schematic of 30-mer oligos ordered from IDT, consisting of 24 A-T base pairs with G-C caps.

figure 3.1) to prevent fraying of the resultant double-stranded molecule, due to the high stability of the guanine-cytosine bond [6]. Each strand arrived as a lyophilized powder in a small cylindrical container, to which an $\sim$ 120 mM sodium salt buffer (described in section 3.2) was added to achieve an oligos concentration of 0.5 mg/mL of buffer. To aid in the dissolution of the oligos, the solution was alternately mixed vigorously using a mini analog vortex mixer (VWR-3000, VWR International, Mississauga, ON) and heated to over 60 ^{o}C (on the advice of IDT [82]) with a DNA thermal cycler (Perkin Elmer Cetus, Waltham, MA) in several one minute intervals, and also underwent a single $\sim$ 10 minute heating interval. The thermal cycler used was designed to fit glass test tubes, so it was necessary to manufacture a specialized metal attachment in-house that fit in the slots of the thermal cycler and had openings that fit the cylindrical containers, as well as 2 mL eppindorf vials, as shown in figure 3.2.

Once the two oligo strands had been satisfactorily dissolved in the buffer, 1 mL of the solution of each complementary strand was added to a 2 mL eppindorf vial. After vigorously mixing the resultant solution for approximately one minute with the vortex mixer, the vial was placed in the thermal cylcer and heated to a temperature greater than the melting point of the double-stranded DNA (65.9^{o}C [83]). To ensure full hybridization of the strands, the temperature of the solution was then reduced at a rate of approximately 1^{o}C per minute to a temperature well below the melting point ($\sim$ 40^{o}C) [40]. Further reduction to room temperature was allowed to occur

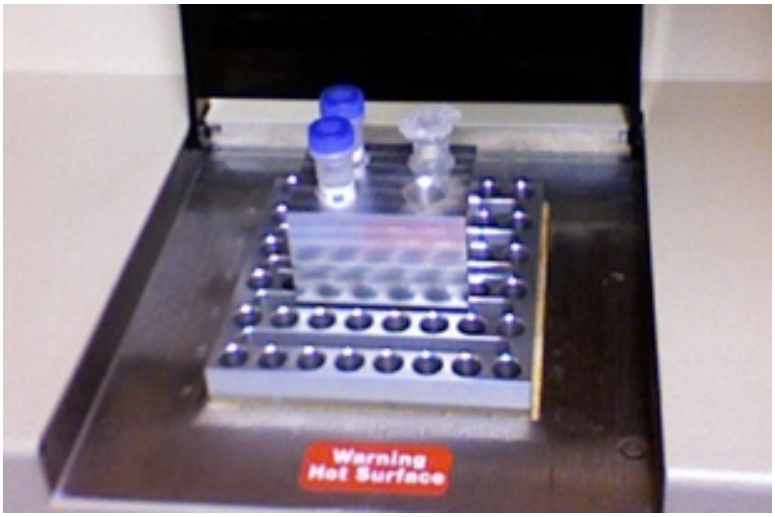

Figure 3.2: Custom metal attachment from DNA thermal cycler. It fits cylindrical DNA vials, and 2 mL eppindorf vials.

more rapidly. The hybridized oligonucleotide solution was then divided equally into ten 600 μL eppindorf vials with a pipette, resulting into $\sim$ 200 μL per vial. The ten samples were then stored in a 4^{o}C freezer.

Short Nucleotide Samples

Short, single strands of each of the four DNA bases were also ordered. The adenine and thymine strands were both six nucleotides long, while the guanine and cytosine strands were only five nucleotides long. Longer guanine strands were not used, as the nucleotides can easily interact with other members on the same strand, and form secondary structures [82]. While this is not a significant problem with cytosine strands, complementary strands of guanine and cytosine were desired.

High DNA concentration stock solutions of each strand were then produced by adding buffer to each powdered sample. The amount of buffer added depended on the production yield of each oligo. The adenine, guanine and cytosine stock solutions had a 1 mg/mL oligo concentration, while the thymine solution had a 1.5 mg/mL concentration. Because these were the first oligo samples ordered, the vortex mixer was not yet available, and the samples were dissolved in the buffer by vigorous shaking

by hand, as well as heating to over 60^{o}C for upwards of 10 minutes.

The stock solutions were then transferred to 600 μL eppindorf vials and all but one vial of each oligo were diluted with buffer to various concentrations. Solutions of all four sequences were obtained with oligo concentrations of 1 mg/mL, 0.5 mg/mL, and 0.25 mg/mL, as well as 1.5 mg/mL in the case of the thymine sequence. All solutions were stored in a 4^{o}C freezer prior to analysis [82].

3.1.2 CT-DNA

Fully hybridized calf-thymus DNA was obtained from Sigma Aldrich Canada, Ltd. (Oakville, Ontario). The manufacturers recommended only gentle mixing during dissolution, so after adding enough buffer to the CT-DNA powder to produce a 0.5 mg/mL DNA concentration, the solution was mixed with the vortex mixer at a very low setting. The DNA vial was secured to a special foam attachment of the vortex mixer (see figure 3.3), and was allowed to mix for about an hour. As recommended by Sigma-Aldrich, the vial was then immersed in an $\sim 37^o$C water bath and heated for approximately 20 minutes. The solution was then gently mixed with the vortex mixer for another hour, until the DNA was fully dissolved. With the use of a pipette, ten 600 μL eppindorf vials were each filled with approximately 200 μL of solution. Prior to analysis, the vials were able to be stored in a 4^{o}C freezer without risk of degradation [84].

3.2 Buffer

As will be discussed in section 4.2.1, several different buffers were produced throughout the course of this research. This section will only discuss the general buffer recipe, as all consisted of the same four salts. The recipe was based on that used in a previous study on the effects of UV radiation on DNA [40]. Each buffer consisted of sodium chloride (NaCl), sodium nitrate ($NaNO_3$), sodium phosphate dibasic (Na_2HPO_4) and ethylenediaminetetraacetic acid disodium salt (Na_2(EDTA)). These salts were added

Figure 3.3: Analog vortex mixer with special foam attachment for calf-thymus DNA vial.

to de-ionized water, each producing a desired molarity, and the resultant solution was heated to 30^{o}C and mixed vigorously with a hot plate/magnetic stirrer (Torrey Pines Scientific, San Marcos, CA) for 20-30 minutes. The buffer, with a pH of $\sim$ 7, was then stored in a 4^{o}C freezer until needed. Typically, before use, the buffer was mixed with the magnetic stirrer for approximately 10 minutes to ensure all of the salts were fully dissolved, even though no solid precipitate ever seemed to form.

3.3 DNA Irradiation

Throughout the course of this research, DNA samples were irradiated by both 6 MeV photons from a Varian 21EX linear accelerator (Varian Medical Systems, Inc., Palo Alto, CA, USA), and $\sim$1.25 MeV photons from a clinical Theratron 780-C Co-60 radiation therapy machine (MDS Nordion, Ottawa, ON). Samples of buffer were irradiated alongside the DNA in order to ensure that the spectral signature of the buffer was not affected by radiation. As the research progressed, different irradiation methods were adopted, and these will be discussed in sections 3.3.1 and 3.3.2.

3.3.1 Linear Accelerator

Linac Design

Linear accelerators produce x-rays through the bremsstrahlung interaction between an electron beam and a tungsten target. In a typical linac, as shown in figure 3.4, electrons are emitted from an "electron gun", and are accelerated through a waveguide by ∼3 GHz microwaves. After exiting the waveguide, the accelerated electron beam is then bent through 270^o by a "bending magnet", and is incident on a tungsten target. This target is thick enough to stop the electrons, and as a result, bremsstrahlung photons are produced [5]. At the high energies used in radiation therapy, the bremsstrahlung photons are forward peaked [5], and travel into the treatment head of the linac, as shown in figure 3.4. The photon beam is constrained by the metal *primary collimator*, which defines the initial geometry of the beam. As the beam passes through the *flattening filter*, which is typically made of tungsten, the lateral energy distribution of the photon beam is essentially "flattened", such that the photons in a plane perpendicular to the treatment head are of the same energy. The beam then passes through the *ion chamber*, where the dose rate of the beam can be sampled before it is further collimated by the *jaws* and the *MLCs*, seen in figure 3.4.

Experimental Method for Initial DNA Batches

The first batches of DNA samples were irradiated in a custom made acrylic phantom by a 6MV linac photon beam (British Columbia Cancer Agency - Vancouver Island Centre). The phantom, shown in figure 3.5, was made of three acrylic blocks, and fit ten 600 μL eppindorf vials in two rows of five vials each, displaced symmetrically about the centre of the phantom. The vials were positioned such that dose fluctuations were less than 2% along each row. Sitting on the treatment couch, the front face of the phantom was designed to be irradiated head on by a 20x15 cm^2 field with

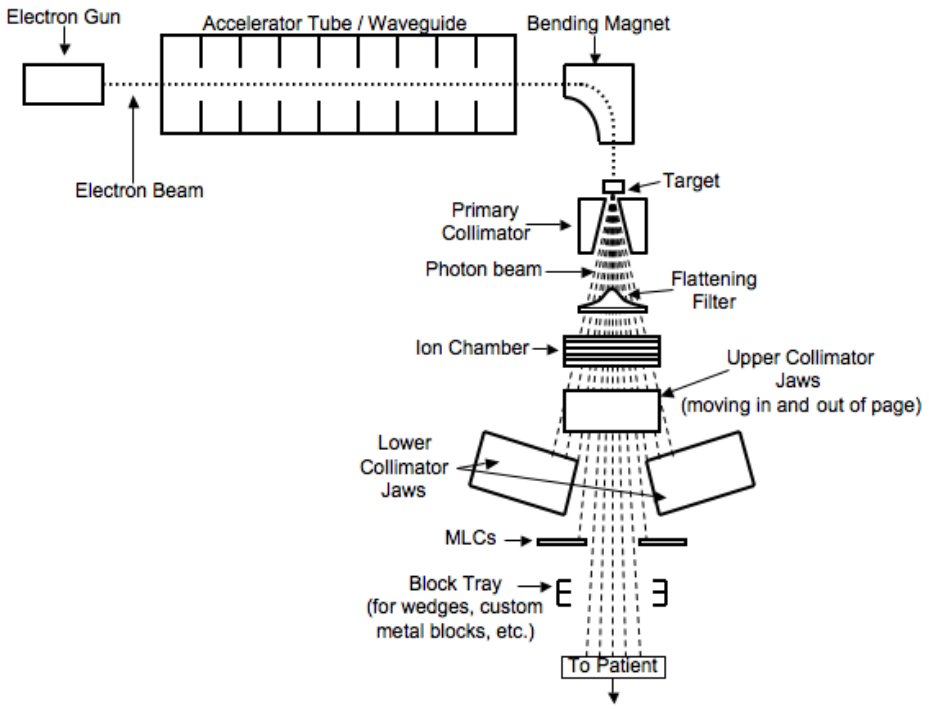

Figure 3.4: Schematic of waveguide and treatment head of a linear accelerator.

the linac treatment head at 90^o (see figure 3.5(d)). At a depth of 1.6 cm from the front face of the phantom, the vials were at the depth of maximum dose for the 6 MV beam. The phantom was aligned to the linac set-up lasers such that the distance from the DNA sample vials to the photon source was 100 cm.

After the initial setup, the vials were irradiated to successively higher doses between 0 and 100 Gy. After each dose interval, one of the DNA sample vials was removed. The vacant slot was filled with a vial of water, as any air gaps would disturb the dosimetry within the phantom.

Experimental Method for the Final Linac-Irradiated DNA Batches

After the analysis of the DNA samples irradiated using the previously described method, it was found that spectral differences between irradiated and unirradiated samples were undetectable in this dose range. This fact is discussed further in section 4.3 and led to the decision to irradiate samples to a single high dose. In order to

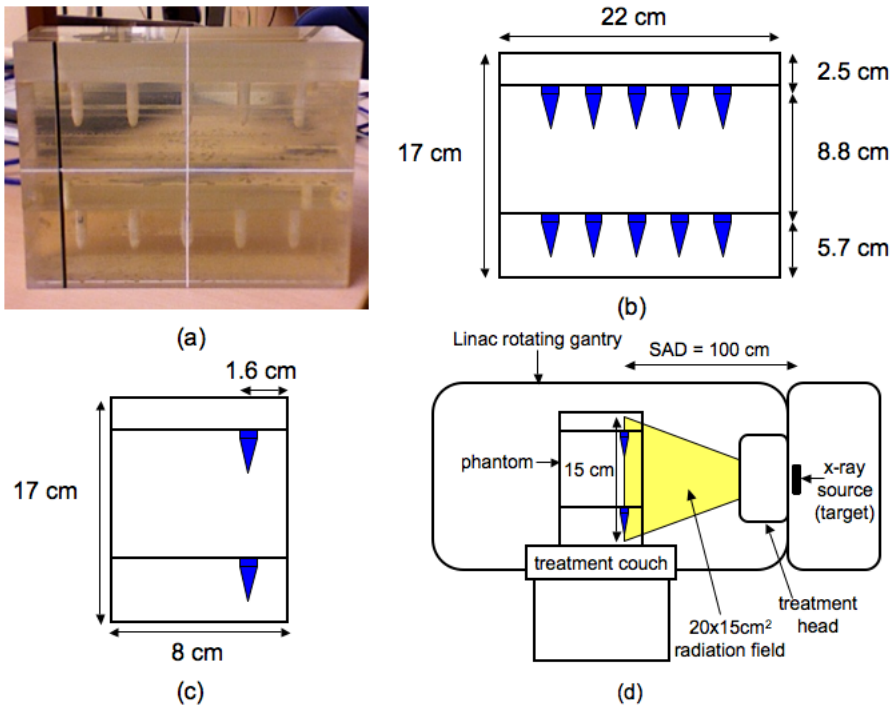

Figure 3.5: (a) DNA irradiation phantom used with linac. (b) Schematic of the phantom: Front view. (c) Side view. (d) Schematic of the setup for the low dose DNA irradiations using the linac.

achieve this goal, it was necessary to alter the initial irradiation setup. Figure 3.6(a) shows the modified setup, which involved placing the phantom, front face up, on the block tray of the linac, bringing it as close as possible to the x-ray source. In doing this, the source to sample distance was reduced to 58.6 cm, which increased the dose rate to the sample vials by a factor of $(100/58.6)^2$=2.91, due to the inverse square law of photon beam attenuation [5]. Due to the fact that field sizes are defined at the axis of rotation of the linac gantry, which is 100 cm from the source, it was necessary to change the field size at 100 cm from 20x15 cm^2 to 25 x 35 cm^2, as that resulted in a field size of 14.6 x 20.5 cm^2 at 58.6 cm from the source, which provided sufficient sample coverage (see figure 3.6(a)). Unfortunately, at 58.6 cm from the source, a treatment simulation showed that the dose to the sample vials would fluctuate by 5% or more, instead of the less than 2% fluctuation of the previous setup. However, this was not a significant problem, as the fact that all vials were irradiated to the

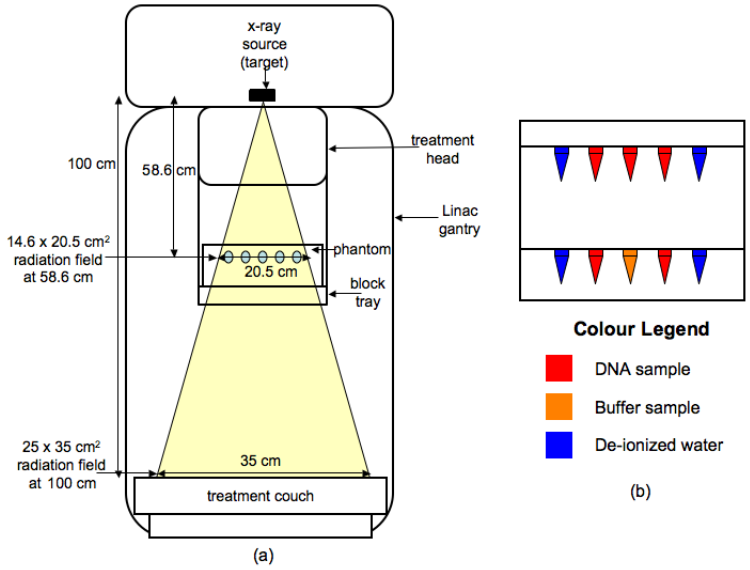

Figure 3.6: (a) Schematic of the setup for the high dose DNA irradiations using the linac. (b) Diagram of the sample distribution in the phantom for this setup.

same dose meant that the spectra of the individual vials could be averaged during data processing.

In this case, only five of the ten DNA samples were irradiated, as five were to be used to produce an average unirradiated sample spectrum. In order to reduce dose fluctuation throughout the samples, the DNA vials, and one buffer sample, were arranged in the phantom as shown in figure 3.6(b), with water-filled vials used to fill the empty slots. The samples were then irradiated to a dose of $\sim$ 300 Gy. As this is a dose much higher than that used for radiation therapy, it was not delivered all at once, but instead in a series of intervals separated in time so as not to put high stress on the linac. This resulted in lengthy irradiation times, which led to the decision to use a Co-60 treatment machine for further high dose irradiations.

3.3.2 Co-60 Treatment Machine

Unlike the linac, a Co-60 treatment machine has a very simple design. Figure 3.7 shows a typical Co-60 unit, like the Theratron 780-C used in this study. The source head contains a Co-60 source which can be moved by a sliding drawer in and out

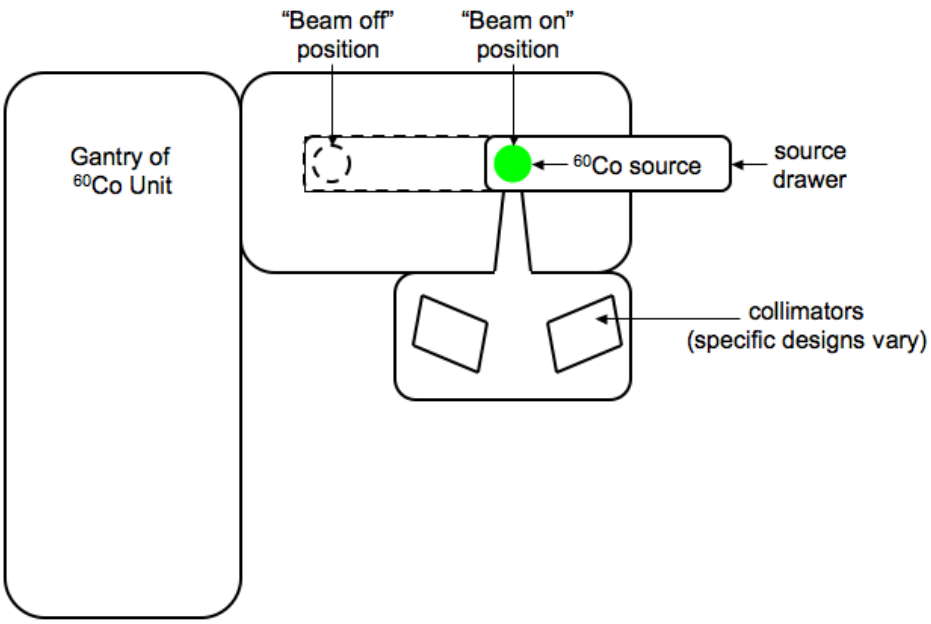

Figure 3.7: Schematic of a typical ^{60}Co unit with a source drawer.

of the collimator opening. When in the "beam off" position, the drawer is pushed completely into the source head where the radioisotope is heavily shielded. When fully extended out of the treatment head, the drawer is in the "beam on" position, and the 1.17 and 1.33 MeV photons emitted by the Co-60 source form the photon beam. Like the linac, the Co-60 unit has a primary collimator which defines the initial geometry of the beam, and secondary collimators to further define the dimensions of the rectangular field. Further collimation of the photon beam is provided by wedges and metal blocks that can be placed in the removable block tray of the Co-60 unit. Unlike the linac, a Co-60 treatment machine dose not have a flattening filter.

Experimental Method

The final batch of DNA samples were irradiated using a Theratron 780-C Co-60 radiation therapy machine (British Columbia Cancer Agency - Vancouver Centre). The setup was very similar to that of the high dose linac irradiations, with a couple of notable exceptions. Firstly, while the phantom was placed in the block tray, it was

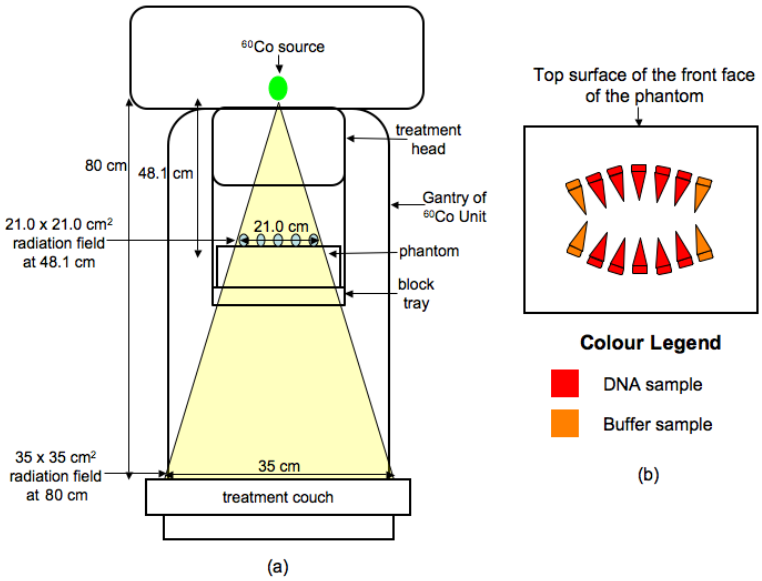

Figure 3.8: (a) Schematic of the setup for the high dose DNA irradiations using the ^{60}Co unit. (b) Diagram of the sample distribution in the phantom for this setup.

located more closely to the source, with it's front face only 48.1 cm from the source. To accommodate for this, a 35 x 35 cm^2 field was defined at 80 cm (the typical SAD for a Co-60 unit), resulting in a 21.0 x 21.0 cm^2 field at 48.1 cm (see figure 3.8(a)). The second difference from the setup of the high dose linac irradiations came from the fact that the depth of maximum dose for a Co-60 photon beam is 0.5 cm. If placed in the slots at a depth of 1.6 cm in the phantom, the sample vials would not be at d_{max} for a Co-60 beam, and the dose rate would not be at its maximum. As time restrictions did not allow the production of a modified phantom, the problem was addressed by securing the DNA and buffer vials to the surface of the front face of the phantom as shown in figure 3.8(b). Ultimately, a total dose of ~2000 Gy was delivered to the samples. As with the linac irradiations, the dose was delivered in a series of intervals.

3.4 Raman Spectroscopy

Analysis of the DNA and buffer samples was performed by Raman spectroscopy at a variety of different excitation wavelengths. Prior to analysis, and after spectral

acquisition for a given DNA batch, samples were stored in a 4^oC freezer. During analysis, both ultraviolet and visible light was used, and three different spectroscopic setups were utilized to achieve the desired wavelengths. Sections 3.4.1 and 3.4.2 describe the setup and experimental procedure used in each case.

3.4.1 Ultraviolet Resonance Raman Spectroscopy

The components of a fibre optic based ultraviolet resonance Raman spectrometer were discussed in detail in section 2.4. To summarize, as shown in figure 2.6, the setup consists of a frequency-doubled, continuous wave argon ion laser (Innova 90C, Coherent Inc., Santa Clara, CA) which is focused by a lens (labeled as the "optic coupler") onto a 600 μm fibre optic cable. The fibre leads to a probe tip (section 2.4.2), which is immersed into the sample and consists of a central fibre that acts as the source of the UV light, and six surrounding fibres that collect the scattered light. The six collection fibres lead the scattered light to a 0.750 m spectrograph (SpectraPro 2750, Acton Research Corp., Acton, MA), where the light is separated according to wavelength, and then incident on a CCD camera (Pixis 400, Princeton Instruments, Trenton, NJ) thermoelectrically cooled to -75^{o}C. In the camera, which is capable of achieving a spectral resolution of ~ 1 cm^{-1}, the light is converted to a digital signal and then passed to a personal computer where a spectrum is produced.

With this setup, the samples were analyzed in the same eppindorf vials in which they were irradiated, and were rotated by a small motor while the probe was immersed in the sample to prevent condensation of the dissolved DNA on the probe. In order to minimize the chances of this happening, the probe was removed from the sample whenever not acquiring data. Also, before each spectral acquisition, the probe tip was cleaned with ethanol, and then rinsed with deionized water, as any particulates on the probe tip can reduce the transmission of scattered light. After washing, the probe was gently dried with a kim wipe, and then laser light was allowed to pass through the tip for a minute or so to further dry the tip.

Throughout the spectral acquisition process, the laser power at the sample was carefully monitored, as it affected the signal strength of the system and needed to remain constant. Spectra of each batch of samples were acquired at incident UV wavelengths of 264, 257 and 248 nm, respectively, over the course of three days. For a given sample the spectral acquisition time varied depending on the incident UV wavelength, due to the variation in the laser power at the sample with wavelength. When using an excitation wavelength of 264 nm or 248 nm, three consecutive spectra of each sample were acquired for 30 seconds each (3x30s), while for an incident wavelength of 257 nm, three consecutive aquisitions of 10 seconds each (3x10s) were obtained. To reduce noise, all spectral acquisitions were obtained in the dark.

3.4.2 Non-Resonance Raman Spectroscopy

Ultimately, the final results of this research were obtained from the spectra acquired using incident UV light at wavelengths of 264, 257 and 248 nm. However, earlier studies considered spectra acquired with wavelengths of 785 nm and 632 nm. Unfortunately, these spectra did not prove as useful as those obtained using UV light, and this will be discussed further in section 4.3.2. Nonetheless, the procedure used for each set of acquisitions is described below, and both apparatus vary significantly from that of the UVRR spectroscopy.

Raman Spectroscopy at 785 nm

A schematic of the 785 nm Raman spectroscopic set-up is shown in figure 3.9. Essentially, it consists of a 785 nm high-power NIR laser (Renishaw plc, Gloucestershire, UK) which is incident on a 785 nm low pass filter that reflects all of the 785 nm light. The reflected light is then incident on a 10x objective lens which focuses the light onto the sample. Light that is Raman scattered off of the sample is then collected by the same objective, after which it is once more incident on the filter. As the filter transmits light at wavelengths longer than 785 nm, the light that has experienced

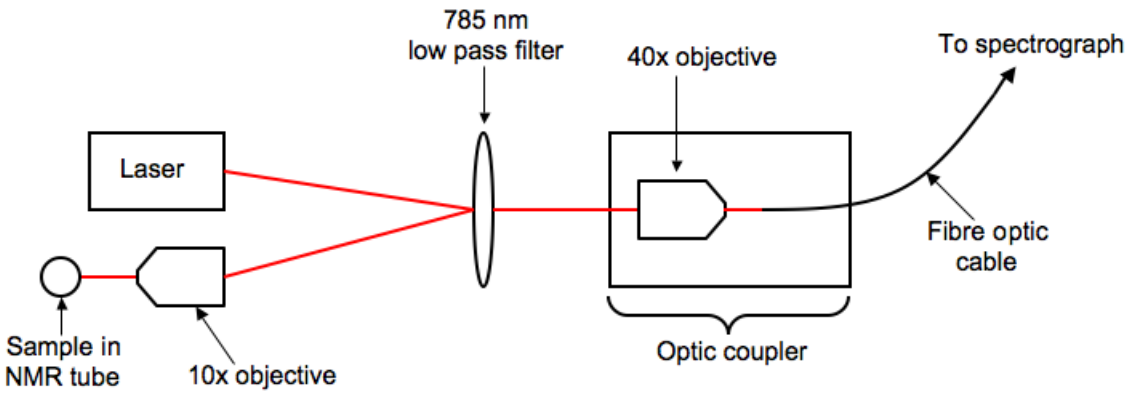

Figure 3.9: Schematic of the Raman spectroscopic setup using a 785 nm laser.

Stokes Raman scattering is allowed to transmit through the filter, and is then focused by a 40x objective onto a 100 μm fibre optic which is connected to the spectrograph. At this point, the set-up becomes the same as for the UVRR spectroscopy, and a spectrum is ultimately stored in the computer.

Using this apparatus, it was necessary to transfer the aqueous samples into glass NMR sample tubes, due to the significant Raman signal from the plastic eppindorf vials at 785 nm. When ready to acquire a spectrum, the laser was first allowed to warm up, producing an $\sim$ 300 mW beam, which was then focused onto the sample vial. The position of the sample was then varied such that the strongest spectral signal would be obtained. For a given sample, five spectra of three minutes each (5x3mins.) were acquired. As with the UVRR apparatus, spectra were acquired in darkness. Also, to minimize interference from the incident 785 nm light in the scattered signal, the optic coupler was shielded with aluminum foil, and the connection between the fibre optic and the spectrograph was covered.

Raman Microscopy at 632 nm

The spectroscopic apparatus that used a 632 nm laser was essentially a Raman microscope, as shown in figure 3.10. 632 nm light from a 50 mW He-Ne laser (Melles Griot, Carlsbad, CA) was directed into a microscope (BHSM model, Olympus, Markham,

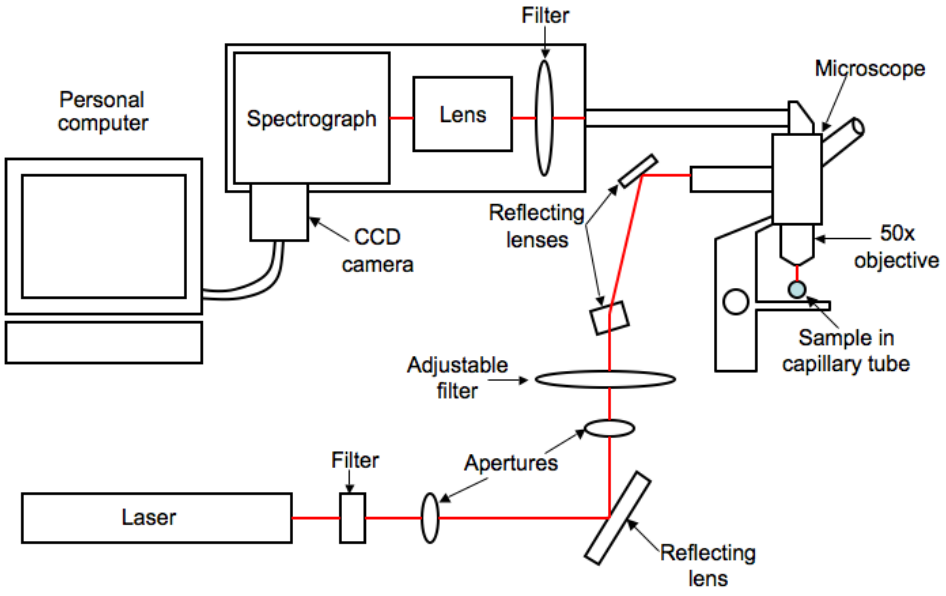

Figure 3.10: Schematic of the Raman microscope with a 632 nm laser excitation source.

ON) via a series of reflecting lenses and apertures, where it was focused onto the sample by a 50x objective. This same objective collected light that underwent 180^o Raman scattering, and directed it by mirrors onto a lens, which focused it into a spectrograph (Holospec f/1.4, Kaiser Optical Systems, Inc., Ann Arbor, MI), where it was directed onto a thermoelectrically cooled CCD detector (iDus DV-401-BV, Andor Technology, South Windsor, CT). From the CCD, the signal was sent digitally to a personal computer where a spectrum was obtained.

As with the 785 nm spectroscopic apparatus, the samples could not be analyzed in their eppindorf vials. Instead, a small amount of sample was transferred into a capillary tube, which was placed on the stage of the microscope. With the help of an internal light, it was possible to focus the microscope on the liquid in the centre of the capillary. To acquire a spectrum, the internal light, and all other ambient light, was shut off, and laser light was then allowed to strike the sample. A single three minute acquisition was performed for each sample (1x3mins.).

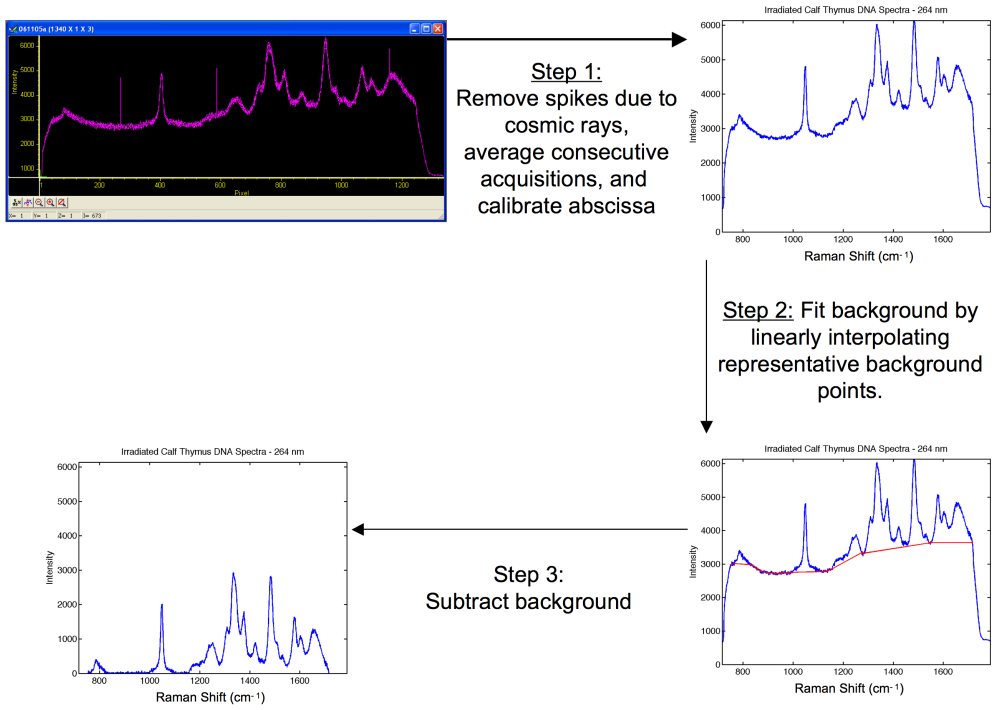

Figure 3.11: Flow chart of the primary data analysis process.

3.5 Data Processing

All data was grouped according to the DNA batch, and the incident wavelength used to acquire the spectra. Data processing was performed with Matllab (The Mathworks, Inc., Natick, MA), and the first step in the process involved the removal of any spikes in the spectra due to interference in the CCD from cosmic rays. The group of consecutive acquisitions obtained for each sample were visually inspected, and any points corresponding to spikes were removed. All consecutive acquisitions for a given sample acquired using a given incident wavelength were then averaged (see figure 3.11).

It was then necessary to calibrate the abscissa of the averaged spectrum, which initially correspond to the pixel values of the columns of the CCD detector (see section

2.4.4). This is done by using substances with well known Raman spectra, such as ethanol in the case of the UVRRS apparatus, tylenol for the 785 nm apparatus, and α-pinene for the 632 nm apparatus. The wavenumber shifts of the peaks of these substances are known, and so the wavenumber shift as a function of pixel position can be determined. This function is then applied to the spectra with the unknown Raman signature to convert the abscissa from pixel value to wavenumber shift (see figure 3.11).

The spectra were then further processed by removal of the spectral background. The background was unique to each spectrum, and was primarily due to Raman scatter from sources such as the sample container or the silica of the fibre optic, and any incident laser light that leaked into the spectrograph. Due to the high variation between spectra, it was determined, as will be discussed in section 4.3.1, that the optimal method for fitting the background of each spectrum involved the linear interpolation between manually selected points representative of the background (see figure 3.11).

After the background subtraction (see figure 3.11), the spectra were then normalized to the peak area of the $NaNO_3$ internal standard at 1049 cm^{-1}, so that the relative peak intensities of the spectra could be compared to one other. Several methods of determining the internal standard peak area were attempted throughout this study, as will be discussed in section 4.3.1, but ultimately, the area was determined by fitting the peak and the surrounding region with a combination of Lorentzian functions. Each spectra was divided by the calculated area of its internal standard peak.

Spectra acquired using a given incident wavelength could then be plotted on the same graph, and the spectral signatures of the irradiated and unirradiated samples could be compared. In some cases, due to slight drift of the grating of the spectrograph (see section 2.4.3), it was necessary to slightly shift the spectra so that their

internal standard peaks overlaid each other. This was acceptable, as the wavenumber shift of the internal standard peak should be consistent between spectra.

For the DNA and buffer samples irradiated to high doses, difference spectra were produced between the irradiated and unirradiated samples of each type. The spectra of all irradiated samples were averaged, as were those of the unirradiated samples. Any spectrum of a given irradiated or unirradiated sample that deviated significantly from the others of the same type was removed from the average. The averaged unirradiated spectrum was then subtracted from the averaged irradiated spectrum. To reduce the noise in the resultant difference spectrum, smoothing was performed using the two-point maximum entropy method [85, 86].

Chapter 4

Results and Discussion I: Initial Studies

This chapter presents results of the initial experiments that were performed, and explains how this work helped to influence and improve the experimental technique. Section 4.1 describes how analysis of the short, 5-6 base pair oligo samples led to the decision of DNA concentration that would be used for the remainder of the research (section 4.1.1), and how these samples provided basic information about the four DNA nucleotides (section 4.1.2). This is followed by a discussion on the evolution of the buffer recipe (section 4.2.1), and on how the final recipe was affected by ionizing-radiation (section 4.2.2). After a brief description of how the data processing techniques evolved throughout the research (section 4.3.1), the chapter concludes with the results of the non-resonance Raman spectroscopy (section 4.3.2) and of the UVRR spectroscopy of the DNA samples irradiated with the linear accelerator (section 4.3.3).

4.1 Preliminary Studies

By acquiring spectra of the short oligos each made up of repeating units of one of the four DNA bases, it was possible to obtain a spectral signature of each of the DNA nucleotides. While Raman spectra of the nucleotides have been acquired elsewhere [29, 33], the spectra obtained for this research were specific to the apparatus used. Spectral signatures of the nucleotides were only obtained using the UVRR

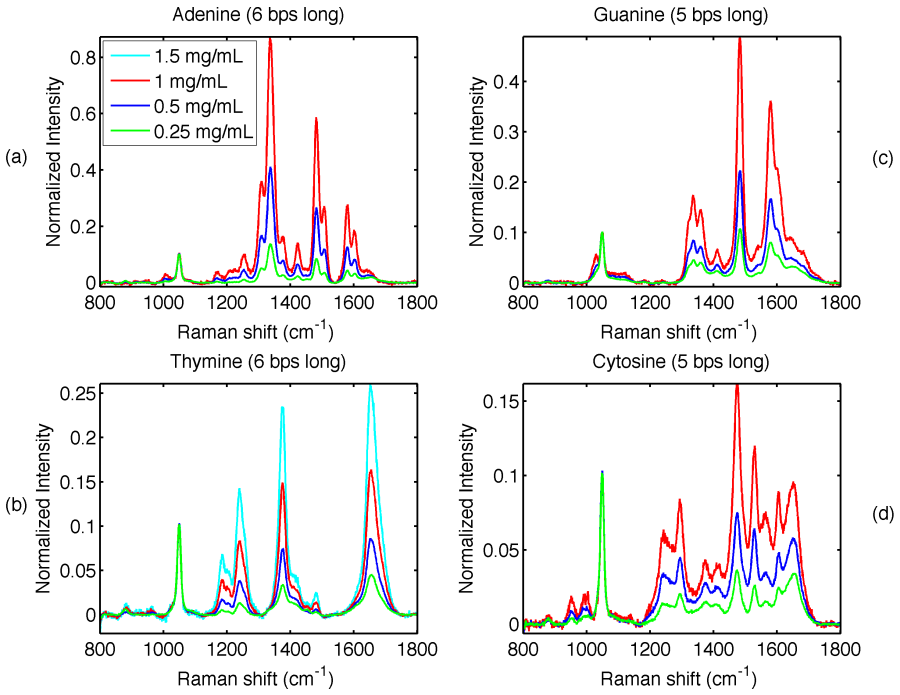

Figure 4.1: Spectra of the short oligo strands at various concentrations. (a) Adenine (b) Thymine (c) Guanine (d) Cytosine.

spectroscopic setup, and not those that utilized the 632 and 785 nm lasers, due to the poor Raman signal obtained at these wavelengths, as is discussed in section 4.3.

4.1.1 DNA Concentration

As these short oligos were the first analyzed in this research, their spectra were used to determine the optimal DNA concentration that would be used for all of the samples that followed. In order to determine how the Raman signal varied with DNA concentration, the short strands of each of the bases were diluted by varying amounts of buffer and analyzed accordingly. The adenine, guanine and cytosine strands were diluted to concentrations of 1.0 mg/mL, 0.5 mg/mL and 0.25 mg/mL, while thymine was diluted to all of these concentrations as well as 1.5 mg/mL. Figure 4.1 shows the spectra of each of the short strands at each of the concentrations, all normalized to the internal standard peak at 1049 cm^{-1}.

There were several factors to consider in choosing the concentration to be used for

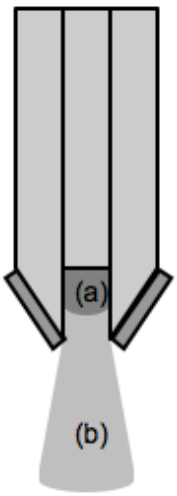

Figure 4.2: Representation of laser light exiting probe tip into a DNA solution. Shaded region (a) represents light penetrating a high concentration solution, while region (b) represents penetration in a low concentration solution.

the remainder of the research. For example, while high DNA concentrations would result in a significant amount of DNA Raman scatter, the absorption of the solution would increase and the scatter would come primarily from molecules close to the source, inadequately sampling the solution, and resulting in low SNR spectra (see figure 4.2). Also, if the concentration were too high, the chances of DNA adsorbing onto the probe tip would increase. It has also been found that the detection of ionizing radiation-induced spectral differences decreases with high concentration solutions [29]. However, for low concentrations, while the SNR of the spectrum improves, the Raman scatter from the DNA relative to that from the buffer reduces. This is why the DNA peaks in the normalized spectra of the low concentration samples in figure 4.1 have low intensities relative to the internal standard peak, despite having higher absolute intensity than the DNA peaks in the spectra of the high concentration samples.

Ultimately, a DNA concentration of 0.5 mg/mL was chosen, as it resulted in strong Raman scatter. It also was within the range of concentrations that had been analyzed succesfully in both UVRR [40] and FTIR [29] studies of radiation-induced

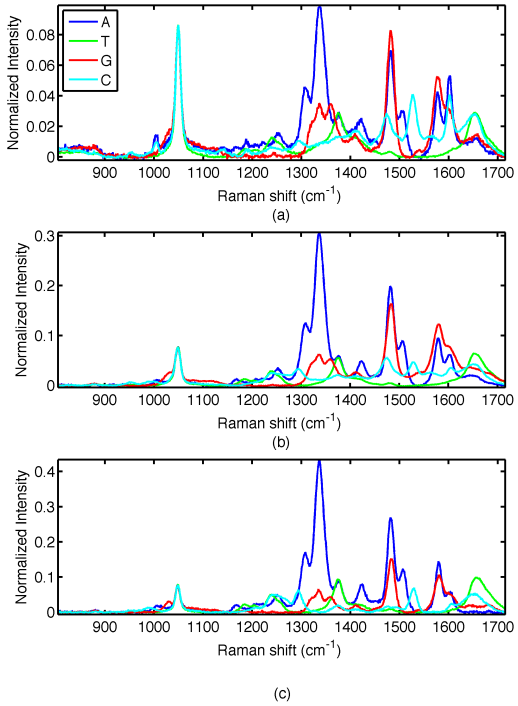

Figure 4.3: Spectral acquisitions of the four short oligo strands at incident UV wavelengths of (a) 248 nm (b) 257 nm (c) 264 nm.

damage to DNA.

4.1.2 UVRR Spectral Signatures

After having chosen an appropriate DNA concentration, spectra of each of the 0.5 mg/mL adenine, thymine, guanine and cytosine solutions were acquired using each of the three incident UV wavelengths. These spectra are displayed in figures 4.3 (a)-(c), and all are normalized to the internal standard peak at a wavenumber of 1049 cm^{-1}. Due to the fact that each short oligo strand is composed of only one base each, it is assumed that the spectrum of a given strand is essentially representative of the spectral signature of its component base.

The molecular vibrations that correspond to the peaks in the spectra of each of the bases are defined in table 5.1. Knowing that a Raman spectrum is defined by vibrations such as these, the fact that adenine and guanine have the most intense

Raman peaks in the spectra of figures 4.3(a)-(c) is not surprising. This is due to fact that each of the incident UV wavelengths used have frequencies that are close to resonance with the vibrations of these bases [37] (see section 2.2.2). As these frequencies are not as close to being in resonance with the vibrations of thymine and cytosine, the spectra of these bases are naturally less intense. However, despite the intensity differences, upon close inspection, it can be seen that changing the incident UV wavelength (and thus the frequency) has a significant effect on the spectral signature of each base.

For example, the peaks of the cytosine spectrum are most intense when acquired using 248 nm light, and they get progressively weaker using incident wavelengths of 257 and 264 nm. The guanine spectrum also seems to weaken when changing from an incident wavelength of 248 nm to 264 nm, particularly in the case of the peaks at 1476 and 1576 cm^{-1}. In contrast, the very same peaks in the adenine spectrum become more pronounced as the incident UV wavelength increases, while the adenine peak at 1604 cm^{-1} is the one to decrease. At first, it may seem strange that some of the adenine peaks decrease, while others increase, but it must be remembered that the molecules within a given base do not all vibrate at the same frequency, and thus respond to the excitation light differently.

By understanding changes such as these, it is possible to selectively enhance particular peaks of a spectrum by changing the incident UV wavelength. A peak that is weak in a spectrum acquired at one incident wavelength is often stronger when the spectrum is acquired at another. This type of selective analysis is particularly useful when considering spectra of more complicated DNA sequences, which are essentially some combination of the four base spectra. Through varying the incident UV wavelength used, it is possible to enhance the contribution of a particular moiety of the DNA molecule to the overall spectrum.

In this research, the effects of ionizing radiation on DNA were studied, and

radiation-induced spectral differences were analyzed in spectra acquired at each of the three incident UV wavelengths (see Chapter 5). Depending on the incident UV wavelength used, radiation-induced changes to a particular moiety were either more or less obvious. In analyzing the spectra of a sample acquired using all three wavelengths, a more complete picture of the radiation-induced effects was obtained.

4.2 Buffer

4.2.1 Recipe

The initial recipe for the phosphate buffer used in this research was adopted from previous work involving the study of oligonucleotides with UVRRS [40]. This buffer contained a 951.06 mM concentration of NaCl, a 50 mM concentration of $NaNO_3$, a 10.02 mM concentration of Na_2HPO_4, and a 1.02 mM concentration of Na_2(EDTA). The $NaNO_3$ was the internal standard of the buffer as it has a well defined Raman peak, the Na_2HPO_4 was used to keep the pH $\sim$ 7, the Na_2(EDTA) was a preservative, and the NaCl was used to increase the sodium ion concentration.

After realizing the subtlety of the spectral differences between the irradiated and unirradiated oligonucleotide spectra in this research, the increased stability of the DNA molecules allowed by the high sodium ion concentration [87, 88] of the buffer, whose spectrum is shown in figure 4.4(a), became a concern. Following a brief survey of the sodium concentrations of buffers used in other research [36, 39, 40, 89–96], it was determined that a more typical buffer had an overall sodium ion concentration on the order of 100 mM, which is a physiological salt concentration [91]. As a result, the $\sim$ 1000 mM [Na^+] buffer that was currently being used was diluted with de-ionized water to a total sodium ion concentration of $\sim$ 100 mM. The UVRR spectrum of this buffer is shown in figure 4.4(b), but, as can be seen from the figure, in the process of diluting the buffer, the intensity of the internal standard peak at 1049 cm^{-1} had been significantly reduced. This resulted in data processing problems, as an intense,

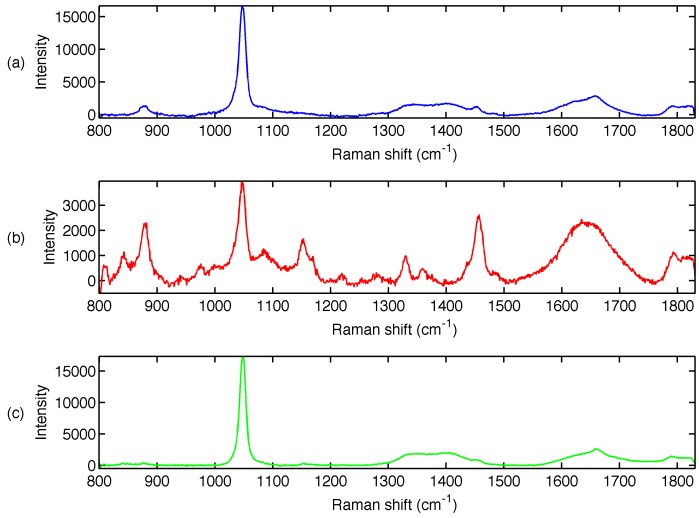

Figure 4.4: Spectra of the various buffer recipes acquired @ 257 nm (a) $\sim$ 1000 mM [Na^+] buffer (b) $\sim$ 100 mM [Na^+] diluted buffer (c) Final $\sim$ 100 mM [Na^+] buffer

well-defined peak is necessary for accurate normalization.

In order to address this problem, the individual components of the buffer were investigated, and the UVRR spectrum of 50mM solutions of each was acquired (see figure 4.5). From these spectra, it was obvious that the primary contributor to the intense peak at 1049 cm^{-1} was sodium nitrate, and thus it's concentration should not be diluted in the buffer. Knowing this, a new buffer was produced, and it's spectrum is shown in figure 4.4(c). Only the overly high concentration of NaCl was reduced in this new recipe, to a value of 50 mM, leaving a strong normalization peak at 1049 cm^{-1}, and bringing the buffer to a physiological salt concentration. All DNA samples used in the final experiments of this research, from which the conclusions were drawn, were diluted with this buffer.

Ultimately, the effect of the different buffers on the magnitude of the radiation-induced changes in the DNA spectra requires further study, as the samples diluted with the final buffer were irradiated to much higher doses than those diluted with the initial buffers. To truly quantify the differences caused by buffer sodium concentration

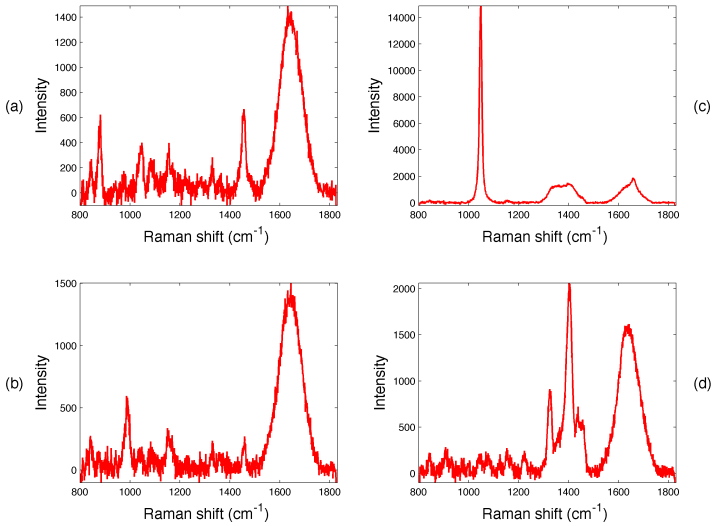

Figure 4.5: Spectra of the component salts of the buffer acquired @ 257 nm (a) NaCl (b) $NaNO_3$ (c) Na_2HPO_4 (d) Na_2(EDTA)

alone, it would be necessary to irradiate the DNA solutions composed of the various buffers to the same dose.

4.2.2 Radiation-Induced Effects on the Buffer

After having decided upon the appropriate buffer recipe, it was important to determine whether or not the spectrum of the buffer exhibited any radiation-induced changes. Ideally, the irradiated and unirradiated buffer spectra should be identical. In order to understand the buffer's response, if any, to radiation, the buffer samples that were irradiated alongside the DNA samples to a high dose with the Co-60 treatment unit were analyzed.

Figures 4.6(a)-(c) show the spectra of the irradiated and unirradiated buffer samples, acquired at each of the incident UV wavelengths, and figures 4.6(d)-(f) show their corresponding difference spectra. The spectra are normalized to the peak at 1049 cm^{-1}, and the spectral differences between the irradiated and unirradiated buffer spectra acquired using 264 and 248 nm light (figures 4.6(d) and (f)) are minimal. Fluctuations in the difference spectra corresponding to these wavelengths are less

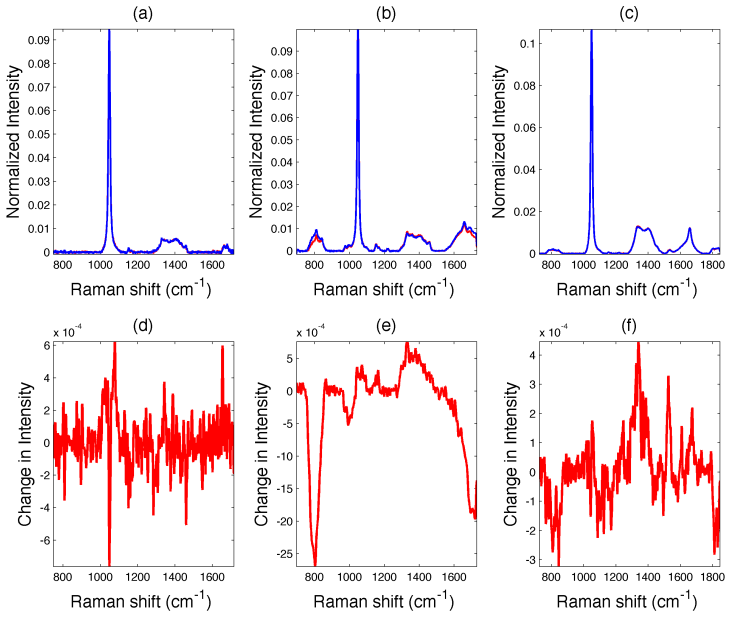

Figure 4.6: Normalized spectra of the irradiated (red) and unirradiated (blue) buffer samples and their corresponding difference spectra. (a) Buffer spectra @ 264 nm (b) Buffer spectra @ 257 nm data (c) Buffer spectra @ 248 nm data (d) Difference spectrum @ 264 nm (e) Difference spectrum @ 257 nm (f) Difference spectrum @ 248 nm.

than 1% of the peak intensity at 1049 cm^{-1}, and can be attributed to spectral noise. More significant fluctuations are found between the irradiated and unirradiated spectra acquired using 257 nm light (figure 4.6(e)). While the fluctuations in the difference spectrum of the 257 nm data are primarily in the 1% range, there are some larger intensity differences around 800 cm^{-1} and 1700 cm^{-1}. The fact that these fluctuations are not visible in the spectra acquired using 264 nm and 248 nm light suggests that these differences may be due to poor technique in acquiring the 257 nm data. On the other hand, the peaks around 800 cm^{-1} and 1700 cm^{-1} are at their most intense in the spectra acquired using 257 nm light, while they are much less significant in the spectra acquired at the other wavelengths. It may be that the radiation-induced changes in these peaks are only visible when probing the sample with 257 nm light, however, this is unlikely as the buffer salts are not near resonance at 257 nm, and thus are not expected to provide information that is not visible at the other wavelengths.

Regardless, these fluctuations occur in spectral regions where there are either no DNA Raman peaks, or only very weak ones, and thus will have minimal impact on the peaks of the DNA spectra. Furthermore, the regions around 800 cm^{-1} and 1700 cm^{-1} are near the edges of the spectral window, where the signal is typically less reliable. However, as these fluctuations in the buffer spectrum cannot be definitively labeled as processing artifacts (although this seems likely), they must be taken into consideration when analyzing the DNA spectra acquired using 257 nm light.

4.3 DNA Spectral Analysis: Initial Studies

4.3.1 Data Processing

Two of the most important aspects of the spectral processing involved subtracting the background, and normalization of the spectrum to the internal standard peak. As was mentioned in section 3.5, a manually selected baseline was ultimately subtracted from each spectrum, and normalization was performed using the area of the peak at 1049 cm^{-1}, calculated using a combination of fitted Lorentzian peaks. Initially, however, the techniques differed significantly, and a brief discussion of these early methods is given below.

Background Subtraction

In the first attempt at background subtraction, a polynomial function was fit to the baseline and subtracted from the spectrum. The data points used in the fit were those in user defined regions identified as being due primarily to the baseline. The order of the fit varied depending on the data set, but it involved a degree of trial and error, and the final choice was somewhat subjective. For a given set of spectral acquisitions of the same type of sample, the order of the polynomial remained constant and data from the same wavenumber regions was used in its calculation. Unfortunately, due to variations in spectral noise and baseline within a given set of acquisitions, the goodness of the polynomial fit was not very consistent. In some cases, the fit could be

improved by uniquely identifying the baseline polynomial order for each spectrum, as well as the data ranges used in the fit. However, due to the large number of peaks in each spectrum, the number of data points representative of the baseline were small, which significantly affected the accuracy of the fit. In the end manually selecting points representative of the background and linearly interpolating between them allowed for a more consistently accurate approximation of the baseline, with less dependance on the number of data points used in the fit.

Normalization

Unlike the background subtraction, variations in the normalization technique had only a minimal affect on the data. In all cases, spectra were normalized to the internal standard peak at 1049 cm^{-1}, and only the area calculation of the peak varied. Initially, a very rough area calculation was performed which involved summing the intensity of the spectrum at each point in a wavenumber range symmetric about the centre of the peak at 1049 cm^{-1}. In order to determine whether small variations in the width of the range affected the normalized data, spectra from a given data set were normalized using both a window that encompassed the entire peak, and one that only contained its central region. Difference spectra between the irradiated and unirradiated samples normalized using each window size were then calculated. The appearance of radiation-induced spectral differences was not found to vary with window size, and their intensity in each difference spectrum was only affected by a uniform scaling factor. However, the small window size was still favoured, as it reduced the influence of overlapping peaks on the normalization.

Eventually it was determined that a more rigorous way to differentiate between the internal standard peak and those that surround it was to fit the region with a series of Lorentzians. The area of the fitted internal standard peak was then used to normalize the spectrum. While this method proved to give equivalent results to the more simple methods described earlier, it was chosen over the others due to its more

accurate area calculation.

One final consideration of the normalization technique involved spectra that were to be averaged, as in the case of the high dose irradiations in which the spectra of all irradiated samples were averaged, as were those of all unirradiated spectra. In this situation, the spectra could be normalized before averaging, or the final result could be normalized. It was determined that neither method significantly affected the difference spectra between the irradiated and unirradiated samples, but it was decided that normalization would be performed on the averaged result, as it had a higher SNR than the individual spectra.

4.3.2 Non-Resonance Raman Spectroscopy

Examples of the unirradiated spectra of CT and SS-DNA acquired at both 632 nm and 785 nm are shown in figure 4.7. Unfortunately, upon analysis, it was found that these spectra contained no useful information about the DNA samples, due to the low concentration of the DNA solution. As non-resonance Raman scattering is already very weak, the scattered light was not intense enough to register in the CCD. As a result, the CT and SS-DNA spectra are virtually identical at each incident wavelength, and the peaks that are visible in the spectra of figure 4.7 are due primarily to ethanol, which was accidentally introduced into the DNA solution during transfer to the NMR tubes used for the 785 nm spectroscopic setup. A spectrum of ethanol acquired at 257 nm is shown in figure 4.8 to illustrate the similarities. This spectrum is essentially identical to those in figure 4.7, apart from some peaks in the 1350 - 1500 cm^{-1} region of the spectrum acquired at 785 nm (see figure 4.7(a) and (c)). However, it is not clear that these peaks are due to DNA Raman scatter, as they are poorly resolved and there is a high degree of noise in the spectrum acquired at 785 nm due to Raman scatter from both the glass NMR tubes containing the samples and the silica of the fibre optics. Even if these peaks were due to DNA, they would only provide minimal information, and it was decided that non-resonance Raman spectroscopy

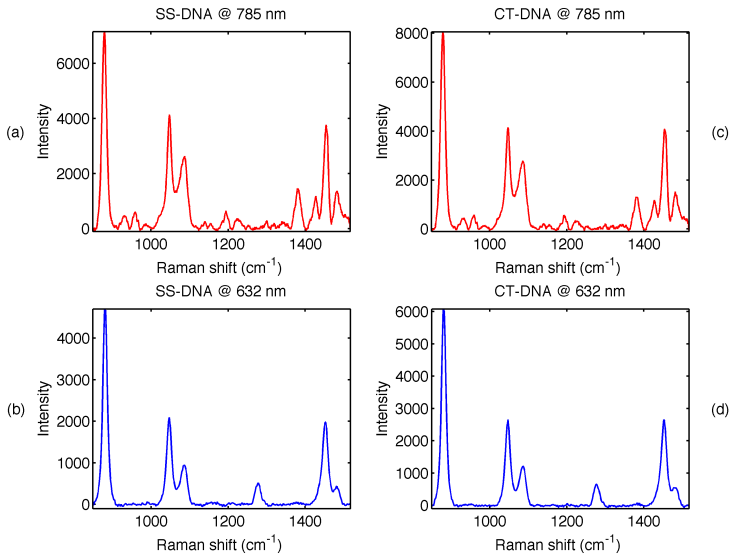

Figure 4.7: Unirradiated spectra of (a) SS-DNA @ 785 nm (b) SS-DNA @ 632 nm (c) CT-DNA @ 785 nm (d) CT-DNA @ 632 nm

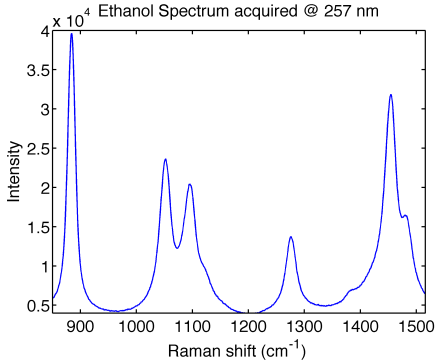

Figure 4.8: Raman spectrum of Ethanol acquired with an incident wavelength of 257 nm.

would not be pursued any further in this research, in favour of the more fruitful resonance Raman spectra. Due to this decision, and the ethanol contamination of the samples, the non-resonance Raman spectra of the irradiated SS and CT-DNA samples are not presented.

4.3.3 Resonance Raman of Low-Dose DNA Samples

Unlike the spectra acquired at 785 and 632 nm, the strong resonance Raman scattering produced by UV light compensated for the low DNA concentration of the samples, and resulted in intense DNA peaks in the UVRR spectra. Figure 4.9(a) shows the

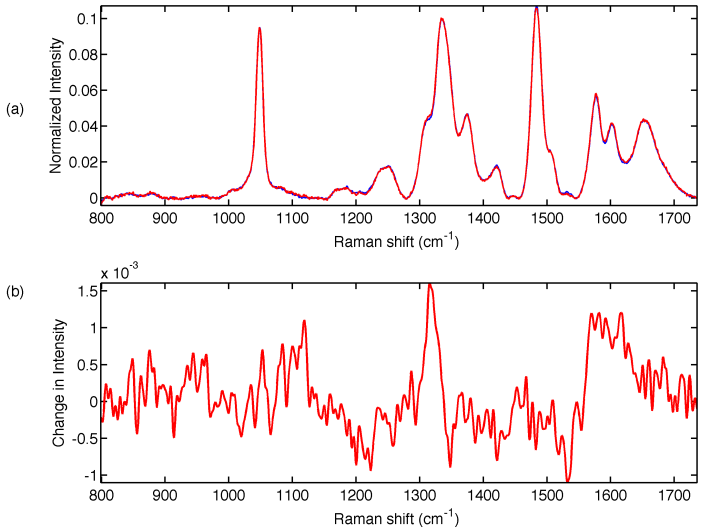

Figure 4.9: (a) Raman spectrum of SS-DNA irradiated to $\sim$ 300 Gy (red) and unirradiated (blue). Spectra acquired with an incident wavelength of 257 nm. (b) Difference spectrum between spectra of irradiated and unirradiated SS-DNA.

spectra of SS-DNA irradiated to $\sim$ 300 Gy with the linac and unirradiated SS-DNA, acquired at an incident UV wavelength of 257 nm. In these spectra, the peaks seen correspond to the DNA Raman peaks expected to appear in this wavenumber region, as listed in Table 5.1. However, only minor spectral features are visible in the difference spectrum between the irradiated and unirradiated samples shown in figure 4.9(b). The situation is similar for the other samples irradiated with the linac to both lower doses (between 0 and 100 Gy) and higher doses ($\sim$ 450 Gy). As a result, the spectra of these samples are not shown here.

While it is possible that some of the variation in the difference spectra of these samples, such as that in figure 4.9(b), is due to radiation-induced effects to the DNA, the small magnitude of the differences led to the decision that these spectra would not be analyzed. Instead, that would be left for the spectra of the SS and CT-DNA samples irradiated to $\sim$ 2000 Gy with the Co-60 treatment unit, in the hopes that any radiation-induced spectral changes would be more obvious. This analysis is described in Chapter 5.

Chapter 5

Results and Discussion II: Effects of Ionizing Radiation on DNA

This chapter presents a detailed discussion on the ionizing radiation-induced effects of SS-DNA and CT-DNA. Section 5.1 describes difference spectra between the irradiated and unirradiated spectra of SS and CT-DNA in detail, offering interpretations of the radiation-induced spectral differences with reference to table 5.1, and using the numbering convention shown in figure 1.1 for the molecules of the bases. A general discussion of the results and the utility of UVRRS in the study of ionizing radiation-induced damage to DNA follows in section 5.2.

The irradiated and unirradiated spectra of the CT-DNA acquired at an incident UV wavelength of 264 nm are shown as an example in figure 5.1(a), with the difference spectrum between the two shown in figure 5.1(b). The signal-to-noise ratio (SNR) of the difference spectrum in figure 5.1(b), at ~ 25, is a significant improvement over that of the difference spectrum corresponding to the DNA irradiated with the linac (figure 4.9(b)), which was ~ 8. This SNR improvement is also true of the rest of the data corresponding to the samples irradiated to ~ 2000 Gy, which is summarized in figure 5.2. The average spectra of the unirradiated CT and SS-DNA samples acquired at each of the three incident UV wavelengths are shown in figures 5.2(a)

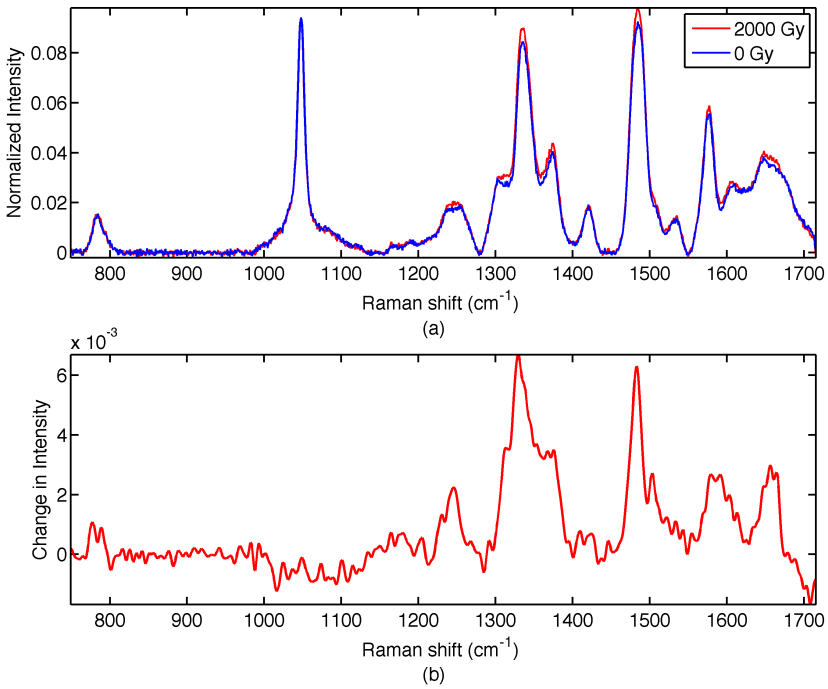

Figure 5.1: (a) Irradiated and unirradiated CT-DNA spectra acquired at 264 nm. (b) Difference spectrum between the irradiated and unirradiated CT-DNA spectra.

and (e) respectively, with the difference spectra between each set of the irradiated and unirradiated samples shown in figures 5.2(b)-(d) for the CT-DNA and figures 5.2(f)-(h) for the SS-DNA.

The spectral changes for each difference spectrum are summarized in table 5.1, along with information regarding the assignment of the peaks to scatter from particular molecular groups. As each peak contains a contribution due to scatter from each of the DNA bases, the primary and secondary bases represented by each peak are also summarized in table 5.1. The relative contribution of each of the bases to the peaks is determined based on the relative intensities of the peaks in the spectra representative of the individual bases in figure 4.3. The intensity of the scatter from the primary and secondary contributors to each peak is also classified (from very weak to very strong), again based on the spectra in figure 4.3.

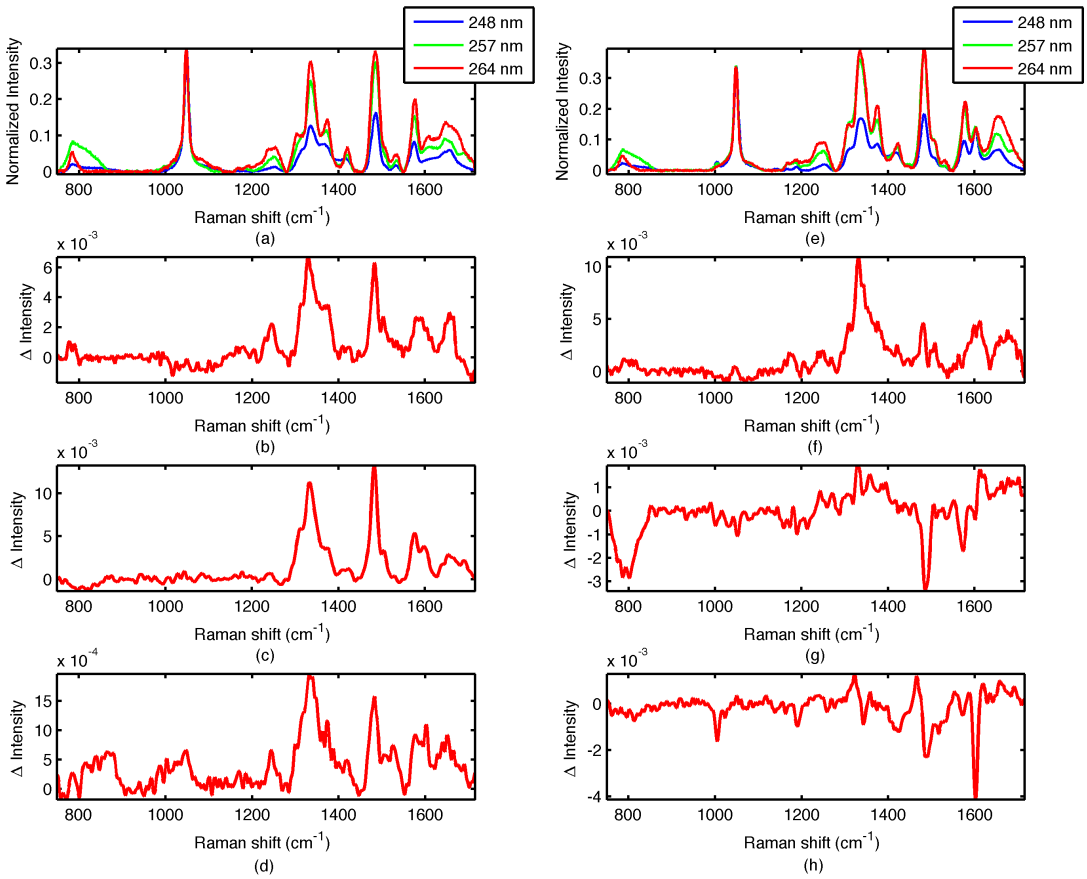

Figure 5.2: a) Unirradiated calf-thymus DNA spectra b) 264 nm difference spectrum between irradiated and unirradiated CT-DNA c) 257 nm difference spectrum d) 248 nm difference spectrum e) Unirradiated short stranded DNA spectra f) 264 nm difference spectrum between irradiated and unirradiated SS-DNA g) 257 nm difference spectrum h) 248 nm difference spectrum

Table 5.1: Summary of the Effects of Radiation on Spectra of 30-mer & Calf Thymus DNA acquired using 248, 257 and 264 nm light

ν (cm^{-1})	248 nm		Effect		257 nm		Effect		264 nm		Effect	
	Prim./ Moiety	**Sec./ Moiety**	**CT**	**SS**	**Prim.**	**Sec./ Moiety**	**CT**	**SS**	**Prim.**	**Sec.**	**CT**	**SS**
785	**C(w)** Ring breathing [a]	**T(vw)** Ring breating **Backbone** O-P-O s [c]		↓	**C(w)**	**T(vw)/ Backbone**	↓	↓	**C(w)**	**T(vw)/ Backbone**		
835	**Backbone** O-P-O s, marker of B-DNA [a]			↓	**Backbone**		↓	↓	**Backbone**			
1005	**A(w)**	**C(w)**		↓	**A(w)**	**C(vw)**						
1168	**A(w)** N7=C8, N1-C2s; C6-NHb				**A(w)**				**A(w)**			↑
1185	**A(w)**	**T(vw)** C5-CH3 s **C(vw)**		↓	**T(w)**	**A(vw)**			**T(w)**	**A(vw)**		
1208	**A(w)** C8-H, N7=C8 s	**T(vw)**			**A(w)**	**T(w)**			**A(w)**	**T(w)**		
1240	**T(mw)** C5-CH3s; ring s	**C(vw)**			**T(mw)**	**C(mw)**			**T(mw)**	**C(mw)**	↑	
1252	**A(mw)** N1-C2, C8-N9 s, C2-H b; N1=C6, C6-N [b]	**T(w)**			**A(mw)**	**C(w)** C6-H b, C4-N s			**A(mw)**	**C(mw)**	↑	
1310	**A(m)** C8-N9, C2=N3 s; C8-H b		↑	↑	**A(m)**		↑	↑	**A(m)**		↑	↑
1335	**A(s)** C5-N7, N7=C8 s	**G(m)**	↑		**A(s)**		↑	↑	**A(s)**		↑	↑
1375[1]	**G(m)** N7=C8, N1-C6, C5-N7 s	**A(m)** **T(m)** C6-Hb; ring s	↑		**A/T(m)**	**G(m)**	↑		**A/T(m)**	**G(w)**	↑	↑
1421	**A(m)** N1=C6, C6-N s	**C(mw)** **G(mw)** C4-N9, C5-N7 s **T(mw)** ring s		↓	**A(m)**		↑		**A(m)**			↑
1486	**G(s)** C8-H b; C8-N9, N7=C8s	**A(s)** N9-C8s; C2-H, C8-H b [b]	↑	↓	**A(s)**	**G(s)**	↑	↓	**A(s)**	**G(m)**	↑	
1507	**A(mw)** N-acceptor site, prob. N1 &/or N3 & N7 [c]	**C(vw)**		↓	**A(mw)**		↑		**A(mw)**		↑	↑

Continued on Next Page...

ν (cm^{-1})	248 nm		Effect		257 nm		Effect		264 nm		Effect	
	Prim./ Moiety	**Sec./ Moiety**	**CT**	**SS**	**Prim.**	**Sec./ Moiety**	**CT**	**SS**	**Prim.**	**Sec.**	**CT**	**SS**
1530	**C(mw)** N3=C4, N1-C2 s		↑	↓	**C(mw)**	**G(vw)** C4-N9, C6=O, N1-C2 s			**C(mw)**			
1576	**G(m)** N3-C4, C4=C5, C5-N7s, base stack.[2]	**A(m)** C4=C5, N3-C4 s; N-H2 def. [c]			**G(ms)**	**A(m)**	↑		**A(m)**	**G(m)**	↑	
1604[1]	**A(m)** N-H2 b; C5-C6, C6-N s	**C(m)** N-H2 b, C4-N s **G(m)** N1-H b, N1-C2 s	↑←	↓	**G(ms)**	**A(m)**	↑←		**A(m)**	**G(m)**	↑←	↑
1650	**C(m)** C2=O, C2-N3 s		↑		**C(mw)**	**G(mw)** C=O s	↑		**C(mw)**		↑	
1673	**T(m)** C4=O, C5=C6 s, C2=O [c]	**G(mw)** C=O s **A(mw)**	↑	↑	**T(m)**		↑		**T(m)**		↑	
1690	**T** C4=O s [b]; C2=O s [c]	**C** C=O s			**T(mw)** C4=O s, C2=O s	**G(mw)** C6=O, C5-C6 s, N1-H b	↑	↑	**T(mw)**	**G/C(w)**		

↑, Intensity increase; ↓, Intensity decrease; ←, wavenumber downshift; →, wavenumber upshift
A, adenine; **T**, thymine; **G**, guanine; **C**, cytosine; s, stretch; b, bend; def., deformation
(s), strong intensity; **(m)**, medium; **(mw)**, medium weak; **(w)**, weak; **(vw)**, very weak
[1]Peak centre shifts slightly with incident UV wavelength
[2]Vibration is sensitive to base stacking
Note: All peak assignments obtained from reference [33] *except*:
[a]from reference [29]
[b]from reference [36]
[c]from reference [91]

5.1 Effects of Ionizing Radiation on a 30-mer Oligonucleotide and Calf-Thymus DNA

From observing the difference spectra of the CT-DNA (figure 5.2(b)-(d)) and SS-DNA (5.2(f)-(h)) calculated from spectra acquired at each of the incident UV wavelengths, it is clear that there are pronounced spectral differences between the irradiated and unirradiated samples. These differences are particularly significant in the CT-DNA difference spectra, but are also readily observed in the SS-DNA data. Keeping in

mind possible changes induced in the buffer by the radiation (see section 4.2.2), an interpretation of the difference spectra in figure 5.2 is given below. The discussion is separated into wavenumber regions corresponding to closely grouped spectral peaks.

5.1.1 1550 - 1700 cm^{-1}

CT-DNA: From figure 5.2(b)-(d) it can be seen that there are several moderate intensity fluctuations in this region. In the 264 and 254 nm difference spectra, an intensity increase is visible in the peak at 1576 cm^{-1} (figure 5.3(a)). This peak corresponds to the C4=C5 stretching vibrations on both the adenine and guanine rings [33], which are involved in base stacking (table 5.1 and figures 5.3(c) and (d)). The intensity increase of the peak at 1576 cm^{-1} suggests an increase in Raman scatter from the C4=C5 vibrations. This is due to the disruption of base stacking of the guanine and adenine rings [29, 97], which reduces the shielding of the interior base rings from the incident UV light. The fact that the radiation-induced intensity increase in the 257 nm difference spectrum, where guanine vibrations are the primary contributor to the peak (see table 5.1 and figures 4.3(b)), is larger than the increase in the 264 nm difference spectrum, where adenine vibrations are dominant (table 5.1 and 4.3(c)) has been noticed in previous studies [97] and implies that guanine is more sensitive to the radiation-induced changes caused by base un-stacking. Considering this, the minimal increase in this peak in the 248 nm difference spectrum is puzzling as guanine vibrations dominate here as well (table 5.1 and figure 4.3(a)), but this discrepancy may be related to the lower spectral SNR, evident in figure 5.2(d).

An increase and wavenumber downshift in the 1604 cm^{-1} peak of each of the CT-DNA difference spectra is also evident in figure 5.3(a). Due to the fact that this peak corresponds to hydrogen bonding sensitive vibrations (eg. the NH_2 bend of adenine [33] and the N1-H stretching of guanine [33], see table 5.1 and figures 5.3(c) and (d)) the wavenumber shift suggests the disruption of the hydrogen bonds (H-bonds) between the bases. Previous studies have noticed this peak shift due to

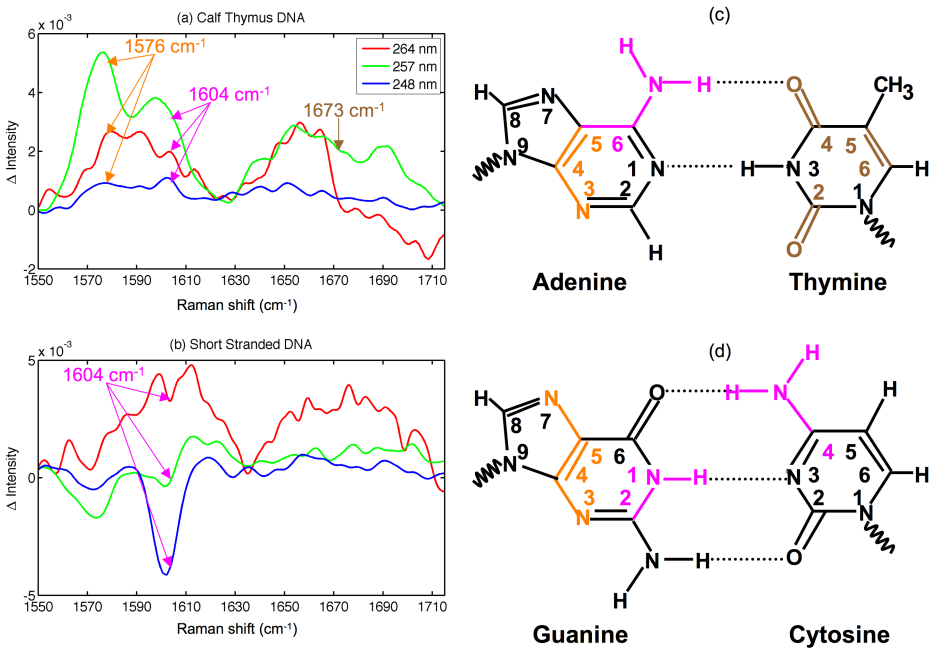

Figure 5.3: (a) Difference spectra for CT-DNA in the wavenumber region 1550 cm^{-1} - 1700 cm^{-1} (b) Difference spectra for SS-DNA (c) Adenine and Thymine diagrams with molecular groups colour coded to match corresponding Raman peaks (d) Guanine and Cytosine diagrams colour coded as in (c).

DNA melting [36], and in this case the additional intensity increase likely represents base unstacking, which is related to DNA denaturation [29, 91, 97]. At an excitation wavelength of 248 nm, the peak at 1604 cm^{-1} also has a strong contribution from the NH_2 bending vibration of cytosine [33] (table 5.1 and figure 5.3(d)), suggesting the breaking of the interbase H-bonds in which the NH_2 group of cytosine is involved, as well.

At all incident wavelengths, increases with radiation are observed throughout the broad band in the high wavenumber portion of this region (see figure 5.3(a)). This band is comprised of overlapping peaks that all correspond primarily to the stretching of C=O bonds of cytosine, thymine and guanine [33, 36, 91] (see table 5.1). Intensity increases are particularly small in the 248 nm difference spectrum, but this is likely due to the low SNR of the difference spectrum. More significant intensity increases

are observed in the 257 nm difference spectrum, however, it is known from section 4.2.2 that radiation-induced effects to the buffer may have an influence in this region. However, the fact that all difference spectra show an intensity increase in this region suggests that the spectral features are due to radiation-induced changes to DNA.

The peak at 1673 cm^{-1} is known to correspond primarily to C=O stretches on the thymine ring and is highly sensitive to hydrogen bonding of the bases [29, 36, 91, 97] (table 5.1 and figure 5.3(c)). In other studies, it's intensity increase along with a wavenumber shift have been attributed to base unstacking and the breaking of hydrogen bonds between thymine and adenine [29, 97, 98]. The absence of a wavenumber shift of the peak in the current study does not negate the possibility of the breaking of inter-base hydrogen bonds, as base unstacking (represented by the increase) is known to be highly related to this process [29, 91, 97]. Similarly, the intensity increase of the peak at 1650 cm^{-1} (sensitive to the C2=O stretch in cytosine [33]) in the difference spectra corresonding to each incident wavelength (figure 5.3(a)) is likely also related to both base unstacking of cytosine and guanine, and the breaking of hydrogen bonds between them. Finally, the peak at 1690 cm^{-1}, which is only visible in the 257 nm spectrum (figure 5.3(a)), relates to C=O stretches on both the thymine and guanine molecule and it's increase further points to both base unstacking and the breaking of hydrogen bonds [91].

SS-DNA: The difference spectra of the SS-DNA (figure 5.2(f)-(g) and figure 5.3(b)) generally show less intense changes in this wavenumber region than those of the CT-DNA, apart from the 264 nm difference spectrum, which shows intensity changes comparable in magnitude to those in the CT-DNA difference spectra. However, there is a lack of intensity change in the 1576 cm^{-1} peak in all of the SS-DNA difference spectra, and as this is sensitive to base stacking [29, 97] (table 5.1), it is implied that base un-stacking has a less significant effect on the spectra of the irradiated SS-DNA.

The peak at 1604 cm^{-1} is better resolved in the SS-DNA spectra than those of the

CT-DNA, and shows an intensity change in the 248 and 264 nm difference spectra (figure 5.3(b)). As in the CT-DNA difference spectra, the peak increases in the 264 nm difference spectrum, again relating to the disruption of the hydrogen bonds of adenine and guanine and base un-stacking. However, in the 248 nm difference spectrum, a small decrease is observed in the peak intensity at 1604 cm^{-1}. At an excitation wavelength of 248 nm, this peak corresponds to the NH_2 bend of the adenine and cytosine ring (table 5.1 and figures 5.3(c) and (d)), which is involved in Watson Crick (WC) H-bonding. It's decrease indicates a reduction in the Raman scatter from the NH_2 bending mode, suggesting radiation-induced damage to this moiety, but perhaps also partial denaturation of the DNA strands, as a decrease in this peak has previously been observed due to DNA melting [36]. The decrease is overwhelmed by the intensity increase at 1604 cm^{-1} in the 264 nm difference spectrum, and this is likely due to the weak contribution of the cytosine moiety to the peak at this wavelength (table 5.1 and figure 4.3(c)).

No radiation-induced spectral change is observed in the 1604 cm^{-1} peak in the 257 nm spectrum (figure 5.3(b)), but this can be attributed to the reduced adenine contribution to the peak, which was more significant in the 248 and 264 nm spectra (see figures 4.3(a)-(c)). At higher wavenumbers in this region, where the spectral peaks correspond to C=O stretching vibrations on the cytosine, thymine and guanine ring (see table 5.1), no significant intensity change is observed either. This, again, is unlike the situation in the CT-DNA, but may be due to the reduced significance of base stacking in the SS-DNA difference spectra, as base unstacking involving the C=O bonds likely contributes to the intensity increase with radiation of the 1650 cm^{-1} and 1673 cm^{-1} peaks in the CT-DNA difference spectra [97].

5.1.2 1450 - 1550 cm^{-1}

CT-DNA: In all of the difference spectra in figure 5.4(a), an increase is visible in the intense peak at 1486 cm^{-1}. This increase relates to the un-stacking of the adenine

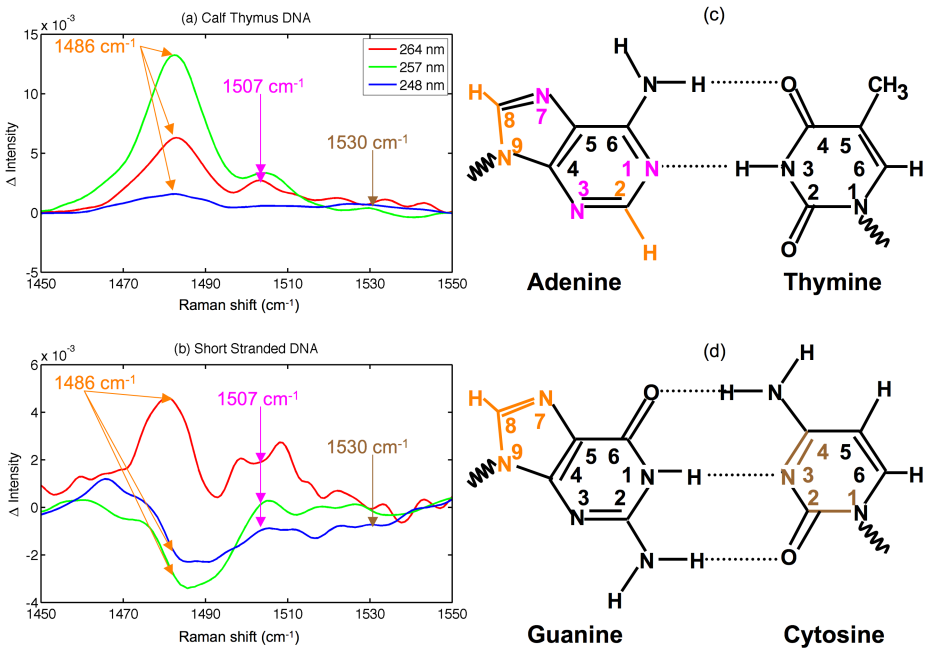

Figure 5.4: (a) Difference spectra for CT-DNA in the wavenumber region 1450 cm^{-1} - 1550 cm^{-1} (b) Difference spectra for SS-DNA (c) Adenine and Thymine diagrams with molecular groups colour coded to match corresponding Raman peaks (d) Guanine and Cytosine diagrams colour coded as in (c).

and guanine rings, allowing Raman scatter from the C8-N9 stretching vibration of both bases, and the N7=C8 vibration of guanine (see table 5.1 and figure 5.4(c) and (d)), to increase in intensity [91]. The fact that the intensity increase is large at all incident UV wavelengths, including the 248 nm difference spectrum where the guanine vibrations are the primary contributors to the peak instead of the adenine vibrations as in the other spectra (see table 5.1 and 4.3(a)-(c)), confirms that both adenine and guanine experience this radiation-induced base un-stacking.

An increase in the peak at 1507 cm^{-1} can also be seen in the 264 and 257 nm difference spectrum (figure 5.4(a)). As this peak is sensitive to hydrogen bonding at the nitrogen-acceptor sites of adenine [91] (N1 or N3 & N7, see table 5.1 and figure 5.4(c)), it's increase may be related to the breaking of hydrogen-bonds suggested by the peak at 1604 cm^{-1}. This is reinforced by the prescence of a slight increase in this

peak caused by DNA melting in a previous study [36]. No increase with radiation is seen at 1507 cm^{-1} in the 248 nm spectrum (figure 5.4(a)), but this is likely due to low spectral SNR.

Despite the absence of change at 1507 cm^{-1}, a weak intensity increase is observed at 1530 cm^{-1} in the 248 nm difference spectrum (figure 5.4(a)). This peak relates to the N3=C4 and N1-C2 stretching vibrations of cytosine [33] (figure 5.4(d)). It is sensitive to WC H-bonding at N3, and it's increase has also been observed in studies of DNA melting [97]. Thus, it likely corresponds to radiation-induced base unstacking and partial denaturation, much like the guanine peaks at 1576 cm^{-1} and 1604 cm^{-1} which correspond to similar vibrations on the guanine ring (see table 5.1 and figure 5.3(d)).

SS-DNA: Unlike the CT-DNA, the 1486 cm^{-1} peak observed in the 257 and 248 nm difference spectra (figure 5.4(b)) shows a radiation-induced intensity decrease. This points to base damage to both adenine and guanine [29] (see table 5.1 and figures 5.4(c) and (d)), or a change in base stacking interactions [36] , and may indicate the separation of the backbone from the bases as N9 on each base ring connects to the backbone. While no decrease is observed in the 264 nm difference spectrum (figure 5.4(b)), this may be due to the decreased contribution from guanine vibrations to the peak at this incident wavelength (see table 5.1 and figure 4.3(c)). While guanine is not abundant in SS-DNA, it is in an important position holding the ends of the DNA molecule together, where it experiences less shielding due to base stacking.

Intensity decreases with radiation in the peaks at 1507 and 1530 cm^{-1} in the 248 nm difference spectrum can also be observed in figure 5.4(b), pointing to base damage of adenine, and cytosine (see table 5.1). Also, the decrease may point to the destruction of Watson-Crick H-bonds, as the peak at 1507 cm^{-1} is sensitive to H-bonding at N1 in adenine, and the peak at 1530 cm^{-1} corresponds to N1-C2 and

N3=C4 stretching vibrations of cytosine that are sensitive to H-bonding (see table 5.1 and figures 5.4(c) and (d)). In the 264 and 257 nm difference spectra (figure 5.4(b)), intensity changes are not observed in the peaks at 1507 and 1530 cm^{-1}, apart from a small increase in the peak at 1507 cm^{-1} in the 264 nm data. While the contradictory changes in the 1507 cm^{-1} peak of the 264 and 248 nm difference spectra are not well understood, the lack of intensity decrease of the 1530 cm^{-1} peak in the 257 and 264 nm difference spectrum is likely a result of poor resolution of this peak when using these incident wavelengths.

Generally, the SS-DNA spectra show intensity decreases in their difference spectra in this region, while those of CT-DNA showed increases. This suggests that base unstacking occurs at a lower dose for SS-DNA than for CT-DNA, reducing shielding to the interior of the SS-DNA molecule allowed by the stacked structure, and leaving it vulnerable to radical attack [26, 29]. The subsequent radiation-induced damage to the SS-DNA results in the reduced Raman scatter from its molecular bonds, which is represented by the intensity decreases.

5.1.3 1300 - 1450 cm^{-1}

CT-DNA: Peaks in this region are particularly well defined and intense, and strong intensity changes are visible in the difference spectra. The peaks at 1310, 1335 and 1375 cm^{-1} all show strong increases in the difference spectra corresponding to each of the incident UV wavelengths (figures 5.5(a)). These increases are due to radiation-induced disturbances of the base stacked structure of the DNA molecule, as the peaks at 1310 cm^{-1} and 1335 cm^{-1} are both sensitive to molecular vibrations of bonds on the adenine ring that are involved in base stacking [33, 97] (C2=N3 and N7=C8 stretches, see table 5.1 and figure 5.5(c) adn (d)). The increase of the peak at 1375 cm^{-1} points to base unstacking of the thymine and guanine rings, due to the fact that the peak is partially due to thymine ring stretching vibrations in all of the spectra, and has a primary contribution from stretches on the ring of guanine in the 248 nm

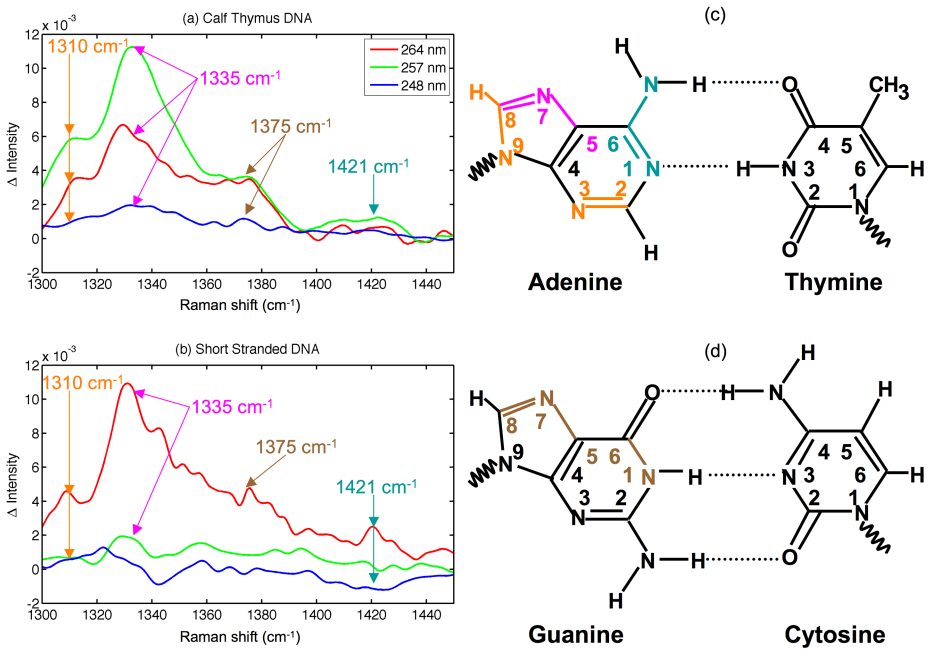

Figure 5.5: (a) Difference spectra for CT-DNA in the wavenumber region 1300 cm^{-1} - 1450 cm^{-1} (b) Difference spectra for SS-DNA (c) Adenine and Thymine diagrams with molecular groups colour coded to match corresponding Raman peaks (d) Guanine and Cytosine diagrams colour coded as in (c).

spectrum (table 5.1 and figures 4.3(a)).

The increase at 1375 cm^{-1} in the 248 nm spectrum (figure 5.5(a)) may also point to the radiation-induced disruption of inter-base hydrogen bonds between guanine and cytosine, this time of those involving the N1 molecule of guanine (table 5.1 and figure 5.5(d)). The suggestion of the disruption of H-bonds is reinforced by an increase of the 1421 cm^{-1} peak observed in the 257 nm difference spectrum (figure 5.5(a)), as this peak has a contribution from the H-bonding sensitive N1=C6 and C6-N stretches on the adenine ring [33] (table 5.1 and figure 5.5(c)).

It is also known that the 1421 cm^{-1} peak corresponds to a vibration of the deoxyribose backbone [36], and while the exact nature of the vibration is unknown, the intensity increase in the 257 nm difference spectrum may point to some kind of radiaton-induced effect to the backbone. This would result in a change in backbone

conformation or damage to base-backbone bonds. Any intensity change in this peak in the 248 nm and 264 nm difference spectra is likely lost in the spectral noise.

SS-DNA: Like that of the CT-DNA, the 264 nm difference spectrum (figure 5.5(b)) of SS-DNA shows an intensity increase in the peaks 1310 cm^{-1}, 1335 cm^{-1} and 1375 cm^{-1}. As a result, the interpretation of the 264 nm difference spectrum in this region is very similar to that of CT-DNA, in that the radiation-induced increases at 1310, 1335, and 1375 cm^{-1} are due to base unstacking. However, in the 257 nm difference spectrum, while the 1310 and 1335 cm^{-1} peaks show intensity increases, the 1375 cm^{-1} peak does not, and only the 1310 cm^{-1} peak shows an increase in the 248 nm difference spectrum (figure 5.5(b)). This is likely related to the fact that at an incident wavelength of 264 nm, adenine vibrations are the main contributor to the peaks at 1310, 1335 and 1375 cm^{-1}, while in the 248 and 257 nm spectra, guanine vibrations becomes more significant in the 1335 and 1375 cm^{-1} peaks (see table 5.1 and figures 4.3(a)-(c)). The fact that the SS-DNA contains a small amount of guanine and cytosine relative to adenine and thymine means that peaks sensitive to guanine will be less intense than those of adenine and thymine. This weaker signal may partially explain the fact that intensity increases are weak, or nonexistant at these peaks in the 248 and 257 nm difference spectra.

The 1421 cm^{-1} peak shows a small increase in the 264 nm difference spectrum, no change in the 257 nm difference spectrum, and a decrease in the 248 nm difference spectrum (figure 5.5(b)). While changes in this peak in the 257 nm difference spectrum are lost in the spectral noise, the increase observed when the DNA is probed with 264 nm light may correspond to the breaking of inter-base hydrogen bonds between adenine and thymine, as in the CT-DNA spectra. The intensity decrease of the peak in the 248 nm difference spectrum is likely due to the strong influences of the cytosine, guanine and thymine rings to this peak when acquired at 248 nm (see table

5.1 and figure 4.3(a)) as opposed to the other wavelengths. The decrease implies damage to cytosine, guanine and thymine, and could also be indicative of damage to the deoxyribose backbone [29, 36]. However, the low SNR of the difference spectrum around 1421 cm^{-1}, as seen in figure 5.5(b), makes interpretation of the changes in the spectral features around this peak difficult.

5.1.4 1100 - 1300 cm^{-1}

CT-DNA: In this region, there is a high degree of overlap between low intensity peaks (see figure 5.2(a)). Upon careful investigation, only the 264 nm difference spectrum (figure 5.6(a)) shows any radiation-induced change. In this spectrum, the peaks at 1240 cm^{-1} and 1252 cm^{-1} show a small intensity increase. The peak at 1240 cm^{-1} has contributions from vibrational ring modes of thymine and cytosine [33], and ring modes of adenine and cytosine influence the peaks at 1252 cm^{-1} [33, 36] (table 5.1). All of these vibrations involve double bonds, and as such, the increase in these peaks is indicative of radiation-induced base unstacking[29, 97–99]. Due to the fact that the peak at 1252 relates to vibrations involving N1 and the NH_2 group of adenine, as well as a stretch between C4 and the NH_2 group of cytosine (table 5.1 and figures 5.6(c) and (d)), which are all sensitive to hydrogen bonding, its increase suggests that the base unstacking is related to the breaking of these inter-base hydrogen bonds[29, 97]. While intensity changes are not visible in the 248 and 257 nm difference spectra, it is likely due to the reduced contributions of the thymine and cytosine vibrations in this region (see figure 4.3(a)-(c)).

SS-DNA: As in the CT-DNA spectra, the peaks of the SS-DNA spectra are weak in this region, and poorly resolved. Changes in the difference spectra are visible, however, this time in the 1168 cm^{-1} peak of the 264 nm difference spectra, and the 1185 cm^{-1} peak of the 248 nm difference spectrum (figure 5.6(b)). When probed with any of the UV wavelengths used, the peak at 1168 cm^{-1} corresponds to the

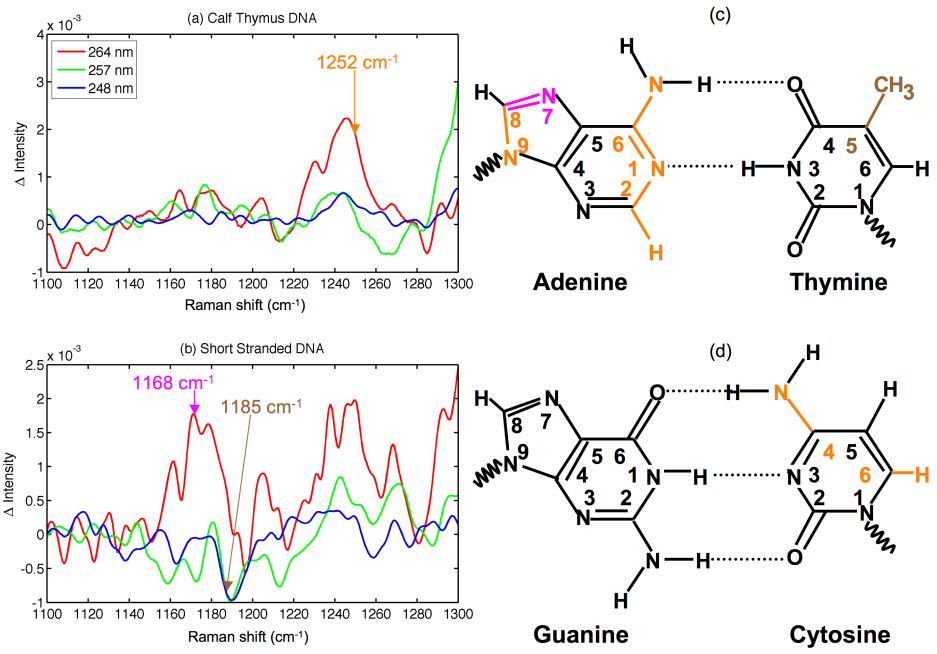

Figure 5.6: (a) Difference spectra for CT-DNA in the wavenumber region 1100 cm^{-1} - 1300 cm^{-1} (b) Difference spectra for SS-DNA (c) Adenine and Thymine diagrams with molecular groups colour coded to match corresponding Raman peaks (d) Guanine and Cytosine diagrams colour coded as in (c).

N7=C8 stretching vibration of the adenine ring, and the N1-C2 and C6-NH_2 vibrations that are also represented by the 1252 cm^{-1} peak [33] (table 5.1 and figure 5.6(c)). The involvement of a double bond implies that the increase of this peak in the 264 nm difference spectrum corresponds to radiation-induced base un-stacking. Also, it suggests the breaking of the hydrogen bonds in which N1 and the NH_2 group are involved, as did the increase at 1252 cm^{-1} in the 264 nm CT-DNA difference spectrum. The fact that the intensity increase at 1168 cm^{-1} is only visible in the 264 nm difference spectrum is due to the higher intensity and better resolution of the peak in this spectrum as compared to the 248 and 257 nm spectra, as seen in figure 5.2(e).

Like the peak at 1168 cm^{-1}, that at 1185 cm^{-1} is related to adenine vibrations. In the 248 nm spectrum, adenine vibrations are the primary contributor to the peak

(see figure 4.3(a)), and the decrease in the 1185 cm^{-1} peak in the 248 nm difference spectrum thus relates to damage to the adenine ring. However, when acquired at an incident wavelength of 264 nm or 257 nm, adenine vibrations are only a secondary contribution to the peak, while the C5-CH_3 stretch of thymine is primary [33] (see table 5.1 and figure 5.6(c)). Thus, the absence of an intensity decrease in the 1185 cm^{-1} peak in these difference spectra means that radiation damage to the C5-CH_3 bond of thymine is not detected. This may be due to the fact that the peak at 1185 cm^{-1} is known to be diagnostic of unpaired thymine [91], and if radiation-induced damage has caused sufficient denaturation of the DNA strands, the resultant increase of the peak at 1185 cm^{-1} may counteract any decrease due to adenine damage.

5.1.5 700 - 1100 cm^{-1}

CT-DNA: The peaks in the 700-900 cm^{-1} region are poorly resolved in the CT-DNA spectra, as can be seen in figure 5.2(a). At each wavelength, a broad band appears in this region, which is a combination of several peaks. The width of this band varies with wavelength, but all achieve their maxima at $\sim$785 cm^{-1}. While the band in the 264 and 248 nm difference spectra shows no obvious changes, the 257 nm difference spectrum (figure 5.7(a)) shows a slight decrease in this band. As was mentioned in section 4.2.2, this is another of the regions in which radiation-induced changes in the buffer need to be considered when observing spectra acquired at 257 nm. This may imply that the decrease seen in figure 5.7(a) is due to changes in the buffer, and not the CT-DNA. However, as can be seen from table 5.1, there are DNA peaks in this region, and the primary contributor to the broad band in this range is the cytosine peak at $\sim$ 785 cm^{-1}, which corresponds to ring breathing [29, 33]. The portion of the broad band that is above 800 cm^{-1} is likely due to O-P-O stretching in the backbone [91, 97, 100] (table 5.1). As a result, if not due to the buffer, the intensity decrease seen in the broad peak of the 257 nm spectrum points towards damage to the cytosine ring, as well as disruption of the backbone. It may also be an

indicator of the loss of the B-form conformation of the DNA [29, 91, 97]. Although no changes are observed in the 264 and 248 nm difference spectra in this region, this may be due to the low SNR of the band in the 248 nm spectra (figure 5.2(a)), and the reduced contribution from backbone vibrations to the band at wavenumbers greater than 800 cm^{-1} in the 264 nm spectrum (figure 4.3(c)).

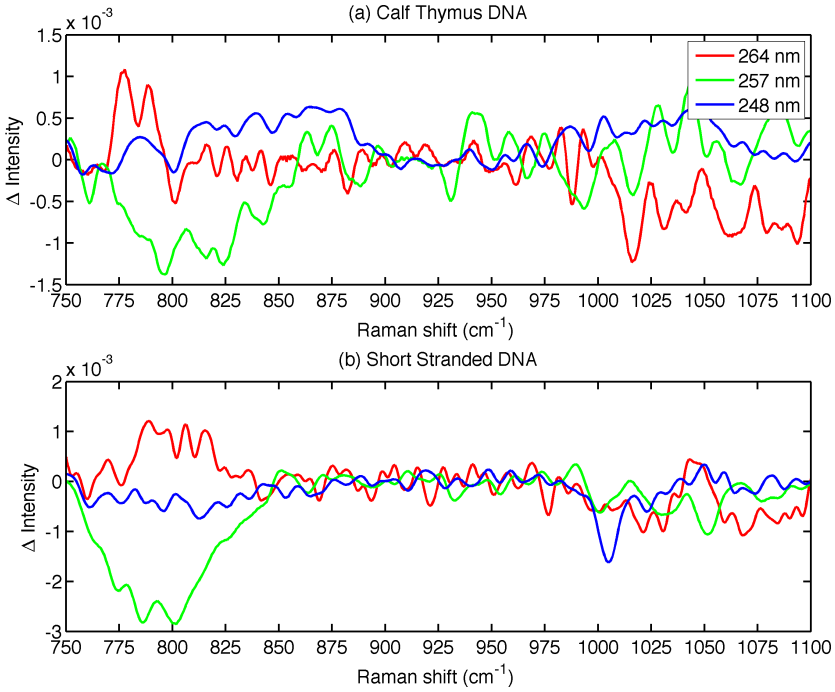

Figure 5.7: (a) Difference spectra for CT-DNA in the wavenumber region 700 cm^{-1} - 1100 cm^{-1} (b) Difference spectra for SS-DNA.

SS-DNA: As is the case with the CT-DNA, the peaks in this region are poorly resolved (see figure 5.2(e)), and the width of the broad band with a maximum at 785 cm^{-1} is the same in each SS-DNA spectrum as in the CT-DNA spectrum acquired at the corresponding wavelength. Again, there is no obvious radiation-induced spectral change in the 264 nm difference spectra (figure 5.7(b)), but the band shows a decrease in both the 257 and 248 nm difference spectra. The decrease is particularly significant at an incident wavelength of 257 nm. Similarly to the CT spectrum, the decrease of this broad band is likely an indicator of damage to both the cytosine ring and

the deoxyribose backbone, so long as the buffer is not playing a significant effect. The fact that the decrease is present in the 248 nm difference spectrum as well is encouraging, as radiation-induced effects of the buffer were deemed negligible at this incident wavelength (see section 4.2.2). The reason that the decrease is visible in the 248 nm difference spectrum of SS-DNA, and not that of CT-DNA (figure 5.7(a)) is not abundantly clear, but may simply be due to better SNR in this region for the SS-DNA spectrum. Likewise, poor SNR in this region, as well as a reduced contribution from backbone vibrations to the peak in the 264 nm spectrum (figure 4.3(c)), are likely the reason for the lack of an intensity change in the 264 nm difference spectrum.

Unlike the difference spectra of the CT-DNA, there is a further intensity decrease observed in the 248 nm difference spectrum in the peak at 1005 cm^{-1} (figure 5.7(b)). This peak is not visible in the spectra of the CT-DNA (figure 5.2(a)), or in the 264 nm spectrum of the SS-DNA (figure 5.2(e)). While present in the 257 nm SS-DNA spectrum (figure 5.2(e)), it shows no change with radiation (see figure 5.7(b)), likely due to poor SNR. The peak at $\sim$ 1005 cm^{-1} is due primarily to cytosine, with secondary contributions from adenine, as can be seen from figure 4.3 and table 5.1. The precise assignment of this peak is currently unknown, but it is particularly prominent in the 248 nm spectrum (figure 5.2(e)), and it's decrease implies that the cytosine and adenine rings are experiencing some form of radiation-induced damage.

5.2 General Discussion

Through the observation of the specta acquired pre- and post-irradiation, it is evident that the $\sim$ 2000 Gy of ionizing radiation had a significant effect on both the CT and SS-DNA. The use of varying incident UV wavelengths allowed the unique opportunity to better probe different moieties of the DNA molecule, and the spectra of the short strands of the individual bases (figure 4.3) helped to confirm the assignments of the peaks and the relative contributions of the four bases at each of the three incident

wavelengths.

In general, at all incident wavelengths, the radiation-induced spectral differences were more noticeable in the CT-DNA difference spectra. They were particularly significant at incident UV wavelengths of 257 and 264 nm, which is not surprising, as the vibrations of the bonds of all four DNA bases are near resonance when excited by UV light close to 260 nm [37], resulting in strong Raman scattering. Typically, spectral increases were observed in the difference spectra of the CT-DNA, which indicated an increase in Raman scatter from the molecular bonds to which the peaks corresponded. These increases were generally attributed to base un-stacking, as the disruption of the stacked, ordered structure of the CT-DNA by $OH^{\cdot}$ radicals reduced shielding of the interior of the DNA molecule [26, 29], allowing for more UV light photons to strike the bases. It was also assumed that these increases were indicators of partial DNA denaturation, as base un-stacking and denaturation typically occur cooperatively [29, 91, 97].

In contrast to those of the CT-DNA, spectral decreases were more prevalent in all difference spectra of the SS-DNA. The absence of increases implies that radiation-induced base unstacking had a less significant effect on the difference spectra of the SS-DNA. This is likely due to the disruption of the stacked structure of SS-DNA at a lower dose than that of the CT-DNA. If the SS-DNA was unstacked before the dose delivery was completed, then $OH^{\cdot}$ radicals would have easier access to the bases, as the interior of the DNA molecule would no longer be allowed the shielding provided by base stacking. This would explain the spectral decreases present in the SS-DNA difference spectra, as these are indicative of reduced Raman scatter from the molecular bonds of the bases to which the peaks correspond, due to radiation-induced damage and structural change to these bonds.

While changes were observed in the spectra of both SS and CT-DNA due to radiation, the increases in the CT-DNA spectra were much larger than the decreases

of the SS-DNA spectra. This does not necessarily mean that CT-DNA is more radiation sensitive than SS-DNA, but likely relates to the fact that the longer CT-DNA strand has a larger surface area, and as such is more susceptible to interactions with hydroxyl radicals. Also, while the exact composition of the CT-DNA is complicated, the SS-DNA was essentially composed of adenine-thymine base pairs. As the Raman spectrum is essentially an average of the entire sample, scatter from damaged adenine and thymine rings is detected along with significant scatter from undamaged adenine and thymine rings. This averaging partially explains the need for the high dose delivered to the samples, as high doses result in more damaged bases and fewer undamaged bases present in the sample, and thus the contribution to the spectral signal from damaged bases is dominant.

Although the fluctuations in the difference spectra shown in figure 5.2 are the result of one experimental trial, there is confidence in the results obtained due to the fact that similar changes are observed in the spectra of the corresponding samples acquired at each of the incident wavelengths. Also, the irradiated and unirradiated DNA spectra used to calculate the difference spectra are each the average of five separate samples (section 3.5), and little spectral variation was found between samples of the same type. Furthermore, despite the low SNR of the difference spectra corresponding to the DNA samples irradiated to lower doses (section 4.3.3), fluctuations in these difference spectra showed similar trends to those of figure 5.2.

Ultimately, the fact that the findings presented in this research are consistent with similar studies performed on damage to DNA provides the strongest evidence for the accuracy of the experiment. While previous studies have focused mainly on the use of Raman spectroscopy to determine damage to DNA due to excessive heating [38–40], or UV radiation [35, 36, 38, 40, 89, 91, 101], all of the DNA damage caused by these external factors is also caused by ionizing radation [102]. As in this work, these previous studies provided evidence of base unstacking, base damage, and strand

breaks, but with the additional evidence of changes in DNA conformation. In one of the few other studies using Raman spectroscopy to study ionizing radiation-induced damage to DNA, Sailer *et al*[29] used FT-Raman spectroscopy to observe damage to CT-DNA. As in this study, and those involving heat and UV damage, Sailer *et al* were able to determine base-unstacking, base damage and denaturation of the DNA strand. However, like the heat and UV damage studies, they also observed evidence of a conformation change of the DNA strand, and the loss of B-form DNA. This information was not as evident in this research, but is likely due to the increased sensitivity of UVRRS to the DNA bases, and decreased sensitivity to moieties of the backbone. For example, the spectra presented by Sailer *et al* were better resolved in the low wavenumber region (500-1100 cm^{-1}) than the spectra presented in this work and the low wavenumber region is highly sensitive to backbone conformation [29]. However, by using incident UV light in this research, superior molecular sensitivity was obtained in peaks due to vibrations on the base rings (1300-1700 cm^{-1}) [37]. This allowed for the identification of the ionizing radiation-induced damage to the bases observed by Sailer *et al*, and, along with the high intensity of the spectra achieved with UVRRS, enabled the detection of this damage at a low dose relative to those used by Sailer *et al* (up to 40 000 Gy).

This research also had the added benefit of the high molecular specificity of UVRRS, which was enhanced through the use of varying incident UV wavelengths. For example, in the case of the peak at 1486 cm^{-1}, which is due to ring stretches of adenine and guanine, the primary peak contribution changed from vibrations of adenine at an incident UV wavelength of 257 and 264 nm, to those of guanine at 248 nm (see table 5.1 and figure 4.3). This confirmed that the increase of the peak at 1486 cm^{-1} with radiation, which was observed in all the CT-DNA difference spectra (see figure 5.4(a)), related strongly to radiation-induced effects to guanine as well as adenine. A similar situation involving the peak at 1604 cm^{-1} allowed damage to

the adenine ring and its Watson-Crick H-bonds to be visualized in the SS-DNA 248 nm difference spectrum (figure 5.3(b)), where adenine vibrations dominated the peak (table 5.1 and figure 4.3), while it was not visible in the other difference spectra where vibrations of guanine had a stronger influence on the peak. In another instance, the superior resolution of the peak at 1530 cm^{-1} in the 248 nm difference spectrum, corresponding to the H-bonding sensitive stretches of the N3=C4 and N1-C2 bonds in the cytosine ring (see table 5.1 and figure 5.4(d)), meant that a radiation-induced increase in this peak was only visible in the difference spectrum corresponding to this wavelength. While these examples all relate to the 248 nm spectra, this is due to the fact that this wavelength was significantly lower than the closely spaced 257 and 264 nm wavelenths, and thus excited different molecular bonds. However, the supporting data from the 257 and 264 nm spectra was critical, as the bases are generally much closer to resonance at these wavelengths [37], and radiation-induced differences were much more obvious in these spectra.

It is all of this information in concert that makes the use of UVRRS with varying incident UV wavelengths useful in the study of radiation-induced damage to DNA. Ultimately, the presence of radiation-induced spectral differences in both the CT and SS-DNA data is encouraging, and provides a case for further study into the use of UVRRS for this purpose.

Chapter 6

Conclusions

6.1 Conclusions

Throughout this work, the effects of ionizing radiation on calf-thymus DNA, and a short stranded DNA sequence were investigated through the use of Raman spectroscopy using a variety of incident excitation wavelengths. Ultimately, at the low DNA concetration used (0.5 mg/mL), only the UV resonance Raman technique, using 248, 257 and 264 nm light, resulted in an appreciable signal from the DNA molecules. This technique provided intense, characteristic spectra of short single strands of each of the four bases, as well as of the 30-mer DNA oligomer (SS-DNA) and calf-thymus DNA (CT-DNA). At all incident wavelengths, difference spectra between the irradiated and unirradiated samples of SS and CT-DNA showed spectral changes, most of which could be attributed to the effects of ionizing radiation. Spectral increases were particularly significant in the CT-DNA difference spectra, and were indicitave of base un-stacking due to radiation-induced damage to overlapping pi-bonds of the base rings, as well as strand denaturation. The difference spectra of the SS-DNA primarily showed spectral decreases, representative of radiation-induced damage to the molecular structure of the bases. Increases due to base unstacking were not as evident in the SS-DNA difference spectra, likely indicating that this process occurred rapidly in the SS-DNA, allowing the ionizing radiation access to the interior of the

DNA molecule and resulting in significant damage to the bases themselves.

In using UVRRS, the spectral information obtained related primarily to the DNA bases and allowed for detailed analysis of the radiation-induced effects to the molecules of the base rings. This was aided by the acquisition of the DNA spectra at incident UV wavelengths of 248, 257 and 264 nm. The spectra acquired at these different wavelengths all shared the same characteristic spectral peaks of the DNA molecules, but the contributions of the individual bases to each peak varied with incident wavelength. Using this variation, alongside previous literature on the topic and characteristic spectra of each of the four bases, it was possible to determine the molecular bonds of the bases to which the radiation-induced spectral changes could be attributed.

Ultimately, the UVRRS technique as described in this work proved useful in the study of DNA, as it provided a strong characteristic DNA signal, and was relatively easy to implement. It also had the benefits of simple sample preparation and short acquisition times ($\sim$10 s). Although a high dose to the DNA was required in order to identify significant radiation-induced spectral differences, the dose delivered was on the low end of those previously used in similar studies [29]. It is feasible to assume that with refinement of the technique, and further study of various DNA and other biological samples, that significant information as to the radiation-induced effects to biology could be obtained.

6.2 Future Directions

As was mentioned in the conclusion, an inconvenience of the UVRRS technique was the magnitude of the dose required to see significant radiation-induced spectral changes in the difference spectra. Ideally, the utility of the information obtained would be improved if biological damage due to clinically relevant doses could be determined. Considering recent research involving Raman spectroscopic analysis, this

seems feasible, as radiation damage was detected in tissue samples irradiated by protons [30] to doses below 60 Gy (a clinically relevant range). Why these effects are present at such low doses in spectra of the tissue samples and not the DNA samples of the current research is unclear, but is likely related to the artificial conditions of the pure DNA samples. However, the study of more biologically relevant samples, such as cells and tissue samples is very possible with the use of Raman spectroscopy, and a particularly promising field of study involves the use of Raman microscopy. With this technique, it would be possible to obtain two-dimensional spectroscopic information of the samples, which would help in the analysis of complicated systems composed of a variety of parts, such as cells [103, 104]. Analysis of DNA damage would still be an important part of this work, as it is possible to locate the DNA in the nucleus of a cell [105–109]. While the analysis of biological systems would add a degree of complexity to the Raman spectroscopic study of radiation-induced damage, experience gained from the UVRRS technique would prove invaluable in this process, and UVRRS could be extended to work in collaboration with Raman microscopic techniques.

Bibliography

[1] Otto Glasser. Wilhelm Conrad Röntgen and the early history of the Roentgen rays. C. C. Thomas, Springfield, IL, 1934.

[2] Denis Brian. The Curies: A Biography of the Most Controversial family in Science. J. Wiley, Hoboken, NJ, 2005.

[3] NCIC. Canadian cancer statistics. Technical report, National Cancer Institute of Canada, 2007.

[4] H. E. Johns and J. R. Cunningham. The Physics of Radiology. Charles C Thomas Publisher, Springfield, IL, 1983.

[5] F. M. Khan. The Physics of Radiation Therapy. Lippincott Williams & Wilkins, Philadelphia, PA, 3rd edition, 2003.

[6] D.C. Rizzo. Fundamentals of Anatomy & Physiology. Thomson Delmar Learning, Clifton Park, NY, 2nd edition, 2006.

[7] J. D. Watson and F. H. C. Crick. Molecular Structure of Nucleic Acids: A Structure for Deoxyribose Nucleic Acid. Nature, 171(4356):737–738, 1953.

[8] K.M. Guckian, B.A. Schweitzer, R.X.-F. Ren, C.J. Sheils, P.L. Paris, D.C. Tahmassebi, and E.T. Kool. Experimental Measurement of Aromatic Stacking Affinities in the Context of Duplex DNA. Journal of the American Chemical Society, 118(34):8182–8183, 1996.

[9] E.T. Kool. Preorganization of DNA: Design Principles for Improving Nucleic Acid Recognition by Synthetic Oligonucleotides. Chemical Reviews, 97(5):1473–1488, 1997.

[10] Susan M. Freier, Naoki Sugimoto, Alison Sinclair, Dirk Alkema, Thomas Neilson, Ryszard Kierzek, Marvin H. Caruthers, and Douglas H. Turner. Stability of XGCGCp, GCGCYp, and XGCGCYp helixes: an empirical estimate of the energetics of hydrogen bonds in nucleic acids. Biochemistry, 25(11):3214–3219, 1986.

[11] Matthew Petersheim and Douglas H. Turner. Base-stacking and base-pairing contributions to helix stability: thermodynamics of double-helix formation with CCGG, CCGGp, CCGGAp, ACCGGp, CCGGUp, and ACCGGUp. Biochemistry, 22(2):256–263, 1983.

[12] Lisa F. Newcomb and Samuel H. Gellman. Aromatic Stacking Interactions in Aqueous Solution: Evidence That neither Classical Hydrophobic Effects nor Dispersion Forces Are Important. Journal of the American Chemical Society, 116(11):4993–4994, 1994.

[13] Ray Luo, Hillary S. R. Gilson, Michael J. Potter, and Michael K. Gilson. The Physical Basis of Nucleic Acid Base Stacking in Water. Biophysical Journal, 80(1):140–148, 2001.

[14] P. K. Ponnuswamy and M. Michael Gromiha. On the Conformational Stability of Oligonucleotide Duplexes and tRNA Molecules. Journal of Theoretical Biology, 169(4):419–432, 1994.

[15] RE Dickerson, HR Drew, BN Conner, RM Wing, AV Fratini, and ML Kopka. The anatomy of A-, B-, and Z-DNA. Science, 216(4545):475–485, 1982.

[16] A. G. W. Leslie, Struther Arnott, Rengaswami Chandrasekaran, and R. L. Ratliff. Polymorphism of DNA double helices. Journal of Molecular Biology, 143(1):49–72, 1980.

[17] Timothy J. Richmond and Curt A. Davey. The structure of DNA in the nucleosome core. Nature, 423(6936):145–150, 2003.

[18] M.C. Wahl and M. Sundaralingam. Crystal structures of A-DNA duplexes. Biopolymers, 44(1):45–63, 1997.

[19] Xiang-Jun Lu, Zippora Shakked, and Wilma K. Olson. A-form Conformational Motifs in Ligand-bound DNA Structures. Journal of Molecular Biology, 300(4):819–840, 2000.

[20] J.R. Ferraro and K. Nakamoto. Introductory Raman Spectroscopy. Academic Press, Inc., San Diego, 1994.

[21] Eric J. Hall. Radiobiology for the Radiologist. Lippincott Williams & Wilkins, Philadelphia, PA, 6th edition, 2006.

[22] R. Teoule. Radiation-induced DNA Damage and Its Repair. International Journal of Radiation Biology, 51(4):573–589, April 1987.

[23] J. Cadet and M. Berger. Radiation-induced decomposition of the purin bases within DNA and related model compounds. International Journal of Radiation Biology, 47(2):127–143, 1985.

[24] A.F. Fuciarelli, B.J. Wegher, W.F. Blakely, and M. Dizdaroglu. Yields of radiation-induced base products in DNA: effects of DNA conformation and gassing conditions. International Journal of Radiation Biology, 58(3):397–415, 1990.

[25] Miral Dizdaroglu. Application of capillary gas chromatography-mass spectrometry to chemical characterization of radiation-induced base damage of DNA: Implications for assessing DNA repair processes. Analytical Biochemistry, 144(2):593–603, 1985.

[26] G. Scholes. Radiation effects on DNA. The British Journal of Radiology, 56:221–231, 1983.

[27] D. D. Ager, W. C. Dewey, K. Gardiner, W. Harvey, R. T. Johnson, and C. A. Waldren. Measurement of Radiation-Induced DNA Double-Strand Breaks by Pulsed-Field Gel Electrophoresis. Radiation Research, 122(2):181–187, 1990.

[28] K.S. Haveles, A.G. Georgakilas, E.G. Sideris, and V. Sophianopoulou. Effects of radical scavengers on radiation-induced DNA double strand breaks. International Journal of Radiation Biology, 76(1):51–59, 2000.

[29] K. Sailer, S. Viaggi, and M. Nusse. Radiation-induced structural modifications in dsDNA analysed by FT-Raman spectroscopy. International Journal of Radiation Biology, 69(5):601–613, 1996.

[30] A. Synytsya, P. Alexa, J. Besserer, J. De Boer, S. Froschauer, R. Gerlach, M. Loewe, M. Moosburger, I. Obstova, P. Quicken, B. Sosna, K. Volka, and M. Wurkner. Raman spectroscopy of tissue samples irradiated by protons. International Journal of Radiation Biology, 80(8):581–591, 2004.

[31] R. Jyothi Lakshmi, V. B. Kartha, C. Murali Krishna, J. G. R. Solomon, G. Ullas, and P. Uma Devi. Tissue Raman Spectroscopy for the Study of Radiation Damage: Brain Irradiation of Mice. Radiation Research, 157(2):175–182, 2002.

[32] Z. Q. Wen, S. A. Overman, and G. J. Thomas. Structure and interactions of the single-stranded DNA genome of filamentous virus *fd*: Investigation by

ultraviolet resonance Raman spectroscopy. Biochemistry, 36(25):7810–7820, 1997.

[33] Z. Q. Wen and G. J. Thomas. UV resonance Raman spectroscopy of DNA and protein constituents of viruses: Assignments and cross sections for excitations at 257, 244, 238, and 229 nm. Biopolymers, 45(3):247–256, 1998.

[34] I. Mukerji, M. C. Shiber, T. G. Spiro, and J. R. Fresco. Polynucleotides 23. A UV resonance Raman-study of D($A^{(+)}$-G)(10), a single-stranded helix without stacked or paired bases. Biochemistry, 34(44):14300–14303, 1995.

[35] I. Mukerji and A. P. Williams. Uv resonance Raman and circular dichroism studies of a DNA duplex containing an A(3)T(3) tract: Evidence for a premelting transition and three-centered H-bonds. Biochemistry, 41(1):69–77, 2002.

[36] S. S. Chan, R. H. Austin, I. Mukerji, and T. G. Spiro. Temperature-dependent ultraviolet resonance Raman spectroscopy of the premelting state of dA · dT DNA. Biophysical Journal, 72(4):1512–1520, 1997.

[37] M. Tsuboi, Y. Nishimura, A. Y. Hirakawa, and W. L. Peticolas. Resonance Raman spectroscopy and normal modes of the nucleic acid bases. In T. G. Spiro, editor, Biological applications of Raman spectroscopy., volume 2, pages 109–179. John Wiley and Sons, 1987.

[38] Weizhong Ke, Duowei Yu, and Jianzhong Wu. Raman spectroscopic study of the influence on herring sperm DNA of heat treatment and ultraviolet radiation. Spectrochimica Acta Part A: Molecular and Biomolecular Spectroscopy, 55(5):1081–1090, 1999.

[39] Yu-Long Tang and Zhou-Yi Guo. Raman Spectroscopic Analysis of the Effect of Ultraviolet Irradiation on Calf Thymus DNA. Acta Biochimica et Biophysica Sinica, 37(1):39–46, 2005.

[40] A. Jirasek, H. G. Schulze, C. H. Hughesman, A. L. Creagh, C. A. Haynes, M. W. Blades, and R. F. B. Turner. Discrimination between UV radiation-induced and thermally induced spectral changes in AT-paired DNA oligomers using UV resonance Raman spectroscopy. Journal of Raman Spectroscopy, 37(12):1368–1380, 2006.

[41] Adolf Smekal. Zur Quantentheorie der Dispersion. Naturwissenschaften, 11(43):873–875, 1923.

[42] C.V. Raman and K.S. Krishnan. A new type of secondary radiation. Nature, 121:501, 1928.

[43] F.P. Kerschbaum. Z. Instrumentenk, 34:43, 1914.

[44] B. Veskatesachar and L. Sibaiya. Indian Journal of Physics, 5:747, 1930.

[45] J.H. Hibben. The Raman Effect and Its Chemical Applications. Reinhold Publishing Corp., New York, 1939.

[46] D.H. Rank, R.J. Pfister, and P.D. Colman. Photoelectric detection and intensity measurement in Raman spectra. Journal of the Optical Society of America, 32:390–396, 1942.

[47] R.F. Stamm and C.F. Salzman. Photoelectric Raman spectrometer with automatic range change II: Conversion of Perkin-Elmer infrared instrument to grating type. Journal of the Optical Society of America, 43:126–137, 1953.

[48] T.R. Gilson and P.J. Hendra. Laser Raman Spectroscopy. Wiley-Interscience, London, 1970.

[49] J.R. Ferraro, R. Jarnutowski, and D.C. Lankin. Fifty Years of Commercial Instrumentation in Absorption Spectroscopy, Part I. Landmark Instruments in Infrared and Raman Spectroscopies. Spectroscopy, 7(2):30, 1992.

[50] E. Smith and G. Dent. Modern Raman Spectroscopy: A Practical Approach. John Wiley and Sons, Ltd., West Sussex, England, 2005.

[51] J. Tang and A.C. Albrecht. Developments in the theories of vibrational Raman intensities. In H.A. Szymanski, editor, Raman Spectroscopy, volume 2. Plenum Press, New York, 1970.

[52] D.L. Rousseau, J.M. Friedman, and P.F. Williams. Resonance Raman Scattering. Topics in Current Physics, 2:203, 1979.

[53] R.J.H. Clark and T.J. Dines. Theory of the resonance electronic Raman effect. Molecular Physics, 45(6):1153–1162, 1982.

[54] R.J.H. Clark and T.J. Dines. Resonance Raman Spectroscopy, and Its Application to Inorganic Chemistry. New Analytical Methods (27). Angewandte Chemie International Edition in English, 25(2):131–158, 1986.

[55] K. Nakamoto. Infrared and Raman Spectra of Inorganic and Coordinate Compounds. John Wiley and Sons, Ltd., New York, 1997.

[56] R. McCreery. Raman spectroscopy for chemical analysis, volume 157. John Wiley and Sons, New York, 2000.

[57] Coherent, Santa Clara, California. Operator's Manual - Innova 90C FreD Ion Laser, 2003.

[58] C. J. Barbosa, F. H. Vaillancourt, L. D. Eltis, M. W. Blades, and R. F. B. Turner. The power distribution advantage of fiber-optic coupled ultraviolet resonance Raman spectroscopy for bioanalytical and biomedical applications. Journal of Raman Spectroscopy, 33(7):503–510, 2002.

[59] L. S. Greek, H. G. Schulze, M. W. Blades, C. S. Haynes, K.F. Klein, and R. F. B. Turner. Fiber-optic probes with improved excitation and collection

efficiency for deep-UV Raman and resonance Raman spectroscopy. Applied Optics, 37:170–180, 1998.

[60] F.R. Perez, H.G.M. Edwards, A. Rivas, and L. Drummond. Fourier transform Raman spectroscopic characterization of pigments in the mediaeval frescoes at Convento de la Peregrina, Sahagun, Lèon, Spain. Part 1 - preliminary study. Journal of Raman Spectroscopy, 30(4):301–305, 1999.

[61] C. Cheng, T.E. Kirkbride, D.N. Batchelder, R.J. Lacey, and T.G. Sheldon. In Situ Detection and Identification of Trace Explosives by Raman Microscopy. Journal of Forensic Sciences, 40(1):31, 1995.

[62] W.E. Smith, C. Rodger, G. Dent, and P.C. White. Handbook of Raman Spectroscopy. Marcel Dekker, Inc., New York, 1st edition, 2001.

[63] P.C. Painter, M.M Coleman, and J.L. Koenig. The Theory of Vibrational Spectroscopy and Its Application to Polymeric Materials. John Wiley and Sons, New York, 1982.

[64] L.S. Plano and F. Adar. Proceedings of SPIE, volume 822. SPIE, 1987.

[65] H-C Tsai and D.B. Bogy. Characterization of diamondlike carbon films and their application as overcoats on thin-film media for magnetic recording. Journal of Vacuum Science and Technology A, 5(6):3287, 1987.

[66] J.J. Freeman, D.O. Fisher, and G.J. Gervasio. FT-Raman on-Line Analysis of PCL_3 Reactor Material. Applied Spectroscopy, 47(8):1115–1122, 1993.

[67] J.D. Pasteris, B. Wopenka, J.J. Freeman, V.L. Young, and H.J. Brandon. Medical mineralogy as a new challenge to the geologist: Silicates in human mammary tissue? American Mineralogist, 84:997–1008, 1999.

[68] H.-U. Gramlich and B. Yan, editors. Infrared and Raman Spectroscopy of Biological Materials. Marcel Dekker, New York, 2001.

[69] T.A. Alexander, P.M. Pellegrino, and J.B. Gillespie. Near-Infrared Surface-Enhanced-Raman-Scattering-Mediated Detection of Single Optically Trapped Bacterial Spores. Applied Spectroscopy, 57(11):1340–1345, 2003.

[70] G.D. Sockalingum, H. Lamfarraj, A. Beljebbar, P. Pina, M. Delavenne, F. Witthuhn, P. Allouch, and M. Manfait. Vibrational spectroscopy as a probe to rapidly detect, identify, and characterize micro-organisms. In M.D. Morris, editor, Proceedings of SPIE, volume 3608, pages 185–194, 1999.

[71] M. Manfait, P. Lamaze, H. Lamfarraj, M. Pluot, and G.D. Sockalingum. Diagnosis and prognosis of tissue pathologies by Raman microspectroscopy: An application to human thyroid tumors. In A. Mahadevan-Jansen and G.J. Puppels, editors, Proceedings of SPIE, volume 3918, pages 153–160, 2000.

[72] Christopher J. Frank, Richard L. McCreery, and Douglas C. B. Redd. Raman Spectroscopy of Normal and Diseased Human Breast Tissues. Analytical Chemistry, 67(5):777–783, 1995.

[73] Renata Andrade Bitar, Herculano da Silva Martinho, Carlos Julio Tierra-Criollo, Leandra Naira Zambelli Ramalho, Mario Mourao Netto, and Airton Abrahao Martin. Biochemical analysis of human breast tissues using Fourier-transform Raman spectroscopy. Journal of Biomedical Optics, 11(5):054001–1 – 054001–8, 2006.

[74] T. G. Spiro and X.-Y. Li. Biological applications of Raman spectroscopy., volume 3. Wiley, New York, 1988.

[75] S. Hu, K.M. Smith, and T.G. Spiro. Assignment of Protoheme Resonance

Raman Spectrum by Heme Labeling in Myoglobin. Journal of the American Chemical Society, 118(50):12638–12646, 1996.

[76] D.M. Kurtz, Jr., D.F Shriver, and I.M. Klotz. Resonance raman spectroscopy with unsymmetrically isotopic ligands. Differentiation of possible structures of hemerythrin complexes. Journal of the American Chemical Society, 98(16):5033–5035, 1976.

[77] A.K. Shiemke, T.M. Loehr, and J. Sanders-Loehr. Resonance Raman Study of Oxyhemerythrin and Hydroxomethemerythrin. Evidence fo Hydrogen Bonding Ligans to the Fe-O-Fe Center. Journal of the American Chemical Society, 108(9):2437–2443, 1986.

[78] W.H. Woodruff, R.B. Dyer, and J.R. Schoonover. Resonance Raman spectroscopy of blue copper proteins. In T.G. Spiro, editor, Biological Applications of Raman spectroscopy. John Wiley and Sons, New York, 1988.

[79] Teresa B. Freedman, Joann S. Loehr, and Thomas M. Loehr. A resonance Raman study of the copper protein, hemocyanin. New evidence for the structure of the oxygen-binding site. Journal of the American Chemical Society, 98(10):2809–2815, 1976.

[80] D. Gill, R. G. Kilponen, and L. Rimai. Resonance Raman Scattering of Laser Radiation by Vibrational Modes of Carotenoid Pigment Molecules in Intact Plant Tissues. Nature, 227(5259):743–744, 1970.

[81] K. Larsson and L. Hellgren. A study of the combined Raman and fluorescence scattering from human blood plasma. Experientia, 30(5):481–483, 1974.

[82] Integrated DNA Technologies. Frequently Asked Questions. "www.idtdna.com/InstantKB/", 2006.

[83] R. Owczarzy and M. Behlke. Calculation of Tm for Oligonucleotide Duplexes. Technical report, Integrated DNA Technologies, 2005.

[84] Information Sheet for Product # D4522. Technical report, Sigma Aldrich, Saint Louis, Missouri, 2005.

[85] A Jirasek, Q Matthews, M Hilts, G Schulze, M W Blades, and R F B Turner. Investigation of a 2D two-point maximum entropy regularization method for signal-to-noise ratio enhancement: application to CT polymer gel dosimetry. Physics in Medicine and Biology, 51(10):2599–2617, 2006.

[86] L. S. Greek, H. G. Schulze, M. W. Blades, A. V. Bree, B. B. Gorzalka, and R. F. B. Turner. SNR enhancement and deconvolution of Raman-spectra using a 2-point entropy regularization method. Applied Spectroscopy, 49(4):425–431, 1995.

[87] C. Schildkraut and S. Lifson. Dependence of the melting temperature of DNA on salt concentration. Biopolymers, 3(2):195–208, 1965.

[88] R. Owczarzy, Y. You, B.G. Moreira, J.A. Manthey, L. Huang, M.A. Behlke, and J.A. Walder. Effects of Sodium Ions on DNA Duplex Oligomers: Improved Predictions of Melting Temperatures. Biochemistry, 43(12):3537–3554, 2004.

[89] L. Movileanu, J. M. Benevides, and G. J. Thomas. Determination of base and backbone contributions to the thermodynamics of premelting and melting transitions in B DNA. Nucleic Acids Research, 30(17):3767–3777, 2002.

[90] J. R. Perno, C. A. Grygon, and T. G. Spiro. Ultraviolet Raman Excitation Profiles for the Nucleotides and for the Nucleic-Acid Duplexes Poly(rA)-Poly(rU) and Poly(dG-dC). Journal of Physical Chemistry, 93(15):5672–5678, 1989.

[91] L. Movileanu, J. M. Benevides, and G. J. Thomas. Temperature dependence of the Raman spectrum of DNA. II. Raman signatures of premelting and melting transitions of poly(dA)-poly(dT) and comparison with poly(dA-dT)-poly(dA-dT). Biopolymers, 63(3):181–194, 2002.

[92] Yoshifumi Nishimura, Masamichi Tsuboi, Tomohiro Sato, and Katsuyuki Aoki. Conformation-sensitive Raman lines of mononucleotides and their use in a structure analysis of polynucleotides: guanine and cytosine nucleotides. Journal of Molecular Structure, 146:123–153, 1986.

[93] J. Ruiz-Chica, M. A. Medina, F. Sanchez-Jimenez, and F. J. Ramirez. Fourier Transform Raman Study of the Structural Specificities on the Interaction between DNA and Biogenic Polyamines. Biophysical Journal, 80(1):443–454, 2001.

[94] J. F. Neault and H. A. Tajmir-Riahi. Structural Analysis of DNA-Chlorophyll Complexes by Fourier Transform Infrared Difference Spectroscopy. Biophysical Journal, 76(4):2177–2182, 1999.

[95] Jean-François Neault and Heidar-Ali Tajmir-Riahi. Diethylstilbestrol-DNA Interaction Studied by Fourier Transform Infrared and Raman Spectroscopy. Journal of Biological Chemistry, 271(14):8140–8143, 1996.

[96] Carlos E. Crespo-Hernandez, Boiko Cohen, and Bern Kohler. Base stacking controls excited-state dynamics in A·T DNA. Nature, 436(7054):1141–1144, 2005.

[97] S. C. Erfurth and W. L. Peticolas. Melting and premelting phenomenon in DNA by laser Raman scattering. Biopolymers, 14(2):247–264, 1975.

[98] James M. Benevides, Patricia L. Stow, Leodevico L. Ilag, Nino L. Incardona, and George J. Thomas. Differences in secondary structure between pack-

aged and unpackaged single-stranded DNA of bacteriophage ϕX174 determined by Raman spectroscopy: a model for ϕX174 DNA packaging. Biochemistry, 30(20):4855–4863, 1991.

[99] J Duguid, V A Bloomfield, J Benevides, and Jr Thomas, G J. Raman spectroscopy of DNA-metal complexes. I. Interactions and conformational effects of the divalent cations: Mg, Ca, Sr, Ba, Mn, Co, Ni, Cu, Pd, and Cd. Biophysical Journal, 65(5):1916–1928, 1993.

[100] S. C. Erfurth, E. J. Kiser, and W. L. Peticolas. Determination of the backbone structure of nucleic acid oligomers by laser Raman scattering. Proceedings of the National Academy of Sciences of the United States of America, 69:938–941, 1972.

[101] L. Movileanu, J. M. Benevides, and G. J. Thomas. Temperature dependence of the Raman spectrum of DNA. Part I - Raman signatures of premelting and melting transitions of poly(dA-dT)·poly(dA-dT). Journal of Raman Spectroscopy, 30(8):637–649, 1999.

[102] O. D. Schärer. Chemistry and Biology of DNA Repair. Angewandte Chemie International Edition, 42(26):2946–2974, 2003.

[103] G. J. Puppels, J. H. F. Olminkhof, G. M. J. Segers-Nolten, C. Otto, F. F. M. de Mul, and J. Greve. Laser irradiation and Raman spectroscopy of single living cells and chromosomes: Sample degradation occurs with 514.5 nm but not with 660 nm laser light. Experimental Cell Research, 195(2):361–367, 1991.

[104] Haiyang Tang, Huilu Yao, Guiwen Wang, Yun Wang, Yong qing Li, and Meifu Feng. NIR Raman spectroscopic investigation of single mitochondria trapped by optical tweezers. Optics Express, 15(20):12708–12716, 2007.

[105] I. Notingher, S. Verrier, S. Haque, J.M. Polak, and L.L. Hench. Spectroscopic study of human lung epithelial cells (A549) in culture: Living cells versus dead cells. Biopolymers, 72(4):230–240, 2003.

[106] S. Verrier, I. Notingher, J.M. Polak, and L.L. Hench. In situ monitoring of cell death using Raman microspectroscopy. Biopolymers, 74(1-2):157–162, 2004.

[107] N. Uzunbajakava, A. Lenferink, Y. Kraan, E. Volokhina, G. Vrensen, J. Greve, and C. Otto. Nonresonant Confocal Raman Imaging of DNA and Protein Distribution in Apoptotic Cells. Biophysical Journal, 84(6):3968–3981, 2003.

[108] Michael A. Short, Harvey Lui, David McLean, Haishan Zeng, Abdulmajeed Alajlan, and X. K. Chen. Changes in nuclei and peritumoral collagen within nodular basal cell carcinomas via confocal micro-Raman spectroscopy. Journal of Biomedical Optics, 11(3):034004, 2006.

[109] Christian Matthäus, Susie Boydston-White, Miloš Miljković, Melissa Romeo, and Max Diem. Raman and Infrared Microspectral Imaging of Mitotic Cells. Applied Spectroscopy, 60(1):1–8, 2006.

University of Victoria

Partial Copyright License

Title of Dissertation: The use of UV Resonance Raman Spectroscopy in the analysis of ionizing radiation-induced damage in DNA .

Author: _____

Conor Shaw

December 13th, 2007